SF 298 MASTER COPY KEEP THIS COPY FOR REPRODUCTION PURPOSES

REPORT DOCUMENTATION PAGE

Form Approved
OMB NO. 0704-0188

1. AGENCY USE ONLY *(Leave blank)*	2. REPORT DATE	3. REPORT TYPE AND DATES COVERED
	30 Mar 98	Final

4. TITLE AND SUBTITLE

CHARACTERIZATION OF HYBRID MATERIAL INTERPHASES

5. FUNDING NUMBERS

DAAH04-95-1-0496

6. AUTHOR(S)

Lawrence T. Drzal, Henjen Ho, Matthias Alt

7. PERFORMING ORGANIZATION NAMES(S) AND ADDRESS(ES)

Composite Materials and Structures Center
College of Engineering
Michigan State University
2100 Engineering Building
East Lansing, MI 48824-1226

8. PERFORMING ORGANIZATION REPORT NUMBER

9. SPONSORING / MONITORING AGENCY NAME(S) AND ADDRESS(ES)

U.S. Army Research Office
P.O. Box 12211
Research Triangle Park, NC 27709-2211

10. SPONSORING / MONITORING AGENCY REPORT NUMBER

ARO 34890.1-MS

11. SUPPLEMENTARY NOTES

The views, opinions and/or findings contained in this report are those of the author(s) and should not be construed as an official Department of the Army position, policy or decision, unless so designated by other documentation.

12a. DISTRIBUTION / AVAILABILITY STATEMENT

Approved for public release; distribution unlimited.

12 b. DISTRIBUTION CODE

13. ABSTRACT *(Maximum 200 words)*

A comprehensive non-linear finite element analysis study has been performed of the single fiber fragmentation test and the microindentation test to evaluate the mechanics of these techniques for measuring fiber-matrix adhesion in fiber reinforced polymeric composite materials. The determination of the fiber-matrix interphase modulus and its spatial variation has been shown to be important to relating microtesting methods to composites properties. As a result, a novel micro testing technique has been proposed for adherend-adhesive or fiber-matrix interphase properties characterization. A modified shear lag relationship was combined with the fiber strain energy equation to obtain an equation for mean/average interfacial shear stress and pseudo mean interfacial shear modulus. Good agreement was found. An experimental study using dynamic mechanical analysis was performed using these methods. The influence of test parameters has been evaluated and have been found to give a clear, reproducible reading of the loss and storage modulus as well as the exact glass transition temperature. The sensitivity of the DMA has proven to be exceptionally high. The viscoelastic response of an interphase with a thickness of only 3% by volume of the fiber can be detected and the interphase influence on the storage modulus of the composite can be quantified.

14. SUBJECT TERMS

Adhesion, Interphase, Composite Materials, Testing

15. NUMBER IF PAGES

147

16. PRICE CODE

17. SECURITY CLASSIFICATION OR REPORT	18. SECURITY CLASSIFICATION OF THIS PAGE	19. SECURITY CLASSIFICATION OF ABSTRACT	20. LIMITATION OF ABSTRACT
UNCLASSIFIED	UNCLASSIFIED	UNCLASSIFIED	UL

CHARACTERIZATION OF HYBRID MATERIAL INTERPHASES

Final Progress Report
by

Lawrence T. Drzal, Ph.D.
Henjen Ho, Ph.D.
Matthias Alt

March 30, 1998

for

US ARMY RESEARCH OFFICE

ATTN: DR. EDWARD S. CHEN
P. O. BOX 12211
RESEARCH TRIANGLE PARK, NC 27709-2211
CONTRACT/GRANT NO. DAAH04-95-1-0496

Michigan State University
Composite Materials and Structures Center
East Lansing, MI 48824-1226

Approved for Public Release
Distribution Unlimited

The views, opinions and/or findings contained in this report are those of the authors and should not be construed as an official Department of the Army position, policy or decision, unless so designated by other documentation.

LIST OF TABLES

LIST OF FIGURES

ACKNOWLEDGMENT

This work was supported by the U.S. Army Research Office under grant No. DAAH04-95-1-0496. Dr. Edward S. Chen was the project monitor. The discussions and suggestions of Dr. Stanley Wentworth and Dr. Walter Zukas are gratefully acknowledged.

SUMMARY

A comprehensive non-linear finite element analysis study has been performed of the single fiber fragmentation test and the microindentation test to evaluate the mechanics of these techniques for measuring fiber-matrix adhesion in fiber reinforced polymeric composite materials. The determination of the fiber-matrix interphase modulus and its spatial variation has been shown to be important to relating microtesting methods to composites properties. As a result, a novel micro testing technique has been proposed for adherend-adhesive or fiber-matrix interphase properties characterization. A modified shear lag relationship was combined with the fiber strain energy equation to obtain an equation for mean/average interfacial shear stress and pseudo mean interfacial shear modulus. Good agreement was found. An experimental study using dynamic mechanical analysis was performed using these methods. The influence of test parameters has been evaluated and have been found to give a clear, reproducible reading of the loss and storage modulus as well as the exact glass transition temperature. The sensitivity of the DMA has proven to be exceptionally high. The viscoelastic response of an interphase with a thickness of only 3% by volume of the fiber can be detected and the interphase influence on the storage modulus of the composite can be quantified.

1. INTRODUCTION

1.1 Interphase

Though there is still lack of a complete understanding of the mechanisms of adhesion between adherend-adhesive joint and fiber-matrix composites, it is now well accepted that an interphase region different in structure and composition exists near the adherend-adhesive and fiber-matrix interface. This interphase includes the two dimensional region of contact between adherend and adhesive (the interface) but also incorporates a region of some finite thickness extending on both sides of the interface. The boundaries of the interphase are defined as extending from the point in the adhesive where the local properties start to change from the bulk properties in the direction of the interface [1]. This region includes adhesive that may have chemical and morphological features different from the bulk adhesive. It can include impurities, unreacted polymer

components, non-polymerized adhesive additives, etc. At the interface, not only can there be chemical and physical interactions between fiber and adhesive, but also voids, adsorbed gases and surface chemical groups. On the adherend or reinforcement side, morphological and chemical features can be different from the bulk. Imposed upon the interphase are the processing conditions which allow chemical reactions, volumetric changes and the operational environment consisting of the mechanical stresses in a combined thermal and chemical environment. The resultant "interphase' can be a very complex material which is not easily described by single parameter models.

The interphase plays a role in the mechanical performance of the composite structure. First, the interface (a two dimensional area inside the interphase) is responsible for the level of adhesion which insures the structural integrity and behavior. Second, the interphase also functions as a mechanical entity which is subject to the applied mechanical and thermal loads and can be a failure site. Either interface or interphase failure can occur which in turn introduces a structural joint failure or fiber-matrix debonding. Therefore, high levels of adhesion as a result of a high degree of chemical bonding is not the only consideration for structural integrity. In most cases, an optimum in the interphasal properties should be the ultimate goal. For optimal adhesion at the interface and optimal interphasal properties, the choice of surface treatment, primer, finish or sizing will depend to a large extent on the adherend or reinforcing fiber as well as the adhesive or polymeric matrix. Therefore the concept of chemical bonding cannot be used exclusively in selecting a surface treatment, which is applied to remove the native defective surface and leave behind one that is rich in surface functionality to promote thermodynamic wetting. Close attention must be paid to the interphasal failure mode (tension, shear, mixed mode) and failure site (interface, interphase) at the point of fiber fracture as well as the operational environment of the adherend-adhesive joint and fiber-matrix composites. In general, a balance between interfacial adhesion and interphasal properties is desirable.

1.2 Interphase Mechanical Properties

Early research on the interfacial shear stress transfer at fiber breaks are exclusively based on a two-phase model (fiber-matrix). Fiber and matrix properties as well as the

geometric terms related to fiber geometry and position are the parameters dominating the interfacial stress distribution, and the interphase was not considered as a component of the composite. Therefore, an expression for the local shear stress distribution taking into account interphase properties and geometry have to be developed. The mechanical properties may affect the local shear stress distribution and limit the degree of adhesion between the fiber and matrix.

Recently, single fiber methods were used to measure fiber-matrix adhesion in which the same matrix chemistry was used with polymers having different distance between crosslinks and therefore different mechanical properties. The interfacial interactions that resulted in the formation of the interphase were constant but the resulting mechanical properties of this region changed as the matrix composition changed in a predictable manner. The fiber-matrix interfacial shear strength was dependent on this changing interphase and matrix properties [2]. This combined effects of interphase composition and matrix properties on adhesion as observed from experiments can be further uncoupled through analytical methods, such as finite element analysis, and controlled interphase (application of distinct coating material to fibers). It is also one of the many goals in this research.

1.3 Interface Adhesion: SurfaceChemistry, Surface Energy, Surface Morphology

Fiber or adherend surface chemistry also plays an important role in determining interfacial adhesion and interphasal properties. The interphase that is formed when the polymeric adhesive or matrix come in contact with the adherend or fiber must be thermodynamically stable, i.e. its interfacial free energy must be negative. This can be illustrated by a recently completed study on a series of IM6 carbon fibers. **Figure 1.3.1** shows the systematic change in the oxygen and nitrogen content of these carbon fibers surfaces after chemical treatment. **Figure 1.3.2** shows the change in the surface free energy of the same fibers with surface treatment. In all cases the concentration of the surface groups increase and the surface free energy increases in a similar manner.

In combination with any polymeric matrix or adhesive the interfacial free energy would decrease with increasing surface treatment insuring that the formed interphase is stable. A direct relationship exists between the number and type of surface functional

groups and adhesion as measured in composite materials. When the interfacial shear strength is measured for this series of IM6 fibers in the same epoxy matrix, a systematic increase is measured as both the surface free energy and number of surface functional groups, in this case oxygen, increase. **Figure 1.3.3** is a plot of all these variables against the interfacial shear strength. It can be seen that there is a very strong relationship between surface chemistry and adhesion.

Previously completed and reported studies have neglected to consider topographical features and surface morphology as being contributing factors to fiber-matrix adhesion. Surface area measurements of reinforcing fibers tend to be at the lower end of the sensitivity of most gas absorption apparatus used for surface area quantification. High resolution scanning electron microscopy has a limited depth of field. In adhesive bonding of structural adhesive joints, topographic features and morphology has been shown to play an important role.

Recently, the scanning tunneling microscope has allowed the surface topography of carbon fiber surfaces to be quantified with a high degree of resolution. **Figure 1.3.4** is a scanning tunneling micrographic image of an IM6 fiber cited in previous studies. A series of micrographs of various scan sizes were collected for the IM6 series of carbon fibers in order to quantify the surface roughness and surface area. When the surface chemical groups that are added during surface treatment are compared to the simultaneous changes that take place in the surface area or roughness with surface treatment as shown in **Figure 1.3.5** and both are compared against the changes in the interfacial shear strength between fiber and matrix, it is obvious that the surface chemical groups which are added with increasing surface treatment levels increase at the same rate as the fiber surface area. It has been shown that when these groups are removed or made non-reactive to the epoxy matrix, significant increases in adhesion are still detected because of the increase in surface roughness and surface area. This result draws an interesting and provocative parallel to the results of studies on adhesion of structural adhesives to anodized aluminum adherends. For structural adhesive bonding both surface chemical and surface morphological factors have been shown to be important to adhesive joint strength.

1.4 Interphase Effect on Adhesion

Recent studies [3,4] by the authors have shown that fiber-matrix adhesion affects both fiber off-axis and unidirectional composite properties. However, the degree of influence of the interfacial shear strength on the composite global properties were not the same.

1.4.1 Composite Interlaminar Shear Strength (Short Beam Shear)

A summary of the experimental data obtained from the composite interlaminar shear strength test on unidirectional composites is plotted in **Figure 1.4.1**. The value of the interlaminar shear strength and fiber-matrix interfacial shear strength of the IM6-0% fiber were taken as the baseline and all other data for the other IM6 fibers was "normalized" by dividing their values by the IM6-0% values. The largest difference occurs between the untreated IM6-0% fiber and the IM6-20% surface treated fiber. The ILSS increases 91%. However, the shear strength remains relatively unchanged after this treatment even when the fiber surface treatment level is increased to 600%. The plateau in the shear strength at 20% fiber surface treatment level is not unexpected if it is assumed that the interfacial shear strength of 20% surface treated fibers is close to the interphasal or matrix shear strength. In the short beam shear test, since the interlaminar shear stresses dominate, the failure is governed by either the interfacial shear strength or the matrix shear strength.

1.4.2 Transverse Flexural Strength

A plot of the "normalized" values for the transverse flexural strength are shown in **Figure 1.4.2**. The transverse flexural strength is strongly dependent on changes in the interfacial shear strength and increase by almost 205% when the fibers are surface treated to only 20%. The 20% surface treatment produces an increase in the fiber-matrix interfacial shear strength by about 83%. Although, there is an additional increase in the interfacial shear strength, the transverse flexural properties of the composites do not increase in a corresponding manner. The low value measured for the IM6-600% composite is an artifact due to the lower fiber volume fraction in this sample. The plateau in the transverse flexural properties starting at 20% surface treatment suggests that the transverse tensile strength of the fiber-matrix interface for the IM6-20% surface treated

fibers may have reached a limit in a manner similar to the interlaminar shear strength.

1.4.3 Mode II Fracture Toughness

The End-Notched Flexure (ENF) test provides a method for measuring the composite interlaminar fracture toughness (G_{IIC}) in forward shear mode. The normalized average values of G_{IIC} of the composites as a function of fiber surface treatment level are shown in **Figure 1.4.3**. Clearly the fiber surface treatment level has a strong influence on G_{IIC}. A significant increase in the G_{IIC} occurs for the composites having the 20% surface treatment. G_{IIC} continues to increase for all other surface treatments albeit more slowly. Unlike the other composite properties of interlaminar shear strength and transverse flexural strength where no significant increase in strengths was noticed beyond 20% surface treatment level, composite G_{IIC} continues to increase with the interfacial shear strength for all surface treatment levels.

The interlaminar fracture toughness of a composite is a measure of the energy barrier that an existing interlaminar crack has to overcome in order for it to propagate. In most unidirectional composites, interlaminar crack propagation occurs either along the fiber-matrix interface, through the matrix material or alternating between the neighboring fiber-matrix interfaces. Clearly, therefore, the G_{IIC} should increase with the interfacial shear strength as long as the interfacial shear strength is less than the matrix shear strength. Because of the high fiber volume fraction in these composites and the significant intermingling of fibers (resulting from the high consolidation pressure during processing), the interlaminar crack cannot remain in one plane in this Mode II test. Therefore, unstable crack growth can occur from the existing end-notch when the energy barriers imposed both by the fiber-matrix interface and the matrix material can be overcome by the growing crack. Since there is a large amount of fiber-matrix interface surface in these high fiber volume fraction composites, the change in interface properties should have a significant effect on the G_{IIC}.

The above three global test results showed that Mode II fracture toughness value increases accordingly with the increase of the apparent interfacial shear strength obtained from single fiber fragmentation test while the short beam shear and transverse flexure test results do not show this one-to-one relationship. However, from mechanics point of

view, the short beam shear and transverse flexure strengths should be more directly related to the interfacial shear strength than the Mode II fracture toughness, which in essence is the strain energy release rate for crack propagation. Therefore, the contradiction is worthy of further investigation. In this research, the fundamental test mechanics of the single fiber fragmentation test will be studied in order to provide an answer to the above-mentioned paradox.

1.5 Fiber-Matrix and Adherend-Adhesive Interphases

This review of the influence of the interphase in fiber-matrix systems in composite materials illustrates the surface and interphase characteristics that are necessary in order to develop the same type of fundamental understanding of the adherend-adhesive interphase. The adherend surface chemistry and energetics are important for the initial response of the adhesive to the adherend surface and for determining if the resulting interphase is thermodynamically stable. The adherend surface morphology and topography are sites for specific chemical groups and enhance the wetting and spreading of the adhesive over the adherend. The adherend-adhesive dimensions, e.g. oxide thickness, and the interphase mechanical properties are necessary to determine the mechanical response of the interphase to applied stress and to develop models for adhesive joint behavior. Finally, post-failure inspection of the interphase is required to determine the locus of failure. Although the majority of published results on the role of the interphase have been conducted on composite systems, these results can be extended to adhesive joints where the same phenomena take place.

Even though it is not yet possible to either quantify or predict the formation of the "interphase" from first principles, it can serve as a framework on which the interactions between composite constituents can be studied and the interphase can be designed in an optimal manner. The ability to quantify this interphase region not only in terms of its molecular and morphological constituents, but also in terms of its mechanical properties is the single most important factor in being able to advance the use of structural adhesive bonding.

1.6 Interphase Properties Characterization

There are several micro test methods (single fiber fragmentation test, fiber pull out test, and micro indentation test [5-7]) for evaluating the interfacial adhesion or interphasal shear strength between the fiber and matrix. The interfacial shear strength is defined as the maximum shear stress at the interface or interphase which causes debonding between the fiber and matrix. Fiber-matrix debonding may be caused by interfacial shear failure (adhesive) or interphasal shear failure (cohesive). In either case, the apparent failure strength is defined as interfacial shear strength by most researchers, though it should be more appropriately defined as interphasal shear strength because the interface is a distinct bi-material surface area inside the interphase. In some studies, the interphase may be a material with known mechanical properties. In other occasions, however, the interphase modulus is not known *a priori* and is a desired quantity. Nano indentation technique, in which a nano indenter is used to measure the hardness of a finite ring region surrounding the fiber, is applied for interphase modulus measurement. However, the application of this technique to such a small geometry scale always introduces confusion between material nonhomogeneity and multiphase in composite materials. In addition, the surface hardness value cannot be readily translated into material modulus. Therefore, a technique for direct interphase modulus and strength measurement needs to be developed. In this research, a novel method for interphase modulus measurement is proposed.

1.7 Previous Work [8]

In the structural adhesive field, due to its simplicity, the single-lap joint has been adopted as a standard mechanical test method for determining the shear strength (ASTM D1002-94) and modulus (ASTM D3983-93) properties of structure adhesives. However, the shear stress concentration and peel stress at the edge of the adhesive layer induced by the adherend bending have been the cause for inconsistent and inaccurate measurement of adhesive properties. To eliminate the problems caused by adherend bending, Goland and Reissner [9] studied the stress distributions for adhesive lap joints between circular tubes and suggested that nearly uniform stresses along the joint were obtainable. However, cost constraint and technical difficulty have prohibited the application of the tubular lap shear experiment. In addition, improper load application at the tube ends usually induces more

undesired complexity. The much simpler micro tests commonly used in the composite community applies similar mechanics principles for fiber-matrix interface property characterization and can be a alternative for the circular tube lap joint test. The fiber-interphase-matrix assembly in a composite material in fact is analogous to the adherend-adhesive-adherend combination in the structural adhesive lap joint. In the previous report, two micro testing methods, the single fiber fragmentation and single fiber micro indentation tests, were used to characterize the interphasal properties of aluminum wire/Epon 828 matrix composite. The two micro tests were used originally in favor of the traditional lap shear testing to avoid undesirable transverse normal (peel) and interlaminar shear stresses at the joint edges. The commonly used micro tests in composite industries were for the first time applied to measure the metal adherend/adhesive interphase properties.

However, these micro testing methods provide results which often do not agree quantitatively and qualitatively, and are sometime contradictory. Thus a basic research on the mechanics of each micro test is necessary for proper interpretation of the experimental data. In this research, finite element method is applied to evaluate the test mechanics and stress transfer mechanism in the two micro tests. The validity of the micro tests for adhesion characterization will be studied and the principal difference in the two micro tests identified.

1.7.1 Single Fiber Fragmentation Test

In the previous study, the commonly observed fiber fractures and interfacial debonding in carbon or glass fiber/polymer matrix composites did not occur in the aluminum wire/Epon 828 specimens. The Kelly & Tyson equation for extracting average interfacial shear strength from fiber critical length cannot be applied to obtain the interfacial shear strength of the aluminum wire/Epon 828 specimens. For as received and anodized aluminum wire/Epon 828 specimens, oxide layer fractures are observed. As the oxide layer becomes thicker, the number of oxide layer fractures decreases. Because the tensile failure strength or strain of the oxide layer is less than the tensile strength or strain of the aluminum wire, the desired fiber fractures and shear stress transfer did not occur.

A detailed mechanics study of this single fiber fragmentation test is therefore needed for the understanding of the test method.

1.7.2 Single Fiber Micro Indentation Test

In addition to the single fiber fragmentation test, single fiber micro indentation test was applied to measure the interfacial shear strength of aluminum wire/Epon 828 specimen. Due to the large diameter of the aluminum wire, large applied load is needed to induce failure shear stress or strain at the aluminum wire/Epon 828 matrix interface to cause debonding. Due to the load cell limitation of the test apparatus, debonding was not obtainable. An alternative push-in test was performed [8]. Similarly, debonding was not found from the indenter end, though ESEM pictures of the fiber end on the other side of the specimen did show evidence of interfacial debonding. Thus a new data reduction scheme needs to be developed for interphasal modulus characterization in situations when debonding is not feasible and the interfacial shear strength not obtainable. In this research, a data reduction method is proposed for interfacial shear stress estimation and a pseudo shear interphasal modulus calculation.

1.7.3 Cyclic Micro Indentation Test

Cyclic micro indentation tests were performed to differentiate the interphasal properties between as received and anodized aluminum wire composite and to evaluate the viscoelastic behavior of the interphase from the hysteresis load-displacement loops. It was found that for as received (d_f = 125 μm) and anodized (d_f = 100 μm) aluminum wire composite, there is an obvious difference in the hysteresis loops. However, the effect of fiber size on the load-displacement data was not investigated. Aluminum wire anodization on one hand reduces the fiber diameter and the corresponding surface area but on the other hand introduces change in fiber surface morphology and increases the surface roughness and surface area. The adhesion between the aluminum wire and Epon 828 matrix will increase as a result of fiber surface roughness. However, the fiber size factor has to be eliminated in order to render direct comparison between as received and anodized aluminum wire/Epon 828 specimen. Therefore, a data reduction scheme is needed to convert the load-displacement data to physically more meaningful stress-displacement or stress-pseudo strain to account for the non-uniformity of fiber diameters.

In this research, the cyclic micro indentation test of aluminum wires will be further studied using the developed data reduction scheme.

2. STATEMENT OF THE PROBLEM STUDIED & OBJECTIVES

The objectives of this work are:

- to study the test mechanics of single fiber fragmentation test and in-situ micro indentation tests in order to better interpret the test results and evaluate the applicability of each test methods in measuring composite properties as well as the adherend-adhesive interfacial properties in the metal (aluminum)-polymer assembly;
- to further study the current micro indentation system and develop a theory for data reduction of single fiber micro indentation test and for interphase modulus estimation;
- to evaluate the feasibility of using DMA for interphase modulus characterization.

3. APPROACH

In this study, analytical, numerical (finite element) and experimental analyses are used to facilitate a comprehensive understanding of interfacial shear strength and interphase properties characterization. First, the mechanics of single fiber fragmentation and micro indentation tests will be studied in order to provide a logical explanation to the discrepancies in the test results. Finite element models of the single fiber fragmentation and micro indentation tests are established and a comprehensive parametric study conducted to study the effects of processing variables on the stress distribution at the interface and interfacial shear strength. The test mechanics of the single fiber fragmentation and micro indentation tests are compared. A modified single fiber micro indentation test is proposed and the data reduction scheme developed using the modified Kelly & Tyson equation and a simplified energy approach. A cyclic single aluminum wire/Epon 828 indentation test is performed and the newly developed data reduction scheme is used to reduce the test data for evaluating the effects of matrix modulus, fiber size and fiber anodization on interphase modulus. Finally, the Dynamic Mechanical Analysis is used to evaluate the interphase effect on the thermal mechanical properties change of the single aluminum fiber/polymer matrix composite.

3.1 Mechanics of Single Fiber Fragmentation Test

The single-fiber fragmentation test originally proposed by Kelly and Tyson [5] assumes that the fiber and matrix is perfectly bonded and the matrix is perfectly plastic such that an average interfacial shear strength, τ, can be determined from a simple balance of force which results in

$$\tau=\frac{\sigma_f d_f}{2l_c} \tag{1}$$

where d_f is the fiber diameter, σ_f is the fiber tensile strength corresponding to the fiber critical length, l_C. However, recent studies showed that for most carbon fiber reinforced polymeric composites interfacial debonding at the fiber ends always accompanies fiber fracture [1,2]. As a result, the effectiveness of the single-fiber fragmentation test for interfacial shear strength measurement was in doubt. A recent experimental study by Drzal et. al. [3,4] showed that the mode II fracture toughness has a one-to-one relationship with the apparent interfacial shear strength from the single-fiber fragmentation test, while the other global properties, such as the interlaminar shear and transverse flexure strengths, can be unrelated to the apparent interfacial shear strength from the fragmentation test. Therefore, a thorough mechanics study of this test technique is needed in order to understand the effectiveness of the fragmentation test for interfacial shear strength measurement and correct interpretation of the test results. To this end, finite element analysis will be applied to evaluate effect of debonding and material plasticity on the *fiber critical length* of fragmentation test.

3.1.1 Finite Element Studies: Literature Review

Among the micro-level experiments, the single fiber fragmentation test is the most frequently used test method because of its simplicity, easiness, and sensitivity to changes in fiber/matrix adhesion due to the effect of surface treatment or finish [10]. However, the interfacial shear strength is calculated based on the force equilibrium of a simplified model of a perfectly bonded fiber and matrix element with an unrealistic assumption that the matrix shear stress is uniform. For better understanding of the interfacial shear strength and the effect of constituent materials on interphase stress-transfer characteristics, a more rigorous mechanical analysis is need. Over the years, a number of

analytical [11-13] and numerical [14-20] analyses have been employed to evaluate the stress transfer mechanism for the single-fiber composite. The analytical models usually are of simple geometry and boundary conditions, which in most cases contradict the experimental observation. In addition, the analytical analysis is limited to linear elastic material properties. On the contrary, the finite element method employs the same exact mathematical procedure in problem solving and yet possesses the flexibility for complex geometry modeling and boundary conditions. The earliest finite element analysis for the evaluation of the stress transfer between fiber and matrix date back to [14]. Carrara and McGarry evaluated the effect of fiber end geometry on the stress distributions along the fiber/matrix interface in a discontinuous single fiber composite. Most of the finite element analyses published afterwards are a continuation of Carrara and McGarry's work using a similar model [16, 18-21]. The analyses have been extended to a three-phase model [16, 18-20, 22] using transverse isotropic fiber properties [19, 20] and nonlinear matrix properties [21]. Effects of interphase thickness [18-20], interphase properties [16, 18, 22] and fiber properties [17, 18] on the stress distribution at the interface have also been investigated. However, these models are more appropriate for a discontinuous short fiber composite which is physically different from the continuous single fiber fragmentation test specimen. And most of the analyses were linear elastic analysis. The model of DiAnselmo et al. [22] is a better representative of the single-fiber fragmentation specimen; however, it only dealt with linear elastic constituent properties. Guild et al. [21] used a elasto-plastic matrix behavior in their analysis of discontinuous short fiber composite. It was a two-phase model and the main discussion was limited to the effect of fiber end shapes on the stress concentrations at regions near the fiber end and along the interface. Effects of the constituent properties (fiber, interphase, and matrix) on the stress transfer mechanism and other important characteristics such as interphasial debonding were not discussed. The study presented here is an extension of DiAnselmo et al. [22] and Guild et al [21]. The mechanics of the single-fiber fragmentation test is investigated using a three-phase, non-linear finite element analysis. The effect of the matrix strain state at the time of fragment fracture on the stress transfer efficiency is evaluated. Locations of stress singularity and the possibility of debond propagation are discussed.

Effects of interphase property gradients and thermal residual stresses on the local stress fields are studied. The physical meaning of the experimentally measured critical length is re-evaluated.

3.1.2 The Finite Element Model

Traditional finite element studies of the interface mechanics included the plane stress analysis with the plane parallel to the fiber axis [15], plane strain or generalized plane strain analysis with the plane perpendicular to the fiber axis [23], and the axisymmetric analysis [14, 16-22]. The plane strain analysis cannot be used to model the stress transfer at and near the fiber breaks and the plane stress analysis severely altered the fiber/matrix relative geometry in the composites. Thus, the two-dimensional axisymmetric analysis which utilizes a two-dimensional scheme with a three-dimensional nature is preferred. A schematic diagram of the single-fiber fragmentation specimen is shown in **Figure 3.1.1**, where the single-fiber coupon with a rectangular cross-section is modeled as a combination of three concentric cylinders representing the fiber, interphase, and matrix. One fragment section of the specimen coupon is isolated (as shown in **Figure 3.1.1**) and analyzed. The aspect ratio (fiber length/fiber diameter) for the fragment analyzed is 126.5, which is more than twice the critical length for graphite epoxy composites [2]. The outer matrix diameter of the model is 10.8 times the fiber diameter, large enough to ensure that the displacement and stress fields approach an undisturbed uniaxial stress state in the matrix. The fiber diameter (d_f), interphase thickness (t_i) are 8 μm and 0.16 μm (=0.02d_f), respectively. Along the symmetric and axisymmetric (fiber center line) axes, roller constraints are applied which restrain the normal displacement but allow for the shear deformation for the nodal points at these two boundaries. Immediately after the fiber breaks, the fiber will recoil and the matrix will stretch further due to the relaxation of the constraints imposed by the fiber. Thus a gap will be formed between the fragments and will extend with increasing applied strain. A gap length of 2 μm is used in this model. The outer cylindrical surface is a free boundary and a uniform displacement is applied at the upper edge as shown in **Figure 3.1.1**. Three layers of elements are used for the interphase. A total of 3927 nodes and 3409 axisymmetric four-node elements are used for the model. Elements are refined at regions

near the fiber breaks. For the debond case, interface elements are used to prevent inter-penetration of the fiber and the interphase. Sliding friction is assumed between the debonded surfaces.

3.1.3 Material Behavior

In practice, the nonlinear finite element analysis refers to the analysis which takes into account the boundary, geometry, and material nonlinearities [24]. However, in the study presented here, the progressive change of the boundary conditions, such as debonding, cannot be modeled. Thus the nonlinear analysis will be limited to geometric and material nonlinearity. Because the stress state is of uniaxial nature, the geometric nonlinearity only involves the nonlinear strain-displacement relations for regions with large deformation. In this analysis, the fiber is AS4 fiber which is assumed to be transversely isotropic and linearly elastic with the same properties as those used by Whitney and Drzal [11], **Table 3.1.1**. The matrix is assumed to be Epon 828 epoxy resin with metaphenylene diamine (mPDA) 14.5 parts by weight per hundred parts of the resin as curing agent. The interphase is assumed to be a layer of more brittle material having the properties of Epon 828 epoxy resin with 7.5 phr of mPDA [25]. The material response curves for Epon 828 with 14.5phr of mPDA (the matrix) and Epon 828 with 7.5 phr of mPDA (the interphase) are shown in **Figure 3.1.2** where it can be seen that the interphase is linear elastic while the matrix is nonlinear elasto-plastic. Thus the matrix is assumed to behave perfectly plastic after 6% strain in the finite element analysis. Note that the matrix nonlinear behavior cannot be represented using a single equation, as was the case in the nonlinear analysis of Ho et. al. [24], to prevent the negative stiffness situations at large strains. The nonlinear material behavior of the matrix is approximated by a combination of a series of piecewise linear sections. The initial moduli and Poisson's ratios of the interphase and matrix materials are shown in **Table 3.1.1**.

From experimental observation, the AS4 fiber began to fracture at 0.8% coupon strain and the fiber fractures were completed at 3.5% coupon strain [26], **Figure 3.1.3**. In this analysis, the effect of the matrix strain state upon the stress transfer between the matrix and the fiber is evaluated. Finite element models for fragments created at 1% and 2% matrix strains are analyzed. The stress transfer for fragments fractured at 1% and 2%

matrix strains are compared. The stress field, stress singularity, debonding and debond propagation as a result of fiber break are discussed for fragments created at 1% matrix strain. A relative displacement of 8 μm is applied at the upper edge of the model for all cases.

In certain circumstances, it is desired to tailor the interphase behavior to achieve desired composite performance [27]. Thus it is necessary to study the effect of the interphase or coating properties on the stress fields in the neighborhood of the fiber breaks. In this study, the effect of fiber modulus, interphase stiffness and thickness on the stress transfer efficiency was evaluated through a nonlinear finite element analysis. The effect of debonding on the stress redistribution; the effect of fiber surface roughness on the slide frictional stress transfer will be evaluated. The determination of the interfacial strength from the fiber strains using the technique of laser Raman spectroscopy will be discussed.

3.2 Mechanics of In-Situ Micro Indentation Test

Among many micro-mechanical test methods, the micro-indentation method has attracted much attention because it is an *in-situ* testing method conducted on a real composite thus allowing for evaluation of the processing or environmental exposure encountered either during manufacturing or in service. Moisture, solvent absorption, fatigue and thermal exposure can be properly evaluated for their effect on the fiber/matrix interface and composite properties. The micro-indentation method was first proposed by Mandell et al. [7] to measure the interfacial shear strength for fiber reinforced polymer composites. The microindentation test is run on the individually selected fibers on a polished cross-section of the composite using a specially constructed apparatus. In this study a specially constructed microindentation apparatus, called an Interfacial Testing System (ITS), developed by the Dow Chemical company [28] is used. A schematic diagram of the Interfacial Testing System is shown in **Figure 3.2.1**. A diamond-tipped stylus mounted on the objective lens holder of the microscope is used to push single fibers from their surrounding matrix. A specimen is prepared for testing by cutting a small piece (typically 1/4"" x 1/4" x 1/8") from the composite of interest, embedding it in metallographic specimen mount with the the fibers normal to the specimen surface, and

polishing the surface using conventional metallographic techniques. The specimen is placed on the microscope stage. The operator then selects the fibers to be tested from the TV monitor by moving the stage to the location of each fiber. By pressing a single key on the computer keyboard, the location of the fiber to be indented is stored in the computer memory. The stage then moves to put the fiber to be tested directly beneath the indenter. The stage then rises at a pre-selected rate until the indenter contacts the fiber. In some cases, the force-displacement data obtained during the indentation process can identify the fiber-matrix debond load and hence the adhesion or the interfacial shear strength. In other cases, the detection of the initiation of the debond relies on certain test procedures which include the use of an optical microscope for observation of debonding on the fiber surface. The interfacial shear strength is derived from the debond load using the results of a finite element analysis [7]. The data reduction scheme requires a choice as to a value of t_m/d_f where the finite element results will be assumed most accurate (t_m is the average matrix thickness between the tested fiber and its next nearest neighbors). Because the local fiber arrangement and spacing are not uniform, the experimental debond loads for various t_m/d_f are shifted to an adjusted value for a fixed t_m/d_f which is used in the finite element analysis [7,29]. The interfacial shear strength at debonding (τ_{deb}) is calculated based on a maximum shear stress criteria which ignoring the residual stresses can be given by:

$$\tau_{deb} = \sigma_{adj} * (\tau_{max}/\sigma_{app})_{fem} \qquad (2)$$

where σ_{adj} is the adjusted compressive stress applied to the fiber end at debonding and $(\tau_{max}/\sigma_{app})_{fem}$ is the ratio of the maximum interface shear stress to the applied stress resulting from a linear axisymmetric finite element analysis with t_m/d_f=0.4 [7,29].

In addition to the finite element methods, an analytical solution of the maximum interfacial shear stress, τ_i, at the interface for the micro-indentation test can be obtained by a shear-lag model for fiber pullout which gives [30]:

$$\tau_i = P*[4G_i/(t_i*d_f*E_f)]^{0.5} /(\pi*d_f) \qquad (3)$$

where t_i and P are the interphase thickness and applied load to the fiber, G_i and E_f are the interphase shear and fiber axial moduli, respectively. Matrix deformation was ignored in deriving the interfacial shear strains and stresses [30]. Mandell et. al. replaced the interphase properties with the matrix properties in equation 3 thereby ignoring the existence of an interphase and obtained the maximum interfacial shear stress as [7]:

$$\tau_i = 0.5\ \sigma avg * (G_m/E_f)^{1/2}\ (d_f/t_m)^{1/2} \qquad (4)$$

where G_m and σavg are the matrix shear modulus and average applied stress to the fiber, respectively. Recently, Tsai et al. [31] employed a modified shear lag theory to include the interphase in the model which took into account the matrix deformation and obtained the maximum interfacial shear stress at the interface as:

$$\tau_I = 0.707*\sigma_{fd}*(G_m/E_f)^{0.5}*\tanh(\alpha l)/\{(G_m/G_i-1)*\ln(1+2t_i/d_f)+\ln(1+2t_m/d_f)\}^{0.5} \qquad (5)$$

where G_i, t_i, and l are the interphase shear modulus, interphase thickness and fiber length, respectively. The parameter α is defined as

$$\alpha=\{2*G_i/[E_f*r_f^2\ln(r_i/r_f)]\}/\{1+[G_i*\ln(r_m/r_i)]/[G_m*\ln(r_i/r_f)]\} \qquad (6)$$

where r_f, r_i and r_m are fiber, interphase and matrix radii in a cylindrical representative volume element. In practice, a generalized empirical equation is embedded in the data reduction software of the ITS apparatus for interfacial shear strength calculation for samples of various fiber and matrix combinations [28]:

$$\tau_i/\sigma_{fd} = 0.8757\ (G_m/E_f)^{0.5} - 0.01863 * \ln(t_m/d_f) - 0.026496 \qquad (7)$$

While the micro-indentation technique proposed by Mandell *et. al.* is for the measurement of interfacial shear strength upon debond initiation, a cyclic micro-indentation test was developed by Marshall and co-workers to derive the interfacial shear stresses for sliding resistance [32] for weakly bonded and unbonded fiber reinforced ceramic matrix composites. From a simplified shear lag analysis, an equation was derived which relates the interfacial shear stress to the load-displacement data. However, the usefulness of the load-displacement data from the micro-indentation test for polymer composites has not been studied. One of the objectives of this study is to evaluate if the load-displacement data is sensitive to interphase parameters such that it can be used to obtain data on fiber-matrix adhesion and interphase properties.

Though the micro-indentation technique has been used in several aspects of material property characterization, the protocol for the micro-indentation test has not been established. Many of the test parameters are not standardized. For example, the aspect ratio (fiber length/diameter) of the sample and the type of the embedding material within the metallographic mount are not standardized and their effects on the experimental test data are not known. In addition, the common problem of large data scatter associated with the micro-indentation test is not well understood and is usually ignored. In this research, a broad and general parametric analysis was performed using a nonlinear finite element method to evaluate the effects of specimen preparation (such as fiber aspect ratio and sample embedding material) and material parameters (such as interphase and matrix properties, fiber diameter, interphase thickness and fiber volume fraction) on the interfacial shear stress distributions and the load-displacement data for micro-indentation tests on carbon fiber/polymer matrix composites. From results of this research, we will be able to identify the factors which have the most influence on the maximum interfacial shear stress and provide insight in interpreting the experimental results. The validity of the analytical closed form solutions of equations 4&5, and the empirical equation of the ITS apparatus [28], equation 7, will be evaluated by direct comparison with the nonlinear finite element results.

The purpose of the finite element analysis is to evaluate the interfacial stress fields corresponding to various processing and material variables and thus assess the effect of these variables on the interfacial shear strength measurement. Strictly speaking, shear failure in the interphase could be caused by interfacial shear failure between the fiber and the interphase or the shear failure of the interphase itself. Usually it is difficult to distinguish between these two failure modes, especially when the interphase is very thin. For a weak interface, interfacial shear failure occurs before interphase shear failure and the maximum interphase shear stress at the time of debonding is treated as the interfacial shear strength. The failure surface on the fiber is clean because failure is caused by separation of fiber and interphase at the bi-material boundary. For very strong fiber-interphase bonding, interphase shear failure occurs before interfacial shear failure and the shear strength of the interphase is treated as the interfacial shear strength. Failure may be

at the fiber-interphase interface or within the interphase. Thus the failed fiber surface may be attached with interphase material. Be it an interfacial failure or an interphase failure, the measured interfacial shear strength is directly related to the maximum interfacial shear stress obtainable subject to various processing and material variables. The purpose of this finite element analysis is to exclusively evaluate the effect of processing and material variables, such as fiber volume fraction, sample fabrication and preparation, fiber diameter, matrix and interphase properties, on the interfacial stress distributions.

3.2.1 Finite Element Model

The micro-indentation specimen assembly was modeled as a combination of four concentric cylindrical tubes representing the fiber, interphase, matrix and composite, **Figure 3.2.2**. The indenter was modeled as a rigid half sphere. For this cylindrical representative volume element, the finite element analysis requires only two-dimensional axisymmetric modeling. Due to symmetry, only half of the cross-sectional plane was analyzed. Fixed boundary conditions were assumed at the sides of the composite. Because the composite sample is placed in the metallographic specimen mount filled with embedding material, the composite sample in fact is sitting on an elastic or a nonlinearly elastic/plastic foundation, depending on the supporting material. A foundation of distinct material properties is modeled beneath the composite sample to account for effect of the embedding material within the metallographic specimen mount. Along the axisymmetric axis (the z-axis) and the bottom boundary (the r-axis), roller constraints are applied. The meshes in the interphase region are refined. Interface elements were used between the indenter and the fiber to prevent inter-penetration of the two bodies. Coulomb friction was assumed in the indenter-fiber contact zone. A compressive load of 5.0 grams (approximately 0.05 Newton) was applied to the top surface of the indenter. For the baseline model, the fiber aspect ratio is 61.25. The matrix thickness, t_m, corresponds to a 36% fiber volume fraction. The fiber diameter, d_f, and the interphase thickness, t_i, are 8 μm and 0.16 μm (=0.02d_f), respectively. In a preliminary study, it was found that the effect of the composite thickness on the indenter displacement and the interfacial shear stress is insignificant. The composite thickness is chosen to be 1.5 times the fiber

diameter to save computational time. The material properties for the baseline model is shown in **Table 3.1.1**. A total of 3420 nodes and 2903 axisymmetric four-node elements were used for the model.

3.2.2 Specimen Configuration

The effects of sampling techniques, such as fiber aspect ratio and the properties of specimen supporting material, on the interfacial stress distributions are evaluated. Three aspect ratios with l/d_f=36.25, 61.25, and 111.25 were used, which are considerably lower than the experimental values in order to reduce the computational time in the analyses. Linearly elastic steel and nonlinearly elastic/plastic epoxy (Epon-828) were used as foundation materials to examine the foundation effect. The properties of the supporting steel and epoxy materials are shown in **Table 3.1.1**.

3.2.3 Constituent Materials

Due to the characteristic material non-uniformity of the composites, the local fiber volume fraction in the neighborhood of the indented fibers is not the same. In addition, the selection of the fibers to be indented is rather arbitrary. The criteria for fiber selection require that for every fiber to be indented there should be at least two neighbor fibers at or within half fiber diameter away yet no closer than a quarter fiber diameter from the selected fiber [28]. Because of the material non-uniformity and the ambiguity of the fiber selection criteria, the fibers selected for indentation were subject to different local fiber volume fractions. For example, the distance between the indented fiber and nearest neighboring fiber is far from a constant value, as demonstrated in **Table 3.2.1**, which is a typical data set for the microindentation test. Thus models with different fiber volume fractions (V_f=10, 15, 20, 30 and 50%) were analyzed to evaluate the local fiber volume fraction effect on the interfacial shear stress distribution. Because there is a statistical distribution of fiber size in the sample, also shown in **Table 3.2.1**, the effect of the fiber diameter on the load-displacement curve and interfacial shear stress is investigated as well.

In practice, fiber-matrix adhesion and interphase properties can be changed by fiber surface treatment, application of sizing or coating materials, etc. To identify the effect of processing variables on the fiber-matrix adhesion, the variation of the stress fields as a result of interphase property change has to be investigated. Models with interphase/matrix modulus ratio E_i/E_m=0.7, 1, 1.5, 7.5, and 30 were analyzed to obtain the corresponding stress fields, where E_i and E_m are the initial interphase and matrix moduli, respectively. The effect of interphase thickness, t_i, on the load-displacement data and the interphase and matrix shear stress fields is evaluated using t_i=0.02d_f, 0.05125d_f, 0.125d_f, 0.2d_f, and 0.25d_f.

Interfacial stress fields corresponding to three matrices systems were also studied. While the fiber is the transversely isotropic carbon fiber, the matrices are the Epon 828 epoxy cured with mPDA and two other fictitious materials which are more compliant compared to the Epon 828 matrix. The constitutive curves for the three matrices are shown in **Figure 3.1.2.**

3.3 Single Fiber Micro Indentation Test

In this research, the single-fiber micro-indentation technique is used to evaluate the equivalent interfacial modulus of an aluminum-2024 fiber/Epon-828 matrix composite. While the interfacial shear strength equation developed by Mandell et. al. [7] and the Dow Chemical Company [28] was based on composite systems with a medium fiber volume fraction (typically between 36 and 50%) [7], the proposed single fiber micro indentation test uses a single fiber composite sample with the fiber volume fraction typically below 1%. Therefore, a new data reduction scheme has to be developed for the single-fiber micro-indentation test. In Mandell et. al.'s approach, the indenter load and indenter displacement for debonding are obtained from the experiment; however, only the indenter load for debonding is needed for calculation of the interfacial shear strength. In this research, the Kelly & Tyson equation originally developed for the single-fiber fragmentation test was modified and was combined with the fiber strain energy equation to derive the mean/average interfacial shear stress as a function of the indenter load and displacement. A mean interfacial shear stress-pseudo shear strain relation was derived and a pseudo shear modulus evaluated. The effects of fiber diameters and matrix

properties on the interfacial shear stiffness were evaluated using the modified Kelly & Tyson equation and a finite element analysis. Some interfacial parametric values obtained from the modified Kelly & Tyson equation were compared to those from the finite element analyses.

3.3.1 Analytical Derivation

The single-fiber micro-indentation specimen can be prepared in the same manner as the single fiber fragmentation specimen such that the differences in experimental parameters can be reduced to a minimum between these two tests. The fiber volume fraction for the single-fiber micro-indentation specimens is typically less than 1%. The interfacial shear strength equation developed by Mandell et. al. and Dow Chemical Company, however, was for composites with medium fiber volume. Thus a different data reduction scheme has to be developed for the single-fiber composite specimen. To this end, the Kelly-Tyson equation for the single-fiber fragmentation test is modified. From the free body diagram of an isolated filament, **Figure 3.3.1**, a force balance equation for fiber axial and interfacial shear stresses can be written. It was found in a preliminary study that the interfacial shear stress, τ, approaches zero at the free surface and rapidly rise to maximum at a quarter of a fiber diameter below the free surface and gradually diminishes to zero at a certain fiber diameters away from the free surface. The length where the interfacial shear stress vanishes is defined as the perturbed length, L_p. A mean interfacial shear stress, τ_m, can be defined as

$$\tau_m = \frac{1}{L_p}\int_{z=0}^{z=L_p} \tau(z)\, dz \qquad (8)$$

where z is the coordinate axis along the fiber with the origin at one fiber end opposite to the indented fiber end. The original Kelly & Tyson equation in the differential form as can be derived from force balance of an isolated filament is

$$\frac{d\sigma_f}{dz} = \frac{4\tau}{d_f} \qquad (9)$$

where σ_f is the fiber axial stress, d_f is fiber diameter, and τ is the interfacial shear stress. After integrating **equation (9)** and assuming that fiber axial stress distribution is linear with a maximum at the indented fiber end and zero at the perturbed end, an expression for the maximum fiber axial stress, $\sigma_f^{max.}$, at the indented fiber end can be obtained

$$\sigma_f^{max.} = \frac{4\tau_m L_p}{d_f} \tag{10}$$

The indenter load, P, can be expressed as

$$P = \tau_m * \pi d_f L_p \tag{11}$$

Because the data reduction scheme is for obtaining the interfacial shear strength for debond initiation, matrix deformation and strain energy are insignificant and are neglected. The applied external work, W, by the indenter load can be assumed to be equivalent to the fiber strain energy

$$W = \frac{1}{2} P * Z_i = \int\int \sigma d\varepsilon dV \tag{12}$$

where Z_i is the indenter displacement, and σ is the average fiber axial stress, which is one half of the maximum fiber axial stress at the indented fiber end. **Equations (10) & (11)** can be combined and rearranged to obtain a non-dimensional relationship between the indenter load and displacement:

$$\left(\frac{P^2}{8\pi^2 r_f^4 E_f^2}\right) = \left(\frac{\tau_m}{E_f}\right) * \left(\frac{Z_i}{r_f}\right) \tag{13}$$

where r_f is the fiber radius, and E_f is the fiber axial modulus. In addition, the mean

interfacial shear stress, τ_m, and the perturbed length, L_p, can be easily calculated from the indenter load, P, and indenter displacement, Z_i:

$$\tau_m = \frac{P^2}{Z_i}(8\,\pi^2 r_f^3 E_f)^{-1} \tag{14}$$

$$L_p = 4\,\pi\, r_f^2\, E_f\,(\frac{Z_i}{P}) \tag{15}$$

3.3.2 Finite Element Modeling

A finite element analysis of the single-fiber micro-indentation technique is performed to asses the accuracy of the modified Kelly & Tyson equation and evaluate the effects of fiber diameter and matrix stiffness on the test results and the pseudo interfacial shear modulus. A simplified two-phase (fiber and matrix) axisymmetric model is used in this study. The finite element model and the associated boundary conditions are similar to the four-phase model used in the in-situ micro indentation test except for the change in dimensions and phases, **Figure 3.3.2**. The fiber aspect ratio is about 50 for aluminum alloy wires with a nominal diameter of 100 microns. The matrix boundary is 2000 microns, which translates into a fiber volume fraction of 0.25%. The material behavior for aluminum alloy and Epon 828 matrix are linearly elastic/non-linearly plastic and are shown in **Figure 3.3.3**. To study the fiber diameter effect on the development of interfacial shear stress, single-fiber composite models with aluminum alloy fibers of 100 and 75 microns in diameter embedded in the standard Epon-828 14.5 phr of mPDA matrix (designated as stiffness matrix in **Figure 3.3.3b**) are established. For studying the effect of matrix properties on interfacial shear stress development, single-fiber composite models with aluminum fibers of 100 microns in diameter embedded in standard Epon-828 14.5 phr of mPDA matrix (stiff matrix) and a fictitious more compliant matrix (compliant matrix) are analyzed. The indenter is a flat-end cylindrical column with indenter diameter of 80 and 60 microns, for fibers of diameter of 100 and 75 microns, respectively. In addition, a finite element model for in-situ carbon fiber/Epon 828 matrix composite was established to evaluate the effectiveness of the modified Kelly & Tyson

equation in reducing the experimental data for in-situ composite. The fiber is a typical transversely isotropic AS4 fiber with E_{11}= 241 GPa, E_{22}= 21 GPa, ν_{12}= 0.25 and G_{23}= 8.3 GPa. Two matrices were used. The constitutive matrix properties are the same as those used in the single-fiber aluminum composites, **Figure 3.3.3b.** The fiber volume fraction is 0.36. Two fiber sizes, 6 and 8 microns in diameter, are used. The objectives are to validate the effectiveness of the modified Kelly & Tyson equation and to evaluate the effects of matrix properties and fiber sizes on the interfacial properties of the in-situ composites. For a carbon fiber composite, the indenter is not flat at its end but is of spherical shape. The indenter tip radii are 10 and 7.5 microns for carbon fibers with 8 and 6 microns in diameter.

3.4 Dynamic Mechanical Analysis for Interphase Modulus Characterization

Recently, there have been studies to investigate the use of Dynamic Mechanical Analysis as a tool for accumulating information about the interphase. With a new generation of DMA, there are new possibilities for detecting an interphase on composite materials. Dynamic mechanical properties are important factors to consider in the design and application of composite material structures. Young's modulus and internal damping are two such properties and are measures of the stiffness and energy dissipation ability of a substance. Damping, though not fully understood, is a good indication of a wide variety of molecular motions, relaxation processes, transitions, structural homogeneities and morphologies, all of which affect a material's mechanical behavior. In addition it reduces vibrations and prevents excessive amplitude build up at resonance frequencies by dissipating energy as heat. A complex Modulus E* is defined with the real and imaginary components E' and E", and these are known as the storage and loss modulus, respectively. In particular the most useful parameter, tan Delta is the ratio of energy lost/energy stored per deformation cycle, i.e. E"/E' [33]. In **Figure 3.4.1** the oscillating behavior of materials and the complex modulus are described. The tan Delta curve exhibits a series of peaks as the temperature is scanned upwards from sub-ambient to the final melt state.

With Dynamic Mechanical Analysis (DMA), the glass transition temperature of a polymer can be detected. The glass transition is a step-change in the mobility of polymer molecules in the amorphous region of the polymer. The polymer structure is loosening

and allows segmental and other molecular group motion. At temperatures below the glass transition, mobility is restricted resulting in a hard rigid structure. Above the glass transition, the material is viscous or rubbery. Due to the significant property change above the glass transition, the material also has a higher heat capacity and a higher coefficient of thermal expansion. In the region of a glass transition, the modulus undergoes relaxation and the damping curve goes through a maximum [34]. The glass transition temperature (Tg) of a fiber reinforced composite is actually the temperature at which changes in thermodynamic properties of the matrix occur since commonly used fiber reinforcements such as carbon and glass fibers as well as aluminum wires do not exhibit such behavior in that temperature region.

3.4.1 The DMA Technique

The Dynamic Mechanical Analyzer (DMA) measures the modulus (stiffness) and damping (energy dissipation) of a material as the material is deformed under periodic stress. The technique is useful for evaluation of viscoelastic materials such as polymers which exhibit time, frequency, and temperature dependent behavior. The DMA can provide information about quantitative modulus, primary and secondary transition temperatures, rate and degree of cure, viscosity and time depending behavior. Polymer research benefits from this information in the fields of blend comparability, processing effects, additives, matrix and branching effects, and isotropic effects. The DMA consists of five main components: the drive motor, the drive shaft and suspension, the sample clamping, the temperature control system, and the displacement sensor. The drive motor supplies a preset sinusoidal deformation. The drive shaft and the suspension transfer the force to the sample. The displacement sensor measures the actual sample deformation under the applied force. Depending on the deformation mode, there are different sample clamps that maintain the sample in the specific configuration. The temperature control system, consisting of the furnace and the cryogenic unit maintains the temperature and the ramp rate over a wide range. The DMA has multiple modes of temperature operations. In the ramp mode the temperature can be increased at a constant ramp rate. In the step & hold mode the temperature rises in isothermal steps. The temperature can also be held isothermally for the duration of the test.

Atkinson and Jones [35] found evidence with a first and second generation Dynamic Mechanical Analyzer (DMA) in a cantilever bending deformation mode, that the surface treatment of fibers and the resulting fiber-matrix interphase have an influence on the glass transition temperature of a composite material. With the third, more sensitive generation of a DMA, more information about interphases might be obtained. A different deformation mode, the tensile mode, is more suitable for gaining further information about the effect of the interphase on the loss and storage modulus and the glass transition of a composite material.

In this research, the following steps are to be taken:

- A new single fiber reinforced composite sample design is to be developed for interphase tests in the cyclic tensile deformation measurement mode of a Dynamic Mechanical Analyzer.
- Known aluminum wire/epoxy composites are to be investigated for their interphase mechanical and viscoelastic properties.
- The ideal test parameters for the investigation of the fiber-matrix interphase are to be found.
- The effect of polymeric interphases or thicknesses on the toughness and viscoelastic response of composite materials is to be determined using dynamic mechanical analysis.

3.4.2 Material Selection

The reinforcing fiber chosen for this investigation was an aluminum alloy 6061 wire with a diameter of 250 microns (10 mil) to be used in a single fiber composite. This moderate strength wire has proven to be quite easy to handle without being damaged during the process of manufacturing. The wire was produced by the California Fine Wire Company in Grove City, California. The alloy consists of 97% aluminum, 1% Magnesium, 0.6% Silicon, 0.28% Copper, and 0.2%Chrome by weight. A pure Aluminum wire was also tested but broke easily while handling the samples. The mechanical properties of different available Aluminum Alloys are given in **Table 3.4.1**.

As a matrix for this composite sample, epoxy resins cured with two different curing agents were chosen. The term "epoxy" refers to the reactive chemical group

consisting of an oxygen atom bonded to two other carbon atoms in a trigonal geometry. The chemistry of an epoxy is unique among thermosets, because of the wide spectrum of different mechanical properties that result from a variety of curing agents. Only a minimum pressure is necessary for the fabrication techniques and the volumetric shrinkage during curing is much less than encountered in many other systems. This means reduced stress in the cured final product [36]. A diglycidyl ether of Bisphenol-A (DGEBA), Epon 828 Shell Chemical Company, was used for all of the test samples.

In order to get two different matrixes with different mechanical and especially viscoelastic properties, the two chosen curing agents were meta-phenylenediamine (mPDA) and a polyetherdiamine (T-403 Jeffamine). The chemical structure is seen in **Figure 3.4.2**. In Dynamic Mechanical Analysis the different viscoelastic properties are easy to distinguish. The epoxy cured with T-403 Jeffamine has a glass transition temperature (Tg) of 97 °C, which is far below the glass transition temperature of the epoxy cured with mPDA (180 °C). The epoxy cured with mPDA results in a high modulus matrix, while a compliant matrix is achieved by curing the epoxy resin with T-403 Jeffamine.

3.4.3 Experimental Methods

The samples were tested by Dynamic Mechanical Analysis and were examined afterwards in the Environmental Scanning Electron Microscope.

Dynamic Mechanical Analyzer (DMA) in Tensile Mode. The Rheometric Scientific DMA (former Polymer Labs) can be used in several different deformation measurement modes. It enables bending, shear, tension and compression modes to be placed on the sample. The mounting may be vertical or horizontal. For this investigation the tensile mode and a vertical mounting was chosen in order to work with single fiber composites.

The DMTA covers a dynamic range of 4.5 decades and has a frequency range of 0.01Hz - 200Hz in 16 steps. With the cryogenic unit attached, the samples can be tested in a temperature range from -150 °C to +500 °C with a resolution of 0.1 °C. The temperature ramp rate was 5 deg/min if not otherwise noted and was started at least 60 °C

below the expected Tg point. Also all the tests were done with a frequency of 1Hz and a strain of 10 microns, if not otherwise noted.

The clamping arrangement consists of a fixed clamp frame fitted to the four ceramic clad support pillars and the tensile T-bar tool fitted to the drive shaft adapter. Clamp bars are fitted to both clamps, as seen in **Figure 3.4.3** and in the photos of **Figure 3.4.4.** The drive shaft motion is in the direction of the fiber and the cyclic displacement can be chosen between 10 microns and 128 microns. The sample length is determined by the distance between the fixed clamp and the drive clamp. The maximum length is 25mm. A static force is applied to prevent buckling of the sample. The static force therefore has to be higher than the dynamic force. The combined maximum force is mechanically limited to 15 Newton (1500 grams).

The design enables absolute measurements of length to a 1 micron accuracy to be made. The instrument performance is enhanced by a Pentium 133 PC with DOS based software. Experimental data includes E', E", tan Delta, and the displacement data.

The measurement of the glass transition point may vary in literature between the temperature of first deviation, temperature of return to baseline, extrapolated onset temperature, extrapolated endset temperature, midpoint temperature, and the damping peak temperature. In this investigation, the glass transition always refers to the damping (tan Delta) peak temperature.

DMTA - Stress vs. Strain Experiments. Another deformation measurement mode of the Dynamic Mechanical Analyzer is the stress/strain mode. The clamping is identical to the tensile mode and the same kind of sample is used as in the dynamic tension tests. In the stress/strain mode only a static force is applied to the sample. The instrument increases the static force over a set ramp rate and measures the resulting displacement. The maximum static force on the Rheometric Scientific DMA Mk III is 15 N equivalent to a load of 1500 grams. The maximum ramp time is 10 minutes, so the computer software calculates the force ramp rate. With the maximum time and the maximum force, the load ramp rate calculates to 0.025 Newton (2.5 grams) per second. With the composite sample tested in the tensile mode, this experiment resembles a fiber pull out

test. A fiber with a diameter of 250 microns diameter though could not be pulled out with the available load.

Environmental Scanning Electron Microscope. To determine the thickness of the actual coating on the fibers, a Philips 2020 ElectroScan Environmental Scanning Electron Microscope (ESEM) was used. ESEMs and SEMs (Scanning Electron Microscopes) offer superior performance compared to light microscopes, particularly in resolution, depth of field, and microanalysis. The ESEM is slightly different than a SEM in its multiple aperture, graduated vacuum system. This ESEM system maintains a high vacuum in most of the electron column while permitting relatively high pressures of water (12 torr) in the sample chamber.

The composite samples were cut in half, cast into a 25 mm diameter ring, and polished at the surface. Observation of polished surfaces made the actual size of the coating visible and easy to measure. Pictures were taken of the polished surface. This method is more precise in distinguishing the coating thickness, than measuring the weight gain. The weight percentage of the coating can be calculated from the thickness-measurement.

3.4.4 Sample Dimensions

Four different kinds of samples as seen in **Figure 3.4.5** have been tested:

Wire Sample. Plain wire was tested first, to find the ideal diameter within the mid force range of the instruments capability. Pure aluminum wire with a diameter of 125 and 250 microns could not be used because the initial application of the static force at the beginning of the test exceeds the strength of the wire. Aluminum Alloy 6061 wire with a diameter of 125 micron was then tested, but it was difficult removing cast samples out of the mold without damage. In addition to the fiber diameter the sample length was varied to keep the static force within the instrumental limits. A free fiber length of 10 mm plus the clamping length a the diameter of 250 microns was picked after these pretests providing the best sample configuration.

Epoxy Matrix Sample. The second kind of tested samples were pure epoxy matrix samples, which are 4 mm wide, 1.3 mm thick and about 25 mm long. The actual

effective sample length for the test is again 10 mm, the additional length is for secure clamping.

Composite Sample. The single wire was embedded in a epoxy matrix to form the composite sample. The dimensions are identical to the matrix sample.

DMA Sample. In the DMA samples there is a free fiber length in which the wire is not surrounded by any matrix. This free fiber length has been varied from 1mm to about 6 mm. In this configuration there is load transfer between the matrix and the fiber.

3.4.5 Sample Preparation

For the fabrication of the DMTA Samples a "dog-bone" mold was chosen. The size of the dog-bone coupons is ideal for DMTA testing and the mold is standardized for the single-fiber-fragmentation-test (SFFT). The SFFT dog bones have a gage section of 3.18 mm x 1.59 mm x 25.4 mm (1/8 in. x 1/16 in. x 1 in.). An aluminum master mold, which is used to prepare the sample silicone mold, already existed. Slots are molded in the center of each dog bone to a depth of 0.79 mm (1/32) inch and through the end of the silicone piece for positioning the wire.

For cure temperatures below 200 °C, RTV 664 two part silicone rubber molding compound made by General Electric has been found to be acceptable. The molds are fabricated in the following procedure:

1. Silicone rubber compound and curing agent are mixed at a ratio of 10 : 1 (75g : 7.5g) and thoroughly stirred.
2. The mixture is evacuated for five minutes in a vacuum jar to remove the enclosed air bubbles.
3. After the aluminum master mold is cleaned with acetone, the silicone rubber mix is poured into the aluminum mold.
4. The mold is set at a level surface and cured at room temperature for 24 hours.
5. The silicone can be peeled away from the aluminum master mold and is post-cured at 150 °C for 1 hour in a special oven only used for silicone compounds.

3.4.6 Resin Preparation

Epon 828 with Curing Agent mPDA. When Epon 828 is cured with the curing agent meta-phenylenediamine (mPDA) a high modulus epoxy matrix is achieved. The

mix ratio is 100g Epon 828 : 14.5g mPDA. The following preparation and curing steps are carried out:

1. Corresponding amounts of the resin and the curing agent are measured in disposable plastic beakers.
2. Both substances are heated to 75 °C in order to melt the curing agent, which is in a solid state below 69 °C. Depending on the amount of the curing agent it takes about 45 to 60 minutes to melt the mPDA.
3. Both substances are mixed after the curing agent becomes liquid. They are thoroughly blended.
4. To remove entrapped air bubbles, the epoxy mixture is degassed in a preheated vacuum oven for 10 minutes.
5. Upon removal from the vacuum oven the samples are cast as soon as the epoxy nears room temperature. The viscosity of the epoxy increases to a gel-like level within an hour.
6. The epoxy samples are oven cured for two hours at 75 °C followed by two hours at 125 °C.
7. The epoxy is not fully cured at this point, so that a post-curing of 175 °C in an inert-gas oven is necessary to fully cure this epoxy. The inert-gas oven has a ramp time of 40 minutes to reach 175 °C and cools down after two hours at 175 °C to 25 degrees room temperature in the same ramp time with nitrogen at a pressure of 0.5 psi.

Epon 828 with Curing Agent T-403 Jeffamine. Using the curing agent T-403 Jeffamine with Epon 828 produces a more compliant epoxy matrix compared to the Epon 828 / mPDA epoxy. The two constituents are mixed at a ratio of 100g Epon 828 : 45g of T-403 Jeffamine. For the curing of this epoxy the following steps are followed:

Both substances are liquid at room temperature, so they can be mixed and stirred without preheating. The materials are heated to 50 °C in a vacuum oven and then stirred together.

1. To remove the entrapped air bubbles, the epoxy is degassed in a vacuum oven for 15 minutes at a lower vacuum to keep it from foaming and 10 minutes at a high vacuum.

2. The blend has to cool down to room temperature before casting. The Epon-Jeffamine epoxy does not gel nearly as fast as the Epon /mPDA epoxy. The DMA Samples were cast after a one hour wait to increase the viscosity of the epoxy. Otherwise the epoxy would flow around the rubber parts and fill the gap.
3. The curing program for Epon 828 with T-403 Jeffamine is 24 hours at room temperature followed by 16 hours at 85 °C. But DMA tests showed that curing the samples at 85 °C for two hours and three hours at 125 °C proved to give the exact same mechanical properties and reduces the cure cycle time significantly.
4. Samples are allowed to cool slowly to room temperature before retrieving from oven. The Epon/Jeffamine samples are fully cured with this procedure, thus, there is no need for a high temperature post-cure.

3.4.7 Casting DMTA Test Samples

In the DMTA the samples are tested in the tensile mode. A sample length of 25 mm (15 mm clamping and 10 mm free length) has proven to be a good size to match the force and load capabilities of the Mk III DMA instrument. The samples were fabricated in the silicone "dog bone" mold as described.

1. The aluminum wires are wrapped around a 165 mm X 125 mm stainless steel frame. Eight wires fit on one frame. The frame is designed, so that it can be placed around the silicone mold while putting the wires in the designated slots.
2. A 4mm x 3mm rubber spacer with a thin slit is fitted into the mold around the wire, dividing the matrix of the dog-bone into two parts creating the free fiber length and keeping the fiber in the right place. This free length was chosen to be 5 mm.

Coating of 10 mil Aluminum Alloy 6061 Wire. Coating an aluminum wire with an epoxy coating thicker than 2 microns was difficult. A uniform coating was not achieved in a solution of more than 5% epoxy. Due to surface energy forces causing retraction of the film into spheres, droplets were formed on the wire at higher solution concentration. In addition to acetone, toluene and NMP (N-Methyl-2-Pyrrolidinone) were examined as solvents and gave similar results, but acetone is the lowest health risk and was chosen. As discovered later, the fully cured Epon/T-403Jeffamine epoxy will still dissolve in acetone. This makes multiple coating of a fiber very troublesome.

The aluminum wires are mounted on a stainless steel frame. The following procedure was used:

1. 15 grams of the Epon 828/ T-403 Jeffamine epoxy is prepared in a beaker as described above and is cured at room temperature for 30 minutes.
2. Acetone is then added to the epoxy to form a 5% solution. This solution is poured in a stainless steel pan.
3. The wires mounted on the frame are lowered into the pan for 30 seconds, while gently stirring the solution by moving the pan.
4. The frame is taken out of the solution and immediately put into a position where the wires held vertical.
5. The frame is mounted to a motor and rotated at about 15 revolutions per minute for two hours in order to eliminate the gravity influence and achieve a uniform coating. An schematic of the motor bench is shown in **Figure 3.4.6**.
6. After a curing cycle of 2 hours at 85 °C and 3 hours at 125 °C the wires are coated again to increase the thickness of the coating. The additional coating steps don't increase the coating themselves, because the previously deposited coating dissolves again.
7. When the desired thickness is reached, the wires are further processed like the "as received" wires.

4. RESULTS AND TECHNICAL DISCUSSION

4.1 Single Fiber Fragmentation Test

4.1.1 Effect of matrix strain state

The axial stress distribution in the fiber and the shear stress distribution in the interphase are of primary interest in this analysis. The fiber axial stress distributions for fragments created at 1% and 2% matrix strains under the applied displacement loading are shown in **Figure 4.1.1**. The fiber axial stress increases from zero at the fiber break (z/d_f=63.25, where z is the axial distance from the coordinate zero, **Figure 3.1.1**, and d_f is the fiber diameter) to a plateau value at a certain length away from the fiber break. If we define a characteristic in-effective length as the length within which the fiber axial stress recovers 95% of its far field value (the plateau), the in-effective length for

fragments created at 1% and 2% matrix strains are 46.5d_f, and 54.25d_f, respectively, for an applied strain ε=1.58%. Physically, the in-effective length is equivalent to the stress transfer length. As the applied relative strain increases, the in-effective length increases. The stress transferred to the fiber is higher for fragments created at lower matrix strains than the fragments created at higher matrix strains for the same given displacement loading. The maximum stress transferred to the fiber are 3034 MPa and 2185 MPa, respectively for fragments created at 1% and 2% matrix strains. This implies that when the matrix becomes more compliant, the stress transfer is less efficient and it requires longer fiber length to complete the stress transfer between the fiber and the matrix. It might be argued that the decrease in the maximum stress transferred to the fiber is a result of the decrease of the applied load at the boundary edge. When the matrix is more compliant, the loading required at the boundary edge to create the same displacement is less; thus the stress transferred to the fiber is accordingly less. The interphase axial stress distribution is of similar pattern to the fiber axial stress distribution, **Figure 4.1.2.** It is zero at the fiber break and increases gradually to a plateau value. The maximum axial stresses for the fragments created at 1% and 2% matrix strains are 55 MPa and 50 MPa, respectively. The bulk tensile strength for the interphase material, Epon 828 with 7.5phr of mPDA, is 44 MPa [25]. However, when the interphase is constrained by the fiber and matrix and thus subject to a hydrostatic pressure, the strength of the interphase is expected to be higher than in the bulk state [37]. The interphase strength is equivalent to its bulk strength multiplied by a enhancement factor (>1). If the enhancement factor is 1.5, then the interphase strength is approximately 66 MPa and the interphase will not fail through interphase fracture. Nevertheless, the interphase shear failure will precede the tensile failure due to shear stress singularity at the free edge as will be discussed in the following section.

The shear stress distributions at the interphase for fragments created at 1% and 2% matrix strains are shown in **Figures 4.1.3a&b**. The shear plateau near the fiber breaks in each case is a result of matrix plasticity. Similar plateaus are found in the matrix shear stress distributions. It is shown in **Figures 4.1.3** that the maximum shear plateau stresses induced in the interphase for fragments created at 1% and 2% matrix strains are 39 MPa

and 24 MPa, respectively. The large shear stress plateau for fragments created at 1% matrix strain correspond to a higher fiber axial stress plateau as shown in **Figure 4.1.1**. The shear strength of the bulk interphase material, as derived from **Figure 3.1.2** and based on the von Mises criterion, is approximately 26 MPa. If an enhancement factor of 1.5 due to constraint is used, the interphase strength is approximately 39 MPa, which is about the shear plateau value in **Figure 4.1.3**. In this regard, the interphase shear stress will reach the interphase shear strength before the tensile stress reaches the interphase tensile strength. In summary, the fragment created at 1% matrix strain is more likely to have interphasial shear failure (debonding) than the fragments created at 2% matrix strain. For fragment created at 2% matrix strain, the shear stress distributions, **Figure 4.1.3b**, and the fiber axial stress distributions, **Figure 4.1.1b**, converge as the applied load increases. This implies that upon further loading the fiber will not be subject to any more loads and the matrix will have to carry more tensile loads which eventually will cause matrix failure. Even if the plateau does not exceed the interphase shear strength, debond will occur at the fiber break where the interphase shear stresses are singular. The effect of interphase shear stress singularity will be discussed in the next section.

4.1.2 Stress Singularity at Free Edge

The stress singularity at the free edge of the bi-material interface has been extensively studied [38-43]. A free edge is defined as the intersection of an interface plane (between two dissimilar materials) and the free surface of a structure. The nature of the singularity depends on the property and anisotropy of the bounding materials as well as the geometry of the free edge of the structure. For elasto-plastic material, such as the matrix material in this study, a stress singularity does not occur due to the formation of plastic zones in the matrix. Since the interphase is linear elastic, a shear stress singularity does occur even at the presence of matrix plasticity. The exact value of the singularity cannot be obtained without the knowledge of the nature of the singularity. For finite element analysis, special elements with a displacement function which incorporates the exact order of singularity have to be applied to the free edges to obtain a better approximation of the singular values. It is not the purpose of this study to investigate the

nature of the stress singularity; thus only the effect of the stress singularity will be discussed.

There are two free edges in this fiber-interphase-matrix model. One is the fiber/interphase free edge and the other is the interphase/matrix free edge. On the matrix side of the interphase/matrix free edge, the stress singularity does not occur due to the matrix plasticity at high strains. On the fiber side of the fiber/interphase free edge, there is a shear stress concentration at regions immediately neighboring the free edge; however, the stress is not singular. On the interphase side of the interphase/matrix free edge, stress singularity is expected because this free edge is right under the loading points. The shear stress on the interphase side of the fiber/interphase free edge is also singular because the interphase is very thin that the free edge is immediately neighboring the loading points. In addition, the presence of two dissimilar materials at the interface gives rise to oscillating singularities [43, 44] at the free edge and at the debond end, **Figure 4.1.3**, which are not present in the elastic fracture mechanics of homogeneous solids.

4.1.3 Interphase Debonding

Because the singular shear stress at the free edge of the interphase exceeds the interphase shear strength, the interphase will fail by shear which will cause interphase debonding at the fiber breaks. It is not certain, however, whether debond will propagate along the fiber/interphase interface or the interphase/matrix interface. One way to decide if debond propagation will occur is to compare the strain energy release rate for the two debond cases with the corresponding interface toughness. If the energy release rate is below the critical strain energy release rate (fracture toughness), crack or debond growth will not occur. However, the critical energy release rate, or the fracture toughness, of the interface of a bi-material is not immediately known. From mechanics point of view, the interface toughness depends on the material properties of the joining materials, the crack geometry, the loading condition and the mode mixity. In this study, the dominant factors for fracture toughness such as crack geometry and loading conditions are similar for the two debond cases. Thus it is expected that the fracture toughness for the two debond cases is not much different. However, a very important factor for interface shear strength evaluation, which is usually ignored in the micromechanics study, is the adhesion

between two dissimilar materials. It is believed that for most sizing processes, the adhesion between the interphase and matrix is stronger and debond is more likely to occur at the fiber-interphase interface.

4.1.4 Critical Length

When the first fiber fracture occurs, the fiber ends will debond right after the fracture. Then the fragment will fracture again at a higher applied strain. Debonding will occur at the new fracture end due to the shear stress singularity and in the case when the matrix stiffness is high enough to raise the interphase shear stress above the shear strength. However, debonding at the two fracture ends occurs at different stage of matrix strains; thus the debond propagation and debond length will be different. This might explain the experimentally observed unsymmetric photoelastic stress patterns at the two fiber ends of a fragment [1].

Fragments created at early stages of the fragmentation process will continue to fracture until a critical length is reached. It was shown in the previous section that the ineffective length changes with the matrix strains. Therefore, at the final stage of the fragmentation test, all fragments will have different debond lengths and the critical length will have a statistical distribution which may be one of the causes for the large variation in the experimentally determined critical length.

If the fiber-interphase bonding is strong, then debond propagation is less likely and the "critical length" will be shorter. Thus the fragmentation test in this respect is like a fracture toughness test for the fiber-interphase interface. The apparent interfacial shear strength obtained based on the simplified shear lag model and the experimentally measured critical length is should be regarded as an interphasal adhesion index qualitatively rather than the interfacial "strength" quantitatively.

4.1.5 Effect of Interphase Property Gradients

In some applications, a distinct third-phase material is coated to the fiber for specific performance requirement [27]. The coating, or the interphase property usually is regarded as homogeneous. However, when the fiber is subject to sizing treatment [1], the interphase is heterogeneous with properties varying continuously from the fiber-interphase boundary to interphase-matrix boundary. Several micro-mechanical

investigations have been conducted to evaluate the effect of interphase property gradients on the stress fields [45,46]. These theoretical calculations have been based on concentric-cylinder models. It was found that the stress gradients affect the local (interphase) stress fields. The interphase property effect studied by Jayaraman and Reifsnider [46] included uniform, linear, parabolic and power-law interphase property gradients. In their models the interphase property gradients are of different shapes so that the effective or average interphase properties are different and hence the interphase stress fields are not the same. The purpose of this portion of the study is to investigate if the interphase stress fields or the stress transfer will be affected by different interphase property distributions when the effective interphase properties are the same. If the stress fields are not affected by the interphase property gradients, then a uniform interphase property can be assumed in the micromechanical model which will greatly simplify further studies of the effects of other interphase parameters.

In this analysis, three types of interphase property gradients (uniform, linear and power-law) are assumed, **Figure 4.1.4**. Despite these interphase property gradients, the average interphase properties for these three types of property gradients are the same. The analysis shows that the fiber axial stress distributions and the interphase shear stress distributions along fiber-interphase interface for the three interphase property gradients are virtually the same, **Figures 4.1.5 & 4.1.6**. It should be emphasized that sizing does produce interphase property gradients and the distribution of the interphase property gradient does affect the average or effective interphase property and hence the stress fields. However, in the micro-mechanical study, we can average the property gradient and assume a homogeneous interphase. The effect of the interphase modulus variation as a result of the property gradients on the stress transfer and local stress fields is discussed in part II of this series of investigation.

4.1.6 Effect of thermal residual stress

Over the years, thermal residual stress has been a concern for composite structure design because it affects the stress state of the composite material and in most cases weakens the composite structure. Thermal residual stresses develop after composite fabrication or processing as a the result of the mismatch among the moduli and thermal

expansion coefficients of the constituents. Whitney and Drzal [11] used a analytical, linear elastic model to investigate the effect of thermal residual stresses on the stress fields of a single-fiber fragmentation specimen and found that the residual stresses increase the radial pressure at the fiber/matrix interface while the other stress components are not significantly affected. In this section, the study of thermal residual stress effect is extended to a specimen with nonlinear elastic/plastic matrix behavior.

The single-fiber fragmentation specimens are cured at 75°C and postcured at 125°C. The specimens are then tested at room temperature, 21°C. The difference between the postcure and room temperature is δT=-104°C. However, because some relieving of residual stresses occur during cool down, a value of δT=-70°C is chosen for the analysis. It is found that the thermal residual stresses reduce the stress transfer efficiency. The maximum stress transferred to the fiber is smaller when thermal residual stresses are present, **Figure 4.1.7**. The shear stress distribution is shown in **Figure 4.1.8**. The maximum shear plateau stress is restrained by the matrix plasticity and is not affected by the thermal residual stresses. However, the shear stress descends to zero more rapidly. In addition, the interphase axial stress increases significantly due to the presence of thermal residual stresses, **Figure 4.1.9**; hence interphase fracture is more likely to occur.

The radial and shear stress distributions along the radial direction on a plane at a distance 9.24 fiber diameters away from the fiber end are shown in **Figure 4.1.10**. The shear stresses reach a maximum at the interphase and decrease to zero at the matrix free surface and the fiber axis. The radial stresses are maximum at the fiber surface, remain constant inside the interphase and gradually reduce to zero at the matrix free surface. When thermal residual stresses are present, the radial stresses become more compressive at the interphase. This finding agrees with the prediction from the linear analysis of Whitney and Drzal [11]. The shear stress distributions for δT=0 and δT=-70°C cases are similar in the fiber and the matrix regions. However, the shear stresses in the interphase are decreased as affected by the thermal residual stresses.

4.1.7 Stress Transfer for Low Aspect Ratio Fragments

In this section, stress transfer for fragments shorter than the critical length is evaluated. The aspect ratio for the fragment studied is L/d_f=42, which is about five

diameters shorter than the critical length as derived from **Figure 4.1.1**. The fiber axial stress and interphase shear stress distributions are shown in **Figure 4.1.11**. As expected, the fiber axial stress never reaches a plateau and the stress transfer to the fiber is ineffective for the whole fragment length because the shear stress never decays to zero value as was the case for long aspect ratio fragments as shown in **Figure 4.1.3**. It implies that during the deformation process the tangential component of displacement between fiber and matrix is discontinuous for the whole fragment length. However, the interphase shear stress reaches the same plateau as that of the long aspect ratio fragment. Thus the short fragment debonds in the same way as the long fragments do as long as the fragments were created at the same time.

4.1.8 Linear vs. Nonlinear FEM

Finite element analyses have been applied to investigate the stress transfer mechanism of the single fiber fragmentation test [14,16, 18-22]. However, most of the studies used models which are more appropriate for discontinuous short fiber composite [14,18-21]. For models more appropriate for continuous fiber composite, linear analysis was performed [17,22]. It is known, however, that the matrix behavior is non-linear elastic/plastic. The matrix stiffness decreases significantly with increasing matrix deformation. Thus the adequacy of the finite element analysis assuming linear elastic matrix properties for the evaluation of stress transfer between fiber and matrix is questioned. In this section, the stress distributions in the fragments from results of finite element analyses assuming linear and nonlinear matrix properties are compared. The fiber axial and the interphase and matrix shear stress distributions from finite element analysis assuming linear and nonlinear matrix properties are shown in **Figures 4.1.12a&b**. For linear analysis, the interphase stiffness is 1.5 times the matrix initial stiffness. For nonlinear analysis, the initial matrix state in the model is the zero strain state. The maximum fiber axial stresses are 3649 MPa and 3331 MPa, respectively for linear and nonlinear analyses. The interphase shear stress is singular at the free edge for both linear and nonlinear analyses. When the stress data for the element at the free edge is ignored, the interphase and matrix shear stresses are approximately the same from the linear analysis though the interphase stiffness is 1.5 times the initial modulus of the matrix,

Figure 4.1.12a. The shear stresses in the interphase and matrix at the fiber break are approximately 400 MPa. However, from **Figure 3.1.2a** and the von Mises criteria, the interphase (Epon 828 with 7.5phr of mPDA) and matrix (Epon 828 with 14.5phr of mPDA) shear strengths are 25 and 51 MPa, respectively. Thus the stress distributions in the region within six fiber diameters from the fiber break is nonrealistic. From the results of the non-linear analysis, it is shown that the stress transfer length (the section where the shear stress is not zero) is longer than that from the linear analysis. The interphase shear stress forms a plateau near the fiber break with a oscillatory singularity approaching the fiber break, **Figures 4.1.2&4.1.3**. In view of **Figures 4.1.12a&b**, it is concluded that linear analysis over-estimates the stress transfer efficiency and predicts a shorter stress transfer region. In general, linear finite element analysis might introduce errors in the parametric studies of the effect of constituent properties due to the neglect of the dominant effect of the non-linear matrix material behavior.

4.1.9 Effect of Interphase Debonding

It was shown earlier that interphase debonding accompanies the fiber fracture. Debonding occurs at the fiber/interphase interface due to the shear stress singularity at the free edge. In this section, the effect of debond length on the fiber axial and interphase shear stress distributions of the fractured fragment will be presented. The shear stress distributions for debond cracks 20 μm, 150 μm and 300 μm in length are shown in **Figure 4.1.13a**. For all debond cracks, frictional debonding between fiber and interphase is assumed. The coefficient of friction is assumed to be 0.6 for all cases. At regions close to the crack tip, oscillatory shear stresses are found. The interphase shear stress distribution is composed of four regions. The first region is the constant shear stress region as a result of constant friction force between the two debonded bodies. The second region is a shear plateau in front of the crack tip as a result of the perfectly plastic behavior of the matrix. The third region is the shear decaying zone. The fourth region corresponds to a zero shear stress zone where stress transfer does not occur. The size of the regions varies with the debond length. At the regions where the shear stresses are approximately constant, the fiber axial stresses are nearly linear, **Figure 4.1.13b**. Because the stress transfer efficiency for frictional debonding between the fiber and the

matrix is low, the stress transferred to the fiber is accordingly less for fragment with longer debond length.

In the debonded regions, the fiber carries very little longitudinal loading as a result of inefficient frictional stress transfer. The interphase thus is subject to a large tensile load, **Figure 4.1.13c**. Consequently, the interphase will fracture in the debonded region. These interphase fractures are stress raisers which might cause matrix cracks or yielding in a layered composite. Thus debonding not only affects the interphase stress transfer efficiency, it also affects the composite stiffness and strength.

4.1.10 Effect of Interphase Modulus

It has been shown in the linear finite element analyses that the interphase stress transfer is affected by the interphase modulus [16,22]. In a preliminary study by the authors, a linear finite element analysis was performed to evaluate the effect of interphase properties on the interphase stress transfer. The fiber is transverse isotropic with the same properties as the baseline model as shown in **Table 3.1.1**. The modulus of the matrix is 1.89 GPa with a Poisson's ratio 0.35. The Poisson's ratio of the interphase is assumed to be the same as that of the matrix. It was found that the maximum fiber axial stress increases when the interphase/matrix stiffness ratio (E_i/E_m) increases. But the increase of fiber axial stress is not monotonic with the increase of interphase stiffness. The fiber axial stress increases as E_i/E_m increases from 0.2 to 25. However, in the range of E_i/E_m=25 to 35, the fiber axial stress remains constant and begins to decrease when E_i/E_m is greater than 35. A plot of the maximum fiber axial stress against the interphase/matrix stiffness ratio is shown in **Figure 4.1.14a**.

A similar plot of maximum fiber axial stress against the interphase/matrix stiffness ratio from the nonlinear finite element analysis is shown in **Figure 4.1.14b**. From the results of nonlinear analysis, the fiber axial stress increases only 2% when the interphase/matrix stiffness ratio increases from 0.7 to 7.5, **Figure 4.1.14b**. However, the increasing trend reverses at E_i/E_m=10. Thus increasing the interphase stiffness does not always increases the stress transfer efficiency. And the optimal E_i/E_m ratio (from the stress transfer efficiency point of view) obtained from the linear analysis is three times larger than that from the nonlinear analysis. Nevertheless, the drawback of increasing the

interphase stiffness is that the interphase tensile stress will increase which in turn can cause interphase tensile failure.

The shear stress distributions for E_i/E_m = 0.7, 1.5, 7.5 and 30 are shown in **Figure 4.1.15b**. It is found that the shear stress distributions for these four cases are of similar shape except that the shear stress oscillates more violently for high E_i/E_m case. The shear stress distributions reach the same plateau as a result of matrix plasticity. It implies that the matrix behavior is the dominant parameter in the interphase shear stress transfer. The interphase tensile stress distributions, however, exhibit significant differences with increasing E_i/E_m ratios. **Figures 4.1.16a&b** are the interphase axial stress distributions for E_i/E_m = 0.7, 1.5, 7.5 and 30 cases. For E_i/E_m = 0.7, the interphase axial stress is low. For E_i/E_m = 1.5, the interphase axial stress is still less than its tensile strength. However, in the debonded region, e.g., from z/d_f=60.75 to 63.25, the interphase axial stress is high because the debonded fiber only carries a small amount of tensile load through friction stress transfer.

The interphase in the debonded region will fracture as discussed in the previous section. For E_i/E_m=7.5 and 30, the interphase axial stresses are very high, **Figure 4.1.16b**, the interphase will fracture in tension before undergoing shear failure. The effect of interphase fracture is investigated by introducing several transverse interphasial cracks purposely along the fragment. It is shown in **Figure 4.1.17** that interphase fractures introduce shear stress concentrations at the site of fracture, which in turn will cause interphase shear failure or debonding. Thus increasing the interphase stiffness has a adverse effect on the composite strength.

4.1.11 Effect of Interphase Thickness

The effect of interphase thickness on the interphase stress transfer has been evaluated by DiAnselmo et al. [22] and Fan & Hsu [20]. It was shown [22] that for E_i/E_m=2, the effective stress in the interphase is always larger than that in the matrix for interphase thickness ranging from 0.0015 d_f to 0.15 d_f. When the interphase is more compliant than the matrix, eg, E_i/E_m=0.1, the effective stress in the interphase is smaller than that in the matrix for interphase thickness greater than 0.006d_f. It was concluded

that the matrix might yield before interphase failure if the interphase is thick and the strengths of the interphase and the matrix are the same. A study by Fan & Hsu [20] showed that the stress transfer efficiency is much lower for the thickly coated fiber with a interphase/matrix modulus ratio E_i/E_m=0.15. Thus from their linear finite element analyses [20,22] it seemed that the evaluation of interphase thickness effect based on single E_i/E_m ratio is not conclusive. In this section, the effect of interphase thickness on the interphase stress transfer is evaluated for E_i/E_m=0.3 and E_i/E_m=1.8 cases, where E_m is the initial modulus of the matrix.

The fiber axial and interphase shear stress distributions for E_i/E_m=1.8 are shown in **Figures 4.1.18a&b**. When the interphase thickness increases from t_i=0.10 μm (=0.0125d_f) to 2.0 μm (=0.25d_f), the fiber axial stress increases 6%, **Figure 4.1.18a**, while the shear stress plateau increases 23%. Thus the stress transfer efficiency increases with the increase of interphase thickness at the expense of increasing the likelihood of shear failure. For E_i/E_m=0.3, when the interphase thickness increases from t_i=0.10 μm (=0.0125d_f) to 2.0 μm (=0.125d_f), the fiber axial stress increases 4%, **Figure 4.1.19a**, while the shear stress plateau increases 24%, **Figure 4.1.19b**. Unlike the results from Fan & Hsu in their study of discontinuous fiber fragmentation test, it is found here that the stress transfer efficiency increases with thicker interphase for both E_i/E_m >1 and E_i/E_m <1 cases.

4.1.12 Effect of Fiber Modulus and Fiber Diameter

The effect of fiber modulus on the interphase stress transfer is evaluated using finite element models of fragmented AS4 and Kevlar fibers. The matrix and interphase properties for the AS4 and Kevlar fragments are assumed to be the same except for the Poisson's ratio of the interphase for the Kevlar coupon. The constituent properties for these two models are shown in **Table 3.1.1**. Two sizes of fiber diameter are used for the Kevlar fiber case. In one case, the Kevlar diameter is assumed to be 8 μm, same as that of the AS4 fiber. In the other case, the Kevlar diameter is assumed to be 12.5 μm, which is the true diameter of the Kevlar fiber. It is assumed that there is no fiber-interphase

debonding. The numerical result is compared to the analytical results of Whitney and Drzal [11] in their linear analysis of a two-phase fiber fragment.

The axial stress distributions for AS4 and Kevlar fibers are shown in **Figure 4.1.20a**. It is found that the maximum axial stress for AS4 fiber is 1.9 times that of the Kevlar fiber of the same diameter while the longitudinal modulus ratio for the AS4 and Kevlar fibers is 1.7. The in-effective lengths (the length within which the fiber axial stress recovers 95% of its far field value) for AS4, Kevlar I (d_f=8 μm) and Kevlar II (d_f=12.5 μm) fiber fragments are 46.6, 33.3 and 42.1, respectively. The fiber axial stress in the AS4 fiber is higher than that in the Kevlar fiber due to the high stiffness of the AS4 fiber. The finding that the in-effective length of the Kevlar fiber fragment is shorter than that of the AS4 fiber fragment agrees well with that analytical results of Whitney and Drzal [11]. However, the experimental results showed that the critical length in the Kevlar coupon is longer than that in the AS4 coupon [11]. As discussed by Whitney and Drzal, the contradiction between the analytical and experimental results can be attributed to the failure mode of the fibers. The AS4 fiber reveals a brittle-type fracture, while the Kevlar fiber displays longitudinal splitting. The splitting of the fiber will cause longitudinal interphase cracks which in turn will cause debonding. Thus for the longitudinally split section of the fiber, the stress transferred to the fiber is very limited. Though the in-effective length of the Kevlar fiber fragment obtained from the finite element results of perfectly bonded model is shorter than that of the AS4 fiber, the fiber critical length is actually longer due to the splitting fracture of the Kevlar fiber.

The shear stress distributions for AS4, Kevlar I and Kevlar II fiber fragments are shown in **Figure 4.1.20b**. For AS4 and Kevlar I (d_f=8 μm), the maximum shear stresses are approximately the same. Only the length of the maximum shear plateau is different. Because the material property ratio of AS4/matrix is higher than that of Kevlar/matrix, the shear deformation at the fiber breaks for the AS4 fragment is accordingly higher. Thus the AS4 fragment has a larger shear plateau. For Kevlar fibers of different diameters, the increase of the fiber diameter enlarges the constraint area to the matrix. The increased constraints to the matrix by the fiber reduce the difference in the relative

displacements between the fiber and the matrix and hence reduce the maximum shear stresses.

4.1.13 Effect of Coefficients of Friction Between the Debonded Surfaces

When the fiber/interphase debonds, the interphase stress transfer is achieved through frictional stress between the fiber and the interphase. The frictional stress is dependent on the coefficient of friction, which in turn depends on the surface topology of the two contact bodies, and the normal force to the contact bodies. For a perfectly bonded fiber/interphase interface, the coefficient of friction between the two bodies is infinity. When the fiber and the matrix are totally separated, the coefficient of friction is zero. Between these two extremes, the coefficient of friction is high for rough or corrugated surfaces and is low for smooth contact surfaces. Because the coefficient of friction between the debonded fiber and interphase cannot be measured, it is only desired to evaluate the effect of coefficients of friction on the interphase stress transfer for the debonded fiber fragment. Note that the coefficient of friction cannot be assigned arbitrarily. There is an upper limit for the coefficient of friction. When the coefficient of friction exceeds the upper limit, the debond crack is not in equilibrium and the numerical iterations in the finite element analysis will not converge.

The fiber axial and interphase shear stress distributions for a fragment with 100 μm (12.5d_f) debond crack emanating from the fiber break are shown in **Figures 4.1.21a&b**. The coefficients of friction are 0.2, 0.6 and 1.0, respectively. The frictional force increases as the coefficient of friction increases. The overall stress transfer efficiency is higher for debonded surfaces with higher coefficient of friction. The fiber axial stress increases 5% when the coefficient of friction increases from 0.2 to 1.0.

4.1.14 Experimental Determination of the Interphase Shear Stress

In recent years, the laser Raman spectroscopy (LRS) technique has been used in combination with the single-fiber fragmentation test [47-49] to measure the interface shear strength. The idea is that when the fiber is under load, the shift in Raman frequency of the fiber has a linear relationship to the magnitude of the fiber axial strain. Thus the Raman frequency of the fiber can be converted to fiber strains. A curve-fit technique is applied to obtained the strain equation as a function of the distance from the

fiber break. A simplified equilibrium equation is then used to calculate the interfacial shear stress from the derived strain distribution equation. The drawback of this technique is the use of the curve-fit technique and the application of the simplified equilibrium equation to calculate the interface shear stress from the fiber strains.

The stress transfer equation frequently used in the literature is derived from a force balance of a volume element as shown in **Figure 4.1.22.** Consider an infinitesimal element of length dz with a distance z from the fiber break, the force equilibrium equation for the volume element illustrated in **Figure 4.1.22** requires that

$$\sigma_f \times \pi r^2 - (\sigma_f + d\sigma_f)\, \pi r^2 + \tau_{rz} \times 2\pi r \times dz = 0 \qquad (16)$$

or,

$$\tau_{rz} = \frac{1}{4} \frac{d\sigma_f}{d(z/d_f)} \qquad (17)$$

where σ_f, τ_{rz}, z and r are the fiber axial stress, the shear stress acting circumferentially on the interface, the axial coordinate and the fiber radius. Assuming isotropic fiber properties and applying Hook's law for uniaxial stress state, **equation (17)** can be converted to

$$\tau_{rz} = \frac{E_f}{4} \frac{d\varepsilon_f}{d(z/d_f)} \qquad (18)$$

where E_f is the Young's modulus of the fiber and ε_f is the fiber axial strain. Thus, the interfacial shear stress can be obtained by taking the derivative of the fiber axial strain distribution along the longitudinal z-axis. However, the conversion from **equation (17)** to **equation (18)** requires that the fiber is in a uniaxial stress state such that $\varepsilon_f = \sigma_f / E_f$. When the fiber is under multi-axial stress state, the fiber axial strain is

$$\varepsilon_Z = [\sigma_Z - \nu (\sigma_r + \sigma_\theta)]/E_f \qquad (19)$$

where ε_z, E_f, ν, σ_r and σ_θ are the fiber axial strain, the fiber modulus, the Poisson's ratio of the fiber, the radial and the hoop stresses applied to the fiber, respectively. For a transversely isotropic fiber, the fiber axial strain is

$$\varepsilon_z = \sigma_z/E_z - \nu_{rz}(\sigma_r + \sigma_\theta)/E_r \qquad (20)$$

where ε_z, σ_z and E_z are the fiber axial strain, fiber axial stress and fiber axial modulus, respectively, and σ_r, σ_θ, ν_{rz}, and E_r are the radial and hoop stresses, the Poisson's ratio and the transverse modulus of the fiber, respectively in the isotropic plane. The shear component does not appear in **equations (19) and (20)** because they are totally uncoupled in the principal material coordinates. Nevertheless, the fiber is subject to radial stresses due to the Poisson's contraction of the matrix, especially at regions near the fiber breaks. Thus for either isotropic or transverse isotropic fibers, the relation between the fiber axial stress and strain is not linear. Therefore, the derivation of interface shear stress distribution from **equation (18)** may introduce errors, especially at regions near the fiber break where large radial and hoop stresses are present.

In the experimental work, data scatter is always observed. In many situations, these data are curve-fit to obtain a smooth curve. However, further derivation from this fitted curve (eg, stress-strain curve) to obtain a secondary data set (eg, modulus) should be applied with care. The derivation of the secondary data set from the first data set have to be physically meaningful. The following example is a demonstration of the possible errors the curve-fitting technique might induce. Consider a fiber fragment containing an isotropic fiber with a Young's modulus of 130 GPa. The dimensions and the interphase and matrix properties of this fragment are the same as those of the baseline model as shown in **Table 3.1.1**. Perfect bond is assumed between the fiber and the interphase. For an applied load of 1.58% strain at the upper loading edge shown in **Figure 3.1.1**, the fiber axial and shear stress distributions from the finite element analysis are illustrated in **Figure 4.1.23**. A fifth-order polynomial is used to fit the fiber stress distribution as shown in **Figure 4.1.23a**. From the curve fitted polynomial, **equation (17)** is applied to obtain the interphase shear stress distribution and is shown in **Figure 4.1.23b**. Note that **equation (17)** does not invole stress-to-strain conversion. It is shown that the derived

shear stress curve from **equation (17)** does not agree with the direct result from finite element analysis. There is no shear plateau as it should be as a result of matrix plasticity.

The curve-fitting technique will also work poorly for the debonded cases in **Figure 4.1.13b**. Physically, the fiber axial stress distribution is made up of four different regions as discussed in the previous section. They are the friction stress transfer region, the constant shear transfer region (due to matrix plasticity), the decaying shear stress transfer region and the zero stress transfer region. Ideally four curves with proper polynomial orders should be used to describe the fiber strains in the above mentioned four different stress transfer sections. Then the data scatter will not play a part in defining the material behavior. The single-curve fitting technique cannot distinguish the difference between these physically dissimilar sections, especially at the presence of experimental data scatter.

4.2 In-Situ Micro Indentation Test

4.2.1 Fiber aspect ratio

It was found that the stress perturbation on the interface due to the applied load diminishes at about 36 fiber diameters away from the indented fiber end, as shown in **Figure 4.2.1** from a baseline model. Thus the fiber aspect ratio, l/d_f, has to be higher than 36, which can be easily achieved in the experiment, in order to eliminate the effects from the boundary constraints. For the three cases studied in this research, where l/d_f are 36.25, 61.25, and 111.25, the stress distributions are identical because either case has a fiber aspect ratio higher than the l/d_f=36 critical value.

4.2.2 Specimen Foundation

Similarly, the foundation has no effect on the stress field when the fiber aspect ratio is higher than the critical value. When the foundation varies from hard steel to soft epoxy, the stress distributions for the baseline model, which has a fiber aspect ratio l/d_f=61.25 and a fiber volume fraction V_f=0.36, are the same.

As the fiber volume fraction increases, the perturbed fiber length or the critical fiber length decreases. For composite with stiffer matrix, the perturbed fiber length also decreases. It is common laboratory practice to select the specimen length for the micro-indentation test to be between 5mm and 10mm for convenience, which translates into a

fiber aspect ratio of 625 to 1250 for fibers with 8 microns diameter. Thus the specimen aspect ratio and the sample supporting material have no effect on the indentation test results.

4.2.3 Fiber Volume Fraction Effect

Due to the non-uniformity of the composite materials, and the ambiguity of the fiber selection criteria, the local fiber volume fraction, V_f, for each indented fiber is different. The fiber volume fraction effect is evaluated for models with V_f=0.1, 0.15, 0.2, 0.3 and 0.5. In this evaluation, the fiber diameter remains constant for all fiber volume fraction variations; only the matrix thickness, t_m, varies. For models with a higher fiber volume fraction, the composite modulus is higher thus imposing larger constraints to the fiber and interphase for deformation which in turn results in higher interfacial and matrix shear stresses and strains. As the fiber volume fraction changes from 0.1 to 0.5, the variation of the interfacial shear stress is about 35%, **Figure 4.2.2**. If the interfacial shear strength is an invariant for fibers associated with various fiber volume fractions, the fiber associated with higher fiber volume fraction will fail under lower applied load due to its higher $\tau_{i\text{-}max}/\sigma_f$ ratio, where $\tau_{i\text{-}max}$ and σ_f are the maximum interfacial shear stress and the average fiber axial stress, respectively. Thus if the local fiber volume fraction for the indented fibers is not consistent, the debond load and hence the interfacial shear strength will vary. This is the main reason for the data scatter in the measured apparent interfacial shear strength with the micro-indentation test. As shown in **Figure 4.2.2**, the empirical equation (ITS) agrees well with the nonlinear finite element method (NLFEM) in deriving the maximum interfacial shear stress, $\tau_{i\text{-}max}$, when the fiber volume fraction is between 0.3 and 0.5. The best agreement can be obtained at V_f=0.36. The rest of the discussion in this report will be based on models with V_f=0.36 unless specified otherwise. The classical shear lag (shear lag) and modified shear lag (m. shear lag) equations do not compare well with NLFEM and ITS. The shear lag equation is accurate only at V_f=0.1.

The interfacial stress distributions along the interface in the axial direction near the fiber ends for a model with V_f=0.36 are shown in **Figure 4.2.3**. The interfacial axial (σ_{zz}), radial (σ_{rr}), hoop ($\sigma_{\theta\theta}$), and shear (τ_{rz}) stress distributions for models with

different fiber volume fractions are of similar shapes except that the shear stress is higher for the model with the higher fiber volume fraction. The radial stress is compressive with its maximum at about half a fiber diameter below the free surface and rapidly diminishes toward a zero value at about two fiber diameters below the free surface. Thus mode I fracture is unlikely. All the stresses except the hoop stress have the maximum value at some distance below the free surface and diminish to a zero value at the free surface. The maximum interfacial shear stress is located at about three quarters of a fiber diameter below the free surface while the maximum octahedral shear stress is at about 0.6 fiber diameters below the free surface. If maximum shear stress or maximum octahedral shear stress criterion is used, interface failure will be initiated at some distance below the free surface. However, because the maximum shear stress position is so close to the free surface that crack will propagate to the surface quickly and the load at which debonding is observed at the free surface can be taken as the debond load.

4.2.4 Interphase Property Effect

In a recent research by the authors [27], fiber tows were dipped into hexane solutions of the silsesquioxane terpolymer to form silsesquioxane coatings (preceramic polymer) typically 0.1 μm thick. The coatings were then pretreated by heating in N_2 to the selected temperatures. The amorphous polymeric coatings were shown to convert to amorphous silicon oxycarbide coatings on heating to temperatures above 600°C [27]. It was found that fiber-matrix adhesion increases with increasing coating modulus as a result of increasing heat treatment temperature of the preceramic polymer coated carbon fiber [27]. The increase in the fiber-matrix adhesion may be caused by the change in chemical composition and the surface energy at the interface. However, the coating property changes may also affect the interfacial shear strength measurement. Before the test data can be used to assess the fiber-matrix adhesion, the effect of coating or interphase properties on the interfacial shear stress fields and hence the apparent interfacial shear strength has to be identified. In this evaluation, the interphase property effect is evaluated by varying the interphase-to-matrix modulus ratio, E_i/E_m, between 0.7, 1.0, 1.5, 7.5, and 30. Because the volume fraction of the interphase, V_i, is so small, the effect of the interphase property changes on the overall composite properties and

hence the constraint to the indented fiber is insignificant. The stress and strain fields in the matrix do not experience much change as the interphase properties vary. However, the interfacial shear stress increases with increasing interphase properties. As the interphase modulus increases from E_i/E_m=1.0 to E_i/E_m=7.5, the interfacial shear stress increases about 10%, **Figure 4.2.4**. It is to be noted that for large E_i/E_m, the interfacial shear stress is no longer the dominant factor for failure initiation. For E_i/E_m=7.5, the interfacial hoop stress reaches the same magnitude as the interfacial shear stress. For E_i/E_m=30, the interfacial hoop stress and the axial compressive stress in the interphase layer are three and six times larger than the interfacial shear stress. Thus the interphase will fail under compressive or combined failure mode rather than interfacial shear. Therefore, the apparent interfacial shear strength is not accurate for samples with high interphase modulus.

The $\tau_{i\text{-}max}/\sigma_f$ ratio represents the efficiency of the development of the interfacial shear stress against the applied load. The debond load for the model with higher interphase modulus would be lower because of its higher $\tau_{i\text{-}max}/\sigma_f$ ratio. For classical shear lag and empirical ITS equations, the interphase modulus effect is ignored and thereby the $\tau_{i\text{-}max}/\sigma_f$ ratio is assumed to remain constant for various interphase modulus. The modified shear lag analysis by Tsai et. al. [50] included the interphase in the model; however, the interfacial shear stress is significantly over-predicted. Note that when the fiber volume fraction is outside the range of V_f=0.3~0.5, the empirical ITS equation becomes inaccurate. For model with V_f=0.15, the empirical ITS equation significantly under-predicts the interfacial shear stress.

4.2.5 Interphase Thickness Effect

In this evaluation, the interphase thickness, t_i, are $0.02d_f$, $0.05125d_f$, $0.125d_f$, $0.2d_f$ and $0.25d_f$. As shown in **Figure 4.2.5**, the interphase thickness only has marginal effect on the interfacial shear stress. For the baseline model, the fiber volume fraction is kept constant at V_f=0.36. The interphase modulus is 1.5 times the initial modulus of the matrix. As the interphase thickness increases, the volume fraction of the interphase increases but the effective composite modulus only increases marginally. The modified

shear lag equation predicts a more significant increase of the interfacial shear stress as compared to that of the NLFEM when the interphase thickness increases. However, the predicted magnitude is about 75% to 95% higher than that of the NLFEM.

4.2.6 Matrix Property Effect

When the matrix property varies, the interfacial shear stress and strain, the matrix shear stress and strain and the $\tau_{i\text{-}max}/\sigma_f$ ratio vary accordingly, **Figure 4.2.6**. In **Figure 4.2.6**, the normalized interfacial shear stress, $\tau_{i\text{-}max}/\sigma_f$, is plotted against the normalized matrix initial modulus. The complete stress-strain curves for the matrices are shown in **Figure 4.2.7**. When the matrix becomes more compliant, the shear strain increases in the matrix but decreases in the interphase. The $\tau_{i\text{-}max}/\sigma_f$ ratio changes significantly as the matrix modulus changes. Thus for composites with various matrix properties, the $\tau_{i\text{-}max}/\sigma_f$ ratio is far from constant. Errors will be introduced if the interfacial shear strength is derived based on the assumption that $\tau_{i\text{-}max}/\sigma_f$ ratio is constant for all matrix materials. The empirical ITS equation agrees very well with the nonlinear finite element method (NLFEM).

The experimental procedure of the microindentation test requires repetitive loading-unloading cycles to facilitate the observation of debond initiation under the optical microscope. This type of loading process will introduce residual stresses if the material is viscoelastic or elastic/plastic. In this study, the residual stresses of a loading-unloading cycle for models with non-linear elastic/plastic and viscoelastic matrix systems are evaluated. The final debond load is applied in order to simulate the worse case for residual stress development. The time-dependent shear creep compliance for Epon-828 matrix obtained from the Iosipescu shear test [51,52] is shown in **Figure 4.2.8**. The residual interfacial stresses are plotted at five minutes after beginning of loading (or one minute after the end of unloading). It was found that when the matrix is nonlinearly elastic/plastic, the residual radial, hoop, and axial stresses are tensile while the residual shear stress is compressive at regions within one fiber diameter below the free surface, **Figure 4.2.9a**. The maximum interfacial shear stress is at about 0.8 fiber diameter below the free surface. All the stresses approach zero values at free surface. Note that the stress

values for the first element below the free surface are considered inaccurate due to the numerical noise at free edge and are discarded. Because of the negative residual interfacial shear stress, the apparent interfacial shear strength will be higher than when this negative residual shear stress is absent. When the matrix is viscoelastic, the residual radial, hoop, and axial stresses at the interface are tensile while the residual shear stress is compressive, **Figure 4.2.9b**. However, the magnitude of the stresses are so low that its effect on the interfacial stress state due to the indented load is insignificant.

4.2.7 Fiber Diameter Effect

From experimental observation, the variation of the fiber diameters in the sample composite could be as large as ±25%, **Table 4.2.1**. The variation in the fiber diameters introduces local fiber volume fraction changes. To isolate the effect of fiber diameter on the interfacial shear stress, the fiber volume fraction is assumed to be constant, V_f=0.36, in this study. The debond load changes with the fiber diameter. As the fiber diameter increases from 8 microns to 10 microns (a 25% increase), the indenter load has to be increased from 5 grams to 8 grams to reach approximately the same magnitude of the interfacial shear stress. However, the $\tau_{i\text{-}max}/\sigma_f$ ratio was found to be insensitive to the change of fiber diameter and the load change, **Figure 4.2.10**. The empirical ITS equation, the shear lag equations and the NLFEM all predict the same trend. Thus a constant $\tau_{i\text{-}max}/\sigma_f$ ratio can be assumed for fibers with various diameter. However, only the empirical ITS equation agrees well with the NLFEM.

4.2.8 Thermal Residual Stress Effect

The microindentation samples are cured at 75°C and postcured at 125°C. The specimens are then tested at room temperature, 21°C. The difference between the postcure and room temperature is -104°C. Thus thermal residual stresses develop as a result of the mismatch among the moduli and thermal expansion coefficients of the constituents. However, because some relieving of residual stresses occur during cool down, a value of δT=-70°C is chosen for the analysis. The thermal residual stress due to thermal cool down alone is shown in **Figure 4.2.11**. It was found that the radial and shear stresses are compressive near the free surface while the axial and hoop stresses are tensile. The compressive radial thermal residual stress help to prevent mode I failure and

is beneficial. Because the thermal residual interfacial shear stress is of opposite sign to the interfacial shear stress introduced by the indentation load, the apparent interfacial shear strength will be higher since additional indentation load is needed to offset the thermal residual interfacial shear stress.

4.2.9 Usefulness of Load-Displacement Data

For microindentation test, the experimental data directly obtained is the load-displacement curve and the maximum load for debond initiation. The interfacial shear strength and hence the quality of the interface adhesion has to be assessed through a data reduction process. Significant effort can be saved if the load-displacement data can be used to obtain information about fiber-matrix interface adhesion. The purpose of this section is to investigate the usefulness of the load-displacement data in the interfacial shear strength measurement. The effect of five parameters (such as fiber volume fraction, matrix modulus, interphase modulus and thickness, and fiber diameter) on the indentation displacement were studied. Among these five parameters, only interphase modulus and thickness are related to interfacial properties. The displacements corresponding to a five grams force (approximately 0.05 Newton, or 995 MPa for a eight microns diameter fiber) are plotted against fiber volume fraction change, matrix modulus variation, interphase modulus and thickness changes, **Figure 4.2.12.**

It was found that the maximum indenter displacement corresponding to an applied load of five grams decreases as the fiber volume fraction increases, **Figure 4.2.12a.** Because the composite becomes stiffer with increasing fiber volume fraction, the resistance to the indenter displacement is higher. Similarly, when the matrix is stiffer the required indenter displacement is smaller for the same applied load, **Figure 4.2.12b.** However, indenter displacement is relative insensitive to the interphase modulus and thickness variation due to the small volume fraction of the interphase, **Figures 4.2.12c&d.** As the interphase modulus increases from $E_i/E_m=0.7$ to $E_i/E_m=30$, the change in the indenter displacement is only 1.5%, which is within the experimental errors. When the interphase thickness increases from $t_i/d_f=0.02$ to $t_i/d_f=0.25$, the change of the indenter displacement is 2.4%, also within experimental errors.

The variation of fiber diameter will causes variation of indenter displacement. As the fiber diameter increases from eight microns to ten microns (a 25% increase), the indenter load has to be increased from five grams to eight grams (a 60% increase) to reach approximately the same magnitude of fiber axial stress. The corresponding increase of the indenter displacement is 15%. Though the $\tau_{i\text{-}max}/\sigma_f$ ratio was found to be insensitive to the change of fiber diameter, the slope of the load-displacement curve (either F versus d_f, or F/d_f versus d_f) is not constant for the various fiber sizes. Thus the load-displacement data is more sensitive to the non-interphase related properties. Unlike the cyclic indentation test for ceramic composites, or the fiber pull-out test where a change of slope does occur when debond occurs, the load-displacement data of the micro-indentation test itself cannot be used to derive the interphase properties.

4.3 Single Fiber Micro Indentation Test

4.3.1 Interfacial Shear Stress Distribution

Similar to the single-fiber fragmentation specimen, the interfacial shear stress distribution for the micro-indentation specimen is highly non-uniform. When the indenter displacement is four microns, the maximum interfacial shear stress induced in the aluminum 2024/Epon 828 matrix composite is about 46 MPa. The mean interfacial shear stress from **equation (14)** is about 4.76 MPa (from integration of the interfacial shear stress distribution along the fiber length, the average interfacial shear stress is 4.49 MPa, **Figure 4.3.1a**). Therefore, this averaging technique will reduce the difference in interfacial shear strength with respect to interfacial properties change. However, similar to the single fiber fragmentation test, a qualitative comparison of interfacial shear properties can be easily obtained.

Similarly, the fiber axial stress distribution is not linear along the perturbed length, **Figure 4.3.1b**. The difference in the average interfacial shear stress obtained from equation 7 and from direct integration of the shear stress curve is partially due to the non-uniform interfacial shear stress and non-linear fiber axial stress distributions along the perturbed length. Though the derived average interfacial shear stress is not exact, the

dependence of the interfacial shear stress on the interfacial parameters is apparent as will be discussed in the following sections.

4.3.2 Effect of Matrix Modulus

Due to the nature of the test, there is no 'gage section' in the specimen where the stress or strain fields are uniform. Therefore, a genuine stress-strain relationship cannot be obtained. Instead, a mean interfacial shear stress is plotted against a normalized indenter displacement (Z_i/d_f). From the pseudo mean interfacial shear stress-strain (pseudo strain, Z_i/d_f) curve, the equivalent interfacial modulus can be estimated through the slope of the curve. Though Z_i/d_f is not a strain, it is used for convenience to represent a pseudo average strain (note that Z_i/L_p is not a strain either). In this section, the effect of matrix material behavior on the interfacial shear stress and the pseudo interfacial shear modulus is evaluated. Aluminum alloy fibers of 100 microns diameter are embedded in a standard Epon-828 14.5 phr of mPDA matrix (stiff matrix) and a fictitious more compliant matrix (compliant matrix) to form single-fiber composite. The indenter load-displacement data and the interfacial shear stress-pseudo strain data are plotted in **Figures 4.3.2&4.3.3**. For a given indenter displacement, the induced indenter load and mean interfacial shear stress are higher when the matrix is more stiff, **Figure 4.3.3**. As shown in **Table 4.3.1**, the pseudo interfacial shear modulus is small when the matrix is compliant. As the indenter displacement increases, the average interfacial shear stress increases to a peak value and then decreases, **Figure 4.3.3**. This non-linear shear stress-Z_i/d_f behavior is caused by the non-linearly plastic behavior of the aluminum alloy. A parallel study with linear aluminum alloy material properties does not show such a trend, **Figure 4.3.4**. After the aluminum alloy yields, further displacement loading does not introduce significant increase in resistance forces, **Figure 4.3.4a.** The decrease of mean interfacial shear stress after yielding of aluminum alloy can be easily seen from **equation (14)**.

Some interfacial parameters at the Z_i=4 microns and at the peak of shear stress-Z_i/d_f curve are shown in **Table 4.3.1**. The mean interfacial shear stress obtained from equation 7 (4.76 MPa) agrees well with that from direct integration (4.49 MPa) of the

mean interfacial shear stress-Z_i/d_f curve. Because the initial pseudo shear modulus is used, the pseudo shear moduli are the same for both linearly-elastic and linearly-elastic/non-linearly plastic aluminum alloy fiber/Epon 828 matrix single-fiber composites, **Tables 4.3.1 & 4.3.2**. When the fiber is linearly elastic, at Zi=4 microns, the normalized perturbed length is shorter and the stress transfer efficiency is higher (the induced mean interfacial shear stress is higher) compared to when the fiber is linearly elastic/non-linearly plastic. Therefore, it can be extended that as fiber becomes more stiff, the normalized perturbed length will be shorter and the shear stress transfer efficiency will be higher. From **Table 4.3.1**, it can be seen that the normalized perturbed length (L_p/d_f) decreases with increasing matrix modulus (24.16 for compliant matrix and 20.86 for stiff matrix) while the shear stress transfer efficiency (τ_m/σ_f) increases with increasing matrix modulus (10.3E-3 for compliant matrix and 11.98E-3 for stiff matrix). After the fiber yields, the induced interfacial shear stress does not have a one-to-one relationship with the indenter displacement; therefore, if debonding occurs after fiber yielding, the apparent interfacial shear strength cannot be regarded as true interfacial shear strength. Fiber yielding can be easily observed from the mean interfacial shear stress-Z_i/d_f curve though it is not obvious in the load-displacement data.

4.3.3 Effect of Fiber Size

When the fibers are fabricated, the fiber diameters are not always uniform. It is very common to find fibers with diameters of ±20% variation from the nominal fiber diameter. Therefore, it is desirable to assess the fiber size effect on the pseudo interfacial shear modulus and shear stresses. In this study, the pseudo interfacial shear modulus and shear stress field for single-fiber aluminum alloy fiber/Epon 828 matrix composite with fiber sizes of 75 and 100 microns are evaluated. Though the load-displacement curves are significantly affected by the fiber size, **Figure 4.3.2**, the pseudo interfacial shear modulus does not show a significant dependence on the fiber size, **Figure 4.3.3**. The mean interfacial shear stress derived from **equation (14)** is slightly higher than that from direct integration of the shear stress-Z_i/d_f curve. At the peak of the mean interfacial shear stress-Z_i/d_f curve, the induced mean interfacial shear stress is higher for the 75 microns fiber. However, the perturbed length as well as the shear stress transfer efficiency are the

same for 100 and 75 microns fibers, **Table 4.3.1**. This finding agrees well with the result of the in-situ micro indentation analysis that $\tau_{i\text{-}max}/\sigma_f$ ratio was insensitive to the change of fiber diameter in the in-situ composite, where σ_f is the applied fiber axial stress and $\tau_{i\text{-}max}$ is induced maximum interfacial shear stress in the in-situ composite. When the aluminum alloy is linearly elastic, a similar trend is observed, **Table 4.3.2**. At Z_i=4 μ, though the induced mean interfacial shear stress for the 75 microns fiber composite is much higher than that of the 100 microns fiber composite, the perturbed length (L_p/d_f), the shear stress transfer efficiency (τ_m/σ_f) and the pseudo shear modulus for these two different sized fiber composites are the same.

4.3.4 Application of Modified Kelly & Tyson Equation to In-situ Carbon Fiber Composite.

Though the Kelly & Tyson equation was modified originally to reduce the experimental data for the single-fiber micro-indentation test, it can be used to reduce the load-displacement data of in-situ composites of any fiber volume fraction. To evaluate the effectiveness of the application of modified Kelly & Tyson equation in reducing test data of in-situ composites, similar finite element analyses were performed. In addition, the effect of matrix stiffness and fiber size on the pseudo interfacial shear modulus were evaluated. The matrix stiffness effect is evaluated by embedding 8 micron carbon fibers in the standard Epon 828 14.5 phr of mPDA (stiff matrix) and a fictitious more compliant matrix (compliant matrix) with the material behaviors as shown in **Figure 3.3.3b**. The effect of fiber size is evaluated by embedding carbon fibers of eight and six microns in diameter in the stiff matrix. The load-displacement data for this in-situ carbon fiber composite with 36% fiber volume fraction are shown in **Figure 4.3.5**. The mean interfacial shear stress-Z_i/d_f curves are shown in **Figure 4.3.6**. Because the indenter is spherical in shape, the load-displacement curves are non-linear in the very beginning of the loading, and the slope increases with increasing load. The load-displacement curves become linear after 0.1 microns indenter displacement. A pseudo interfacial shear modulus can be calculated using the linear portion of the mean interfacial shear stress-Z_i/d_f curve. The interfacial shear stresses and pseudo interfacial shear moduli as well as

other interfacial parameter values at Z_i=0.5 microns for the carbon fiber/Epon 828 composites are shown in **Table 4.3.3**. In each case the mean interfacial shear stress obtained from direct integration of the shear stress-Z_i/d_f curves, **Figure 4.3.7**, at indenter displacement Z_i=0.5 microns agrees well with those from **equation (14)**. As the matrix becomes more stiff, the pseudo interfacial shear modulus ($\tau_m/(Z_i/r_f)$) and the shear stress transfer efficiency (τ_m/σ_f) increases. Because the shear stress transfer is more efficient, the perturbed length-to-fiber diameter ratio (L_p/d_f) decreases. However, as the fiber diameter changes from eight microns to six microns, the changes in pseudo interfacial shear modulus, shear stress transfer efficiency and normalized perturbed length are insignificant. Therefore, the interfacial shear modulus is a material property which depends on the material behavior of constituent materials, not on the size of the constituent materials. Note that the normalized perturbed length for the eight microns fiber/Epon 828 matrix (stiff) using the modified Kelly & Tyson equation is longer than that of the in-situ micro indentation test (L_p/d_f=36). In the study of in-situ micro indentation test, the perturbed length was defined as the length where the interfacial shear stresses are equal or greater than one percent of the peak interfacial shear stress while in this study no cut-off values are used.

For a single carbon fiber/Epon 828 matrix micro-indentation specimen with a fiber diameter of eight microns and a stiff matrix is indented with a indenter displacement Z_i=0.5 microns, the induced mean interfacial shear stress is 7.48 MPa, which is much lower than that of the in-situ carbon composite specimen (10.35 MPa). The normalized perturbed length (44.61) is longer than that of the in-situ composite (38.14). It indicates that fiber volume fraction plays a important role in the interfacial shear property. However, as the matrix becomes massive (very low fiber volume fraction), the effect of fiber volume fraction variation on the interfacial shear properties become insignificant.

4.3.5 Sensitivity of Displacement Data

The data reduction scheme for pseudo mean interfacial shear modulus requires accurate measurements of indenter load as well as indenter displacement at debonding. However, the current micro-indentation test apparatus does not generate accurate indenter

displacement because the loadcell and the displacement actuator are on the same side of the load frame, which introduces much higher apparent indenter displacement. In addition, the step motor and gearing used for displacement control are susceptible to temperature changes and gearing tolerance. Therefore, an ideal micro-indentation test apparatus has to be developed for accurate interfacial shear properties measurement. To the authors' knowledge, Kalinka et. al. [53] are re-designing the micro-indentation test apparatus with the loadcell and displacement actuator at the opposite ends of the load frame. In addition, the indenter displacement measurement will be more accurate if a servo-hydraulic system is used to replace the stepping motor and gearing system.

4.4 The Dynamic Mechanical Analysis.

4.4.1 Dynamic and Viscoelastic Properties of the Epoxy

The Epoxy Matrix sample (without the reinforcing fiber) and the wire sample were tested first. The resulting information about the mechanical and viscoelastic properties from the DMA temperature sweep can be seen in **Figures 4.4.1** and **4.4.2. Figure 4.4.1** shows the tan Delta curve of the mPDA and T-403 cured epoxies and the Aluminum Alloy 6061 250 micron wire. The Tg point temperature of the two epoxies can easily be distinguished by the sharp peak in the tan Delta curve. The Tg point of the Epon 828/mPDA epoxy is at 179.8 °C, more than 80 °C higher than the Tg point of the Epon 828/T-403 Jeffamine epoxy at 96.9 °C. The Aluminum wire does not show any glass transition or viscoelastic behavior as expected. In the following composite and DMA sample tests we can assume that the wire does not have any direct influence on the loss modulus (E") and tan Delta curve.

In **Figure 4.4.2** the storage modulus (E') curve is shown, obtained from the DMA test. As expected, the storage modulus of the wire is more than a decade higher than the modulus of the epoxies. The glass transitions of both epoxies are again clear to distinguishable and about 80 °C apart from each other. To identify peaks in the tan Delta and E' curve more clearly, the derivative of these curves are plotted in **Figure 4.4.3** and **Figure 4.4.4**.

4.4.2 Effect of the Curing Cycle

The epoxy sample has to be fully cured in order to make a fully reproducible test possible. Early tests have shown, that under-cured samples cure further during the temperature sweep and the Tg point moves up from the first test to the following tests with the same sample. In **Figure 4.4.5** a DMA sample with a Epon/mPDA matrix, cured with the standard cycle of two hours at 75 °C and two hours of 125 °C, is tested four times through the temperature range from 100 degrees to 250 °C. The glass transition temperature shifts from 185 °C during the first test to 205 °C in the third test. The difference in the Tg is proportional to its degree of cure. That is, the sample was undergoing additional curing during the DMA test itself. **Figure 4.4.6** shows the first derivatives of the tan Delta curves seen in **Figure 4.4.5**.

Postcuring the samples in an inert gas oven at 175 °C for two hours resulted in full cure and the Tg doublet was not detected by DMA.

4.4.3 Effect of Reinforced Sample and the Sample Shape

Results from DMA measurements of the different kinds of samples are presented in **Figures 4.4.7** and **4.4.8**. There is a shift observed in the glass transition temperatures between the different sample types with the same epoxy matrix. **Figure 4.4.7** shows the tan Delta curves of the samples with Epon/mPDA matrix and the corresponding derivative curve in **Figure 4.4.9**. The tan Delta curve of the composite sample reveals two peaks at a higher glass transition temperature than the pure epoxy sample with the standard heating rate of 5 °C per minute. Additional tests at different heating ramp rates of 1 and 2 °C/min revealed an artifact due to the composite sample shape and to heat transfer within the sample (**Figure 4.4.8** and **Figure 4.4.10**). This results from the fact, that the amount of epoxy is less than in the composite sample and the heat can transfer more quickly through the fibers. All further tests with the DMA sample were continued with the ramp rate of 5 °C per minute. This artifact is similar to the ones found by Reed [54] and Thomason [55].

The tan Delta curve of the DMA sample has a glass transition temperature even higher than the composite and matrix sample. The Tg for the bulk epoxy sample is 180°C. In the DMA sample configuration a single peak is detected but at a higher Tg of

205 °C. This shift in the Tg point is a result of the reinforcement of the matrix. The DMA sample has the same matrix composition as the epoxy and composite sample and volume percentile does not influence the glass transition temperature. The aluminum also does not influence the curing of the matrix. The shift in the glass transition is not caused by any test parameter and has to be a result of the load transfer from matrix to the fiber in the interphase.

The effect of the reinforcing fiber on the storage modulus is as high as expected. The storage modulus of the reinforced composite sample can be mathematically calculated by the volumetric amount of fiber in the sample.

Figures 4.4.11 shows the tan Delta curves over the temperature of the same four sample shapes with Epon 828 / T-403 Jeffamine matrix. The results obtained with these samples are similar to the ones obtained with Epon 828 / mPDA matrix. The difference in the Tg is as significant, but in lower temperature range. Again the composite sample tan Delta curve shows a double peak due to the heat transfer within the sample. The tan Delta peak of the DMA sample and the higher temperature peak of the composite sample doublet is at the same temperature of 118°C, 20°C above the Tg of the matrix sample. The load transfer in the Epon 828 / Jeffamine composite sample has to be similar to the load transfer in the Epon 828 / Jeffamine DMA Sample. In **Figure 4.4.12**, the derivatives of the tan Delta curves are plotted.

Variation of the fiber diameter showed no significant change in the glass transition temperature of Epon/mPDA as seen in **Figure 4.4.13**. A 250 micron diameter wire, a 125micron diameter wire and a 670micron glass fiber have been used in a DMA Sample with no significant change in the Tg point. The tan Delta peak of the glass fiber reinforced DMA sample is higher, because of the much greater interface surface and the weaker bonding between glass-fiber and epoxy matrix. This result proves that the amount of material does not have an influence on the glass transition temperature. The modulus of the three samples differs as expected.

4.4.4 Results from the Coated Fiber-Reinforced Composites

The temperature scan from a DMA sample with an Epon/Jeffamine coated Aluminum alloy 6061 250 micron fiber and a Epon/mPDA matrix is shown in **Figure**

4.4.14. In addition to the peak in the tan Delta and loss modulus curve caused by the glass transition of the Epon/mPDA matrix as seen in **Figure 4.4.7**, there is a smaller second peak at 125 °C detected on both curves. This peak can only be caused by the glass transition of the Epon/Jeffamine coating material of the fiber. The Tg temperature of 125 °C is just slightly higher than the Tg temperature of 117 °C detected on the DMA samples with Epon/Jeffamine matrix.

The coating on this 250 micron diameter fiber was only 2 microns or 3 % by volume of the fiber. Even though the amount of coating material is very small compared to the amount of the surrounding Epon/mPDA matrix (0.03% by volume) the loss modulus peak for the coating is about a third of the height of the matrix peak on the log modulus scale. So very small coatings can be detected on a large fiber. To detect small peaks with greater sensitivity, the first derivative as seen in **Figure 4.4.15** can provide more sensitive information. In **Figure 4.4.16** the first derivative of the storage modulus is plotted.

It is also noted that there is a slight drop in the storage modulus at 125 °C. An interphase with a glass transition point lower than the matrix's can weaken the composite's mechanical properties long before the glass transition temperature of the matrix is reached.

Effect of the coating thickness. After tests with a two micron coating, further tests were conducted with thicker coatings. In **Figure 4.4.17** a comparison is given between two DMA samples with different Epon/Jeffamine coating thickness in the Epon 828 / mPDA matrix. The height of the tan Delta and E" peaks at about 125 °C seems to be proportional to the amount of coating material. The Dynamic Mechanical Analysis could be a tool to characterize not only the viscoelastic properties of the coating but also the thickness of the coating on the fiber. The sample with the 12 micron coating shows a minimal shift in the glass transition to a lower temperature.

In the **Figure 4.4.18** and **Figure 4.4.19** the Environmental Scanning Electronic Microscope pictures of the coated wires are presented. The thickness of the thin coating (**Figure 4.4.18**) is very constant around the fiber circumference while the thicker coating varies from 10 to 20 microns with an average of 12 microns (**Figure 4.4.18**). A longer

curing period on the motor bench would be advised to further reduce the distortion due to the gravitational effect on the coating during the curing process.

In **Figure 4.4.20** and **Figure 4.4.21** the first derivative of the tan Delta curve and the loss modulus are plotted. **Figure 4.4.22** shows the storage modulus curves of three different coating thicknesses. The difference in modulus might be an artifact due to instrumentation parameters. However, the drop in the modulus is certainly due to the viscoelastic property of the interphase. **Figure 4.4.23** shows the first derivative of the storage modulus as seen in **Figure 4.4.22**.

Effect of the heating rate. The heating ramp rate has a very important influence on the results. An increase in the heating rate will shift the Tg points to a higher temperature as already seen in **Figure 4.4.8**. This effect is due to the increasing thermal lag between the inside of the sample, the outside of the sample and the thermocouple, which is mounted closer to the furnace. This effect is more apparent at higher temperature and faster ramp rate. The influence of the heating rate also depends on the mount and size of the sample. In the tensile deformation measurement mode the sample is equidistant to the surrounding furnace. At a heating rate of 5 °C/min and below Tg, no artifacts in the form of a heating rate dependent second peak as described by Thomason [55] were found on the DMA Samples. As mentioned above, the composite samples were showing artifacts due to the heating ramp rate because of lag in thermal equilibrium in the higher matrix volume of the sample.

In **Figure 4.4.24** two tests of coated fiber DMA samples performed with heating ramp rates of 2 and 5 °C per minute are compared. The second peak at lower temperature due to the coating is clearly not an artifact. There is a clear shift in the whole curve, including both peaks, of 16 °C. Slower ramp rates do not have an influence on the form or the height of the tan Delta peaks on DMA samples as seen in **Figure 4.4.25**. The first derivative of the tan Delta curve is shown in **Figure 4.4.26**.

Effect of the Frequency. The frequency with which the dynamic stress is conducted has a significant influence on the glass transition temperature and the modulus. A frequency sweep is shown in **Figure 4.4.27**. (loss modulus curve) and **Figure 4.4.28** (tan Delta curve). Tests have been conducted with 0.1Hz, 1Hz, 10 Hz, 20 Hz and 100 Hz.

Frequencies higher than 50 Hz and lower than 1 Hz do not give any constant reading with the stiffness of the samples used. A frequency of 1 Hz has proven to give the most stable and repeatable reading during the tests with the chosen sample shape. With increasing frequency, there is a slight shift in the glass transition to a higher temperature, noticeable in both, the tan Delta and the loss modulus curve. The frequency does not have a notable influence on the sensitivity to detect a coating. However, at a frequency below 1 Hz the number of data points decreases as seen in **Table 4.4.1** resulting in lower quality data.

Effect of the Static Force. In the tensile deformation mode, the DMTA applies a static force to the sample in order to prevent buckling. Early experiments with Aluminum wire of a lesser diameter than 250 microns and lesser tensile strength than Aluminum Alloy 6061 required only a very small dynamic and static force. The instrument is marketed to be capable of forces as low as 0.01 Newton, but the regulation of the static force in the first moment of application is poor in this very low range, so that weaker and finer wires tended to break at the beginning of the test. In the temperature range up to 100 °C the sample is stiff and the loss modulus reading is not as stable as at higher temperatures. A static force of 3.5 Newton (350gramms) was found to bring good results in forms of stable loss modulus though.

Effect of the Free Fiber length. The free fiber length has been changed between 1mm, 2mm and 5mm. There is no change in the E" curve and no change in the tan Delta curve. The E' modulus decreases slightly with greater free fiber length. This effect can be explained with the higher stiffness of the sample with more embedded fiber length. The 1mm and 2mm free fiber length might cause double hump artifacts because of the poor heat transfer to the fiber.

Results of the Stress/Strain Experiment. A DMA Sample was tested in the stress/strain deformation measurement mode with the maximum available stress. The stress/strain or force/displacement curve is shown in **Figure 4.4.29**. The test was conducted at a temperature of 120 °C, below the glass transition temperature of the coating material as well as the matrix material. The test has been repeated with the same DMA Sample, resulting in an identical linear curve. The repeatability proves that the fiber does not debond from the matrix during the test when the maximum force of 15 Newton

is applied. The fiber is too large in diameter and the adhesion is too strong to initiate pull-out. The advantage of this pull out test with the DMA would be the isothermal testing in the temperature range of -100 degrees to +500 °C. A smaller fiber diameter has to be chosen to gain adhesion information resulting from this experiment.

In order to produce the peak to peak strain of 10 microns in the tensile deformation measurement mode, a force of 5 Newton is necessary. The maximum force applied to the DMA Sample in the tensile mode does not exceed 5 Newton, so debonding will not take place in the cyclic tension mode.

5. CONCLUSIONS

5.1 Single Fiber Fragmentation Test

A non-linear finite element analysis has been used to study the mechanics of the single fiber fragmentation test. It was shown that the stress transfer efficiency is different for fragments which are created at different matrix strains. Interphase shear failure precedes interphase tensile fracture because of the shear stress singularity at the free edge. The shear stress singularity at the free edge is responsible for the interface debonding. Because of debonding, there will be a statistical distribution of fiber critical lengths. Although interphase property gradients affect the average interphase property, in terms of micro-mechanical modeling, the interphase can be assumed to be uniform in properties. Thermal residual stresses are found to reduce the stress transfer efficiency. The interphase is more likely to fail under tensile fracture when thermal residual stresses are present. It has been shown that fiber/interphase debonding reduces the interphase stress transfer efficiency and debonding will cause interphase fracture in the debonded region. The stress transfer efficiency does not increase monotonically with increasing interphase stiffness. In addition, increasing the interphase stiffness raises the likelihood of interphase fracture. The increase of the interphase thickness has a far larger impact on the interphase shear stress than the fiber axial stress for both compliant and brittle interphases. The fiber with lower tensile properties should have a shorter critical length if it undergoes brittle failure.

5.2 In-situ Micro Indentation Test

A nonlinear finite element analysis was applied to evaluate the effects of sample preparation procedure and constituent material properties on the fiber-matrix interfacial shear stress distribution determined by the microindentation test. It was found that for a carbon fiber/epoxy composite the stress perturbation caused by the indentation load diminishes at approximately 36 fiber diameters below the free surface. The stress fields for samples with different fiber aspect ratio and supporting materials are identical when the fiber aspect ratio is larger than the critical value. The perturbed stress fields of the indented fibers are significantly affected by the local fiber volume fraction distribution. Due to the non-homogeneity of the composite materials, the variation of local fiber volume fraction inevitably causes some data scatter of the micro-indentation test results. The empirical ITS equation agrees well with the nonlinear finite element method in deriving the interfacial shear stress when the fiber volume fraction is between 0.3 and 0.5. To obtain accurate and consistent measurement of the interfacial shear strength, a more stringent fiber selection criteria or a data correction scheme has to be applied. Currently a data correction scheme to account for the variation of local fiber volume fraction is under study by the authors. The classical and modified shear lag equations were found to be inaccurate for interfacial shear stress prediction. The inaccuracy of the shear lag equations is due to its over-simplified one-dimensional modeling and assumptions. The interfacial shear stress is sensitive to the interphase modulus and is affected by the interphase thickness only marginally. Similar to the single fiber fragmentation test, the interfacial shear stress distribution is significantly affected by the matrix materials. The matrix's nonlinearly elastic/plastic behavior causes residual stresses due to the loading-unloading test procedure associated with the indentation test. In addition, the presence of interfacial thermal residual shear stress introduces a higher apparent interfacial shear strength. For fibers with different diameter, the debond load will be different, but the interfacial shear stress-to-fiber axial stress ratio, $\tau_{i\text{-}max}/\sigma_f$, is unchanged. The load-displacement data from the microindentation test by itself cannot be used to extract interphase properties for polymer composites.

5.3 Single Fiber Micro Indentation Test

A single-fiber micro-indentation test was proposed in place of the existing micro-indentation test for high fiber volume fraction composites to reduce the experimental data scattering due to local fiber volume fraction variation in the in-situ composite. The Kelly & Tyson equation originally used in the single-fiber fragmentation test was modified and combined with the fiber strain energy equation to obtain an equation for mean/average interfacial shear stress and pseudo mean interfacial shear modulus. Finite element analyses were performed to evaluate the effectiveness of the modified Kelly & Tyson equation in reducing the experimental data of micro-indentation test. Good agreement between the results from modified Kelly & Tyson equation and the finite element analyses were found. Both finite element analyses and the modified Kelly & Tyson equation were used to evaluate the effect of matrix compliance and fiber size on the interfacial shear stress and pseudo interfacial shear modulus. It was found that the pseudo interfacial shear modulus increases with increasing matrix modulus. The interfacial shear properties were found to be independent of the fiber size.

5.4 Dynamic Mechanical Analysis

The utility of the Dynamic Mechanical Analysis as a characterization tool for interphase properties of fiber reinforced composite materials has been investigated. The sample shape has been found to be very important. A single fiber reinforced composite sample shape for the tensile deformation measurement mode has been designed. It produces load transfer from the matrix to the fiber and back. The heat transfer within the sample is fast enough not to produce any artifacts due to the heating ramp rate.

The influence of test parameters has been evaluated and discussed and ideal test parameters have been found to give a clear reading of the loss and storage modulus as well as the exact glass transition temperature. These results are proven to be reproducible. Composite test samples with a fiber reinforcement have a higher glass transition temperature than the matrix material. Depending on the load transfer from matrix to the reinforcing fiber in the interphase of a composite, the glass transition temperature rises up to 20 °C above the Tg of the matrix material. The sensitivity of the present DMA has proven to be exceptionally high.

A deliberately built-in interphase in the form of a thin epoxy coating with different mechanical properties than the matrix was applied to the fiber of a reinforced composite material DMA sample. This interphase was detected with the Dynamic Mechanical Analyzer in the tension deformation measurement mode. The height of the loss modulus curve obtained from the DMA reading is proportional to the coating thickness of the fiber exactly measured in the Environmental Scanning Electron Microscope.

The viscoelastic response of an interphase with a thickness of only 3% by volume of the fiber can be detected and the interphase influence on the storage modulus of the composite can be quantified with a Dynamic Mechanical Analyzer. The DMA can be used as a tool for interphase detection and characterization.

The built-in interphase was detected with the DMA on the aluminum/epoxy composite. The aluminum wire is fairly large compared with carbon fibers. The samples have to be downsized for testing of more common carbon fiber/epoxy composite materials and fiber tows should be used instead of single fibers. A tow of 2500 fibers with a diameter of 5 microns and a 0.037 micron coating would be equal in volume to the tested 250 micron Al wire with a 2 micron coating.

The shift in the glass transition point from a pure matrix sample to a composite sample has to be investigated and explained. A test where the sample is cooled down with the same ramp rate as the heating ramp rate could be conducted for this matter as well as tests with different materials.

6.0 LIST OF ALL PUBLICATIONS AND TECHNICAL REPORTS

H. Ho and L. T. Drzal, *"Evaluation of Interfacial Mechanical Properties of Fiber Reinforced Composites Using the Microindentation Method"*, **Composites, Part A,** 27A, pp. 967-971 (1996).

H. Ho and L. T. Drzal, *"Characterization of Interphase Properties Using the Single Fiber Microindentation Method"*, *submitted to* **Composite Science and Technology** (1997).

M. Alt, *"Dynamic Mechanical Analysis as a Tool for Interphase Characterization"*, Studentarbeit *submitted to* the University of Aachen and Michigan State University (1997).

7.0 LIST OF ALL PARTICIPATING SCIENTIFIC PERSONNEL

Professor Lawrence T. Drzal, Departments of Chemical Engineering and Materials Science and Mechanics, Composite Materials and Structures Center, Michigan State University

Dr. Henjen Ho, Composite Materials and Structures Center, Michigan State University

Matthias Alt, studentarbeit exchange student, University of Aachen, Aachen, Germany.

8.0 REPORT OF INVENTIONS

None

Table 3.1.1. Material property table. (use ITS, SFFT2 papers, including CTE, steel, Kevlar)

	carbon fiber	carbon interphase	Kevlar fiber	Kevlar interphase	Epon-828	steel
E_1 (GPa)	241	4.38	128	4.4	3.0*	200
E_2 (GPa)	21		6.9			
G_{12} (GPa)	28		9.3			
G_{23} (GPa)	8.3		2.6			
ν_{12}	0.25	0.30	0.33	0.34	0.35	0.33
α_1 (10^{-6}°C^{-1})	-0.11	68			68	
α_2 (10^{-6}°C^{-1})	8.5					

* initial modulus

Table 3.2.1. Typical test data for microindentation experiments.

glass/epoxy (l/d_f=100)	fiber diameter (micron)	t_m* (micron)	indenter disp. (micron)	debond load (gram)
fiber #1	6.95	3.4	1.32	5.75
fiber #2	7.65	3.1	1.60	8.27
fiber #3	6.00	2.0	1.08	4.21
fiber #4	7.20	3.8	1.20	6.79
fiber #5	6.00	4.3	1.00	4.44
fiber #6	5.75	2.4	1.12	4.13
fiber #7	7.90	5.5	1.52	8.21
fiber #8	6.60	2.4	1.08	4.53
fiber #9	6.45	2.0	0.92	3.78
fiber #10	6.60	2.4	1.20	4.37
fiber #11	7.40	2.4	1.24	6.82
fiber #12	7.90	2.4	2.00	7.70
fiber #13	7.90	2.4	1.24	7.25
fiber #14	6.70	2.0	1.52	5.54
fiber #15	6.70	2.4	1.12	5.25
average	6.91	2.9	1.28	5.80

* t_m is half the distance between the indented fiber and the nearest neighbor fiber.

Table 3.4.1. Mechanical properties of aluminum alloys.

alluminum alloy	tensile strength (MPa)	shear strength (MPa)	fatigue strength (MPa)	yield strength (MPa)
pure Al (1060)	69	48	21	28
Al 6061	125	83	62	55
Al 2024	185	125	90	76

Table 4.3.1. Average interfacial shear stress (MPa), pseudo interfacial shear modulus and other interfacial properties for aluminum alloy fiber/Epon 828 matrix single-fiber composite. Aluminum alloy is linearly elastic/non-linearly plastic.

	compliant matrix, d_f=100 μ	stiff matrix, d_f=100 μ	stiff matrix, d_f=75 μ
at the peak between Z_i=0 and Z_i=4μ			
τ_m from curve integration	4.14	4.62	4.86
τ_m from equation 7	4.44	4.95	5.21
corresponding σ_f	429.1	413.0	437.0
L_p/d_f	24.16	20.86	20.97
τ_m/σ_f	10.35E-3	11.98E-3	11.92E-3
at Z_i = 4 μ			
τ_m from curve integration	4.04	4.49	4.14
τ_m from equation 7	4.34	4.76	4.43
corresponding σ_f	450.8	471.8	525.4
L_p/d_f	25.97	24.78	29.65
τ_m/σ_f	9.63E-3	10.09E-3	8.43E-3
pseudo shear modulus ($\tau_m/(Z_i/r_f)$)	83.7	103.1	108.8

Table 4.3.2. Average interfacial shear stress (MPa), pseudo interfacial shear modulus and other interfacial properties for aluminum alloy fiber/Epon 828 matrix single-fiber composite. Aluminum alloy is linearly elastic.

at $Z_i = 4\ \mu$	compliant matrix, d_f=100 μ	stiff matrix, d_f=100 μ	stiff matrix, d_f=75 μ
τ_m from curve integration	6.10	7.60	10.47
τ_m from equation 7	6.57	8.16	11.18
corresponding σ_f	554.2	617.5	835.0
L_p/d_f	21.09	18.92	18.67
τ_m/σ_f	11.8E-3	13.2E-3	13.4E-3
pseudo shear modulus ($\tau_m/(Z_i/r_f)$)	83.8	103.2	108.8

Table 4.3.3. Average interfacial shear stress (MPa), pseudo interfacial shear modulus and other interfacial properties for carbon fiber/Epon 828 matrix in-situ composite. The fiber volume fraction is 36%.

at $Z_i = 0.5\ \mu$	compliant matrix, d_f=8 μ	stiff matrix, d_f=8 μ	stiff matrix, d_f=6 μ
τ_m from curve integration	7.82	10.22	13.44
τ_m from equation 7	7.93	10.35	13.59
corresponding σ_f (MPa)	1382	1580	2089
L_p/d_f	43.59	38.14	38.44
τ_m/σ_f	5.74 E-3	6.55 E-3	6.51 E-3
pseudo shear modulus ($\tau_m/(Z_i/r_f)$)	84.08	97.83	97.06

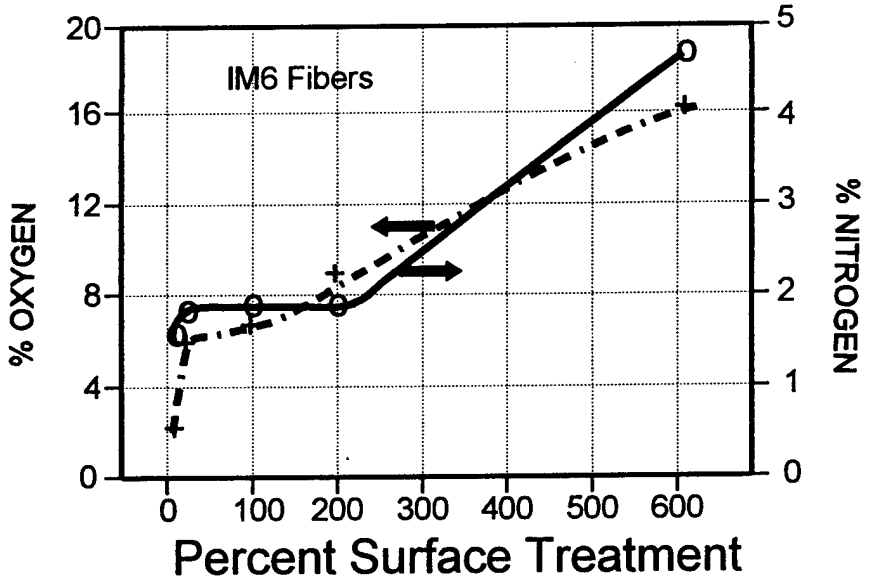

Figure 1.3.1. Surface Oxygen and Nitrogen Concentration Changes with Surface Treatment for IM6 Fibers measured by XPS.

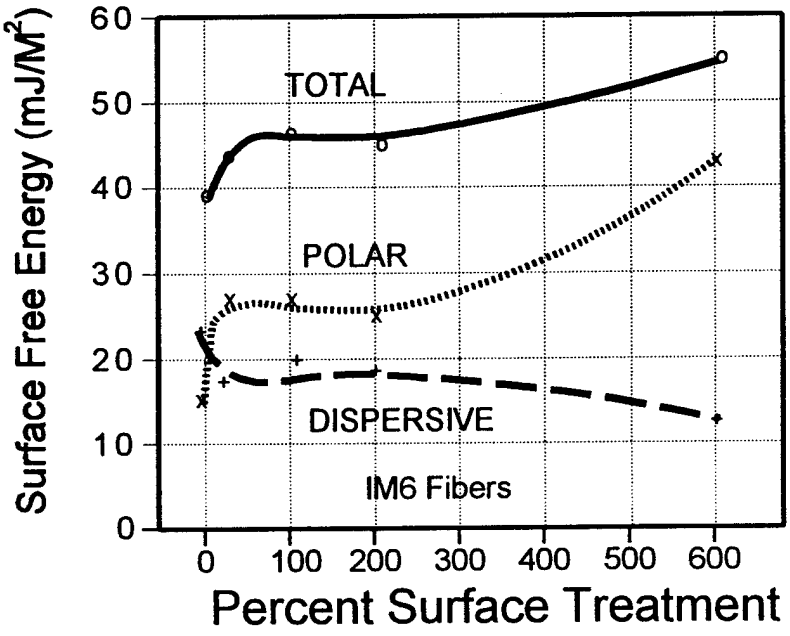

Figure 1.3.2. Polar, Dispersive and Total Surface Free Energy of IM6 Carbon Fibers After Increasing Surface Treatments.

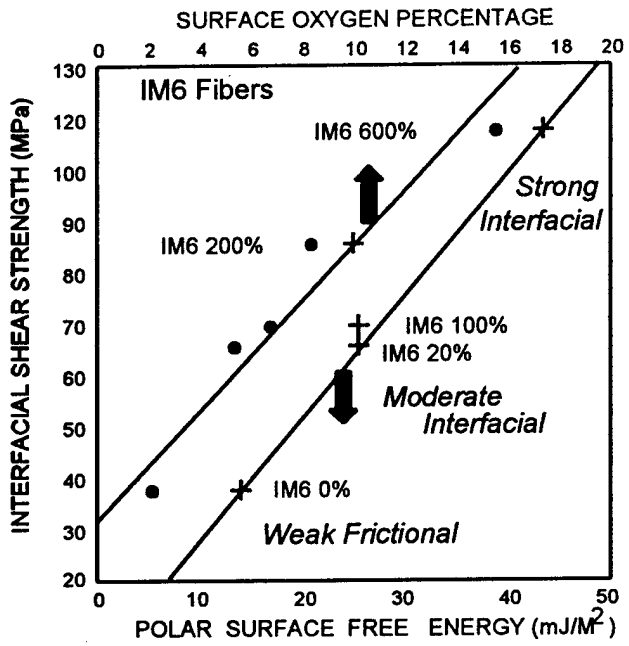

Figure 1.3.3. Interfacial Shear Strength of IM6 Carbon Fibers to an Epoxy Matrix as a Function of Fiber Polar Surface Free Energy and Surface Oxygen Concentration.

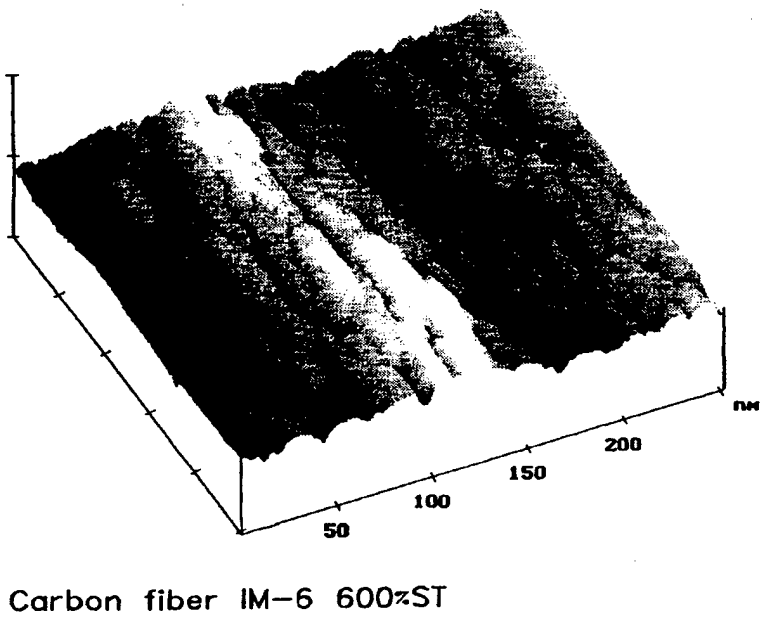

Figure 1.3.4. Scanning Tunneling Microscope image of an IM6-600% surface treated carbon fiber.

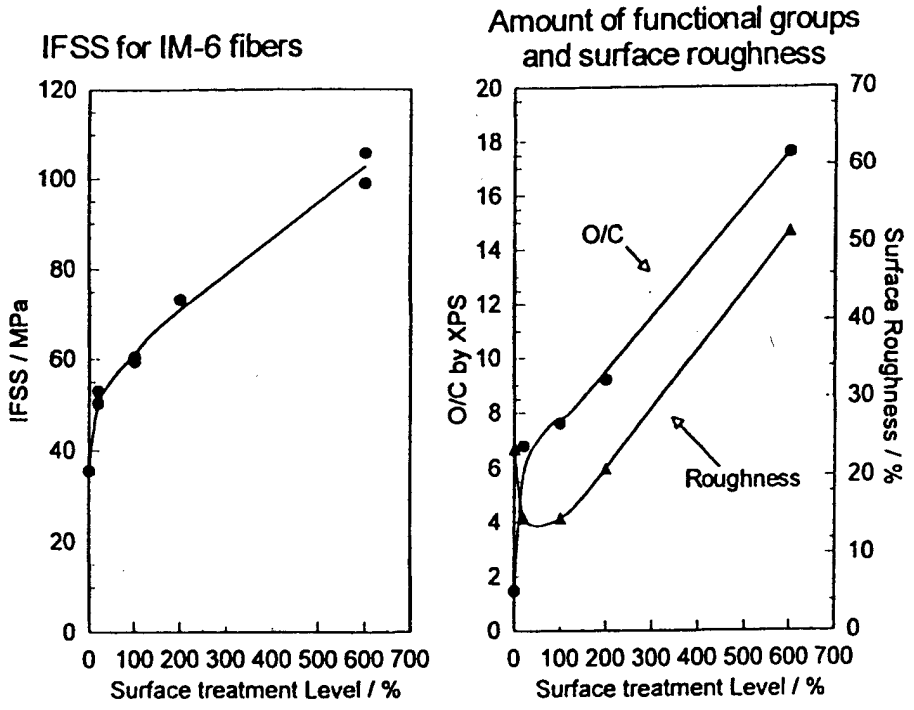

Figure 1.3.5. Change in surface roughness and surface area with surface chemistry and adhesion as a function of surface treatment for IM6 fibers in an epoxy matrix.

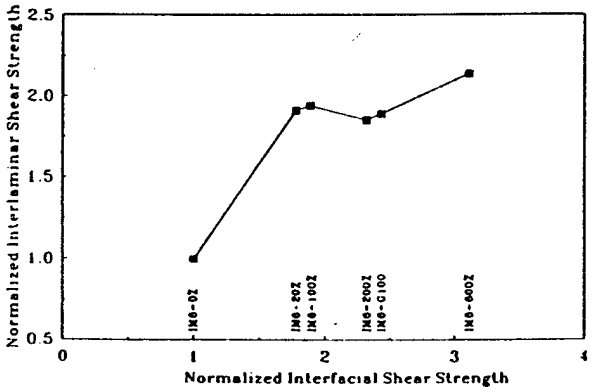

Figure 1.4.1. Normalized interlaminar shear strength versus normalized interfacial shear strength of IM6 carbon fiber/epoxy composites.

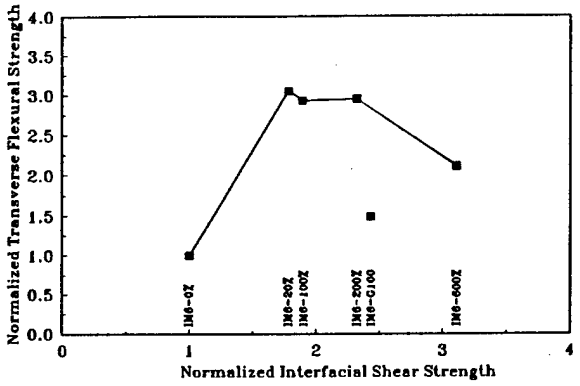

Figure 1.4.2. Normalized transverse flexural strength versus normalized interfacial shear strength of IM6 carbon fiber/epoxy composites.

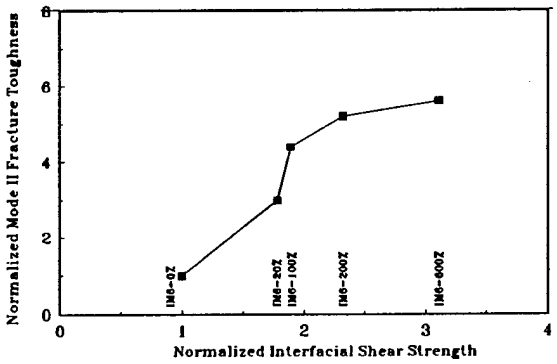

Figure 1.4.3. Normalized Mode II fracture toughness versus normalized interfacial shear strength for IM6 carbon fiber/epoxy composites.

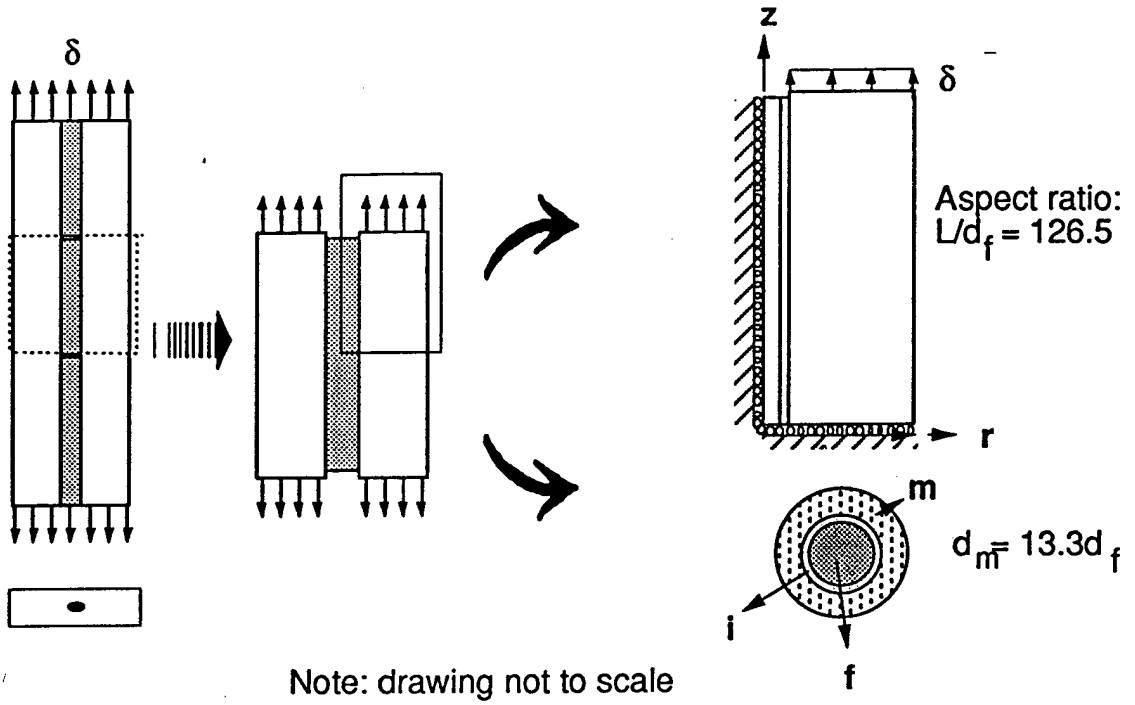

Figure 3.1.1. Finite element model of single fiber fragmentation test.

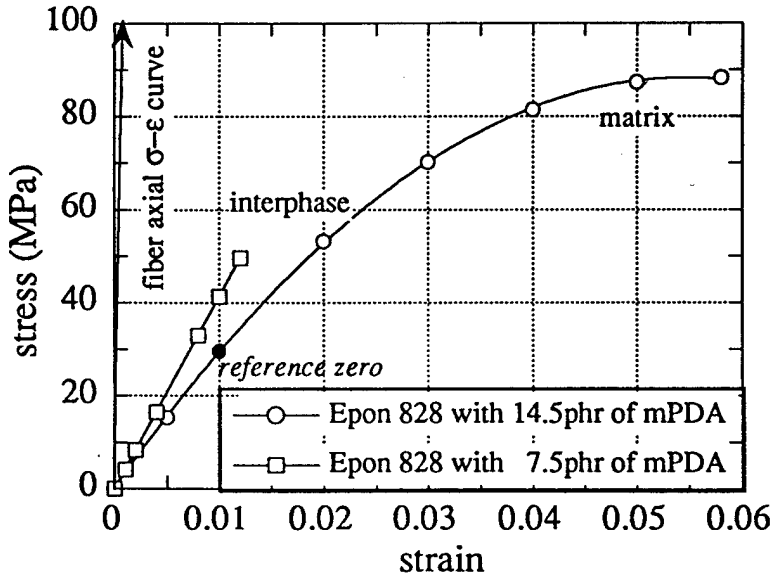

Figure 3.1.2. Stress-strain curve of the constituent materials for single fiber fragmentation test.

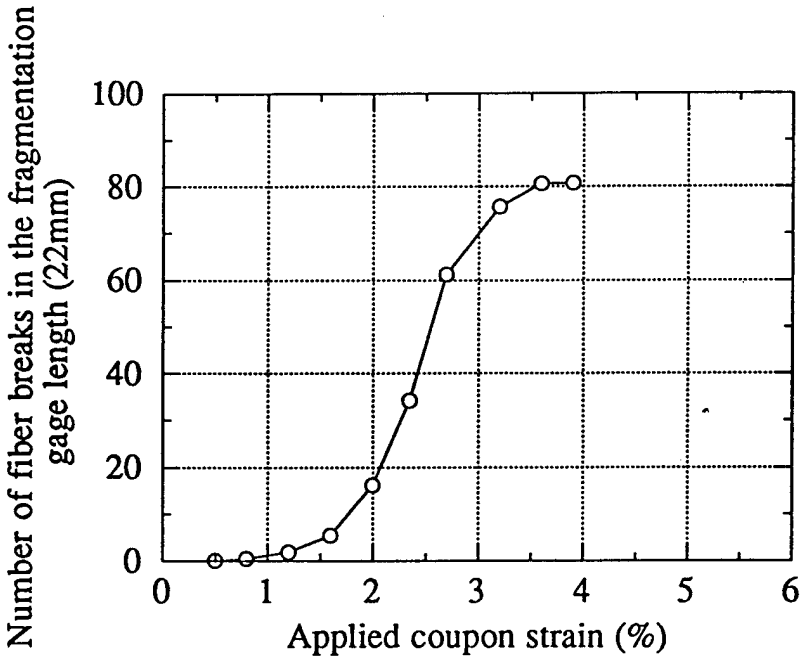

Figure 3.1.3. Number of fiber fractures vs. applied coupon strain.

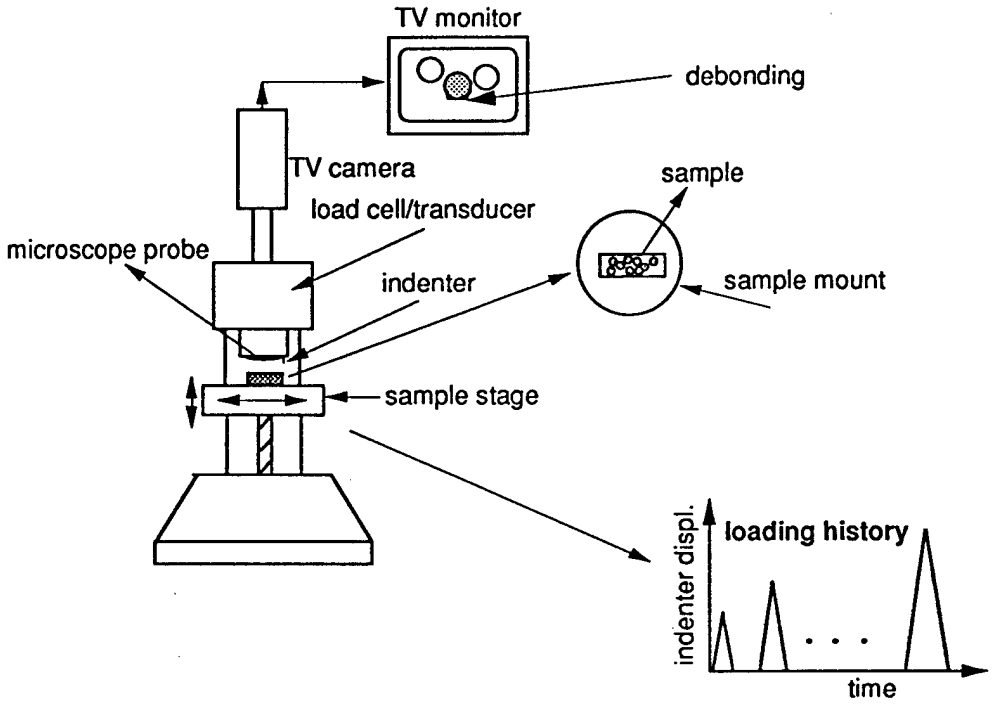

Figure 3.2.1. Schematic diagram of microindentation test apparatus.

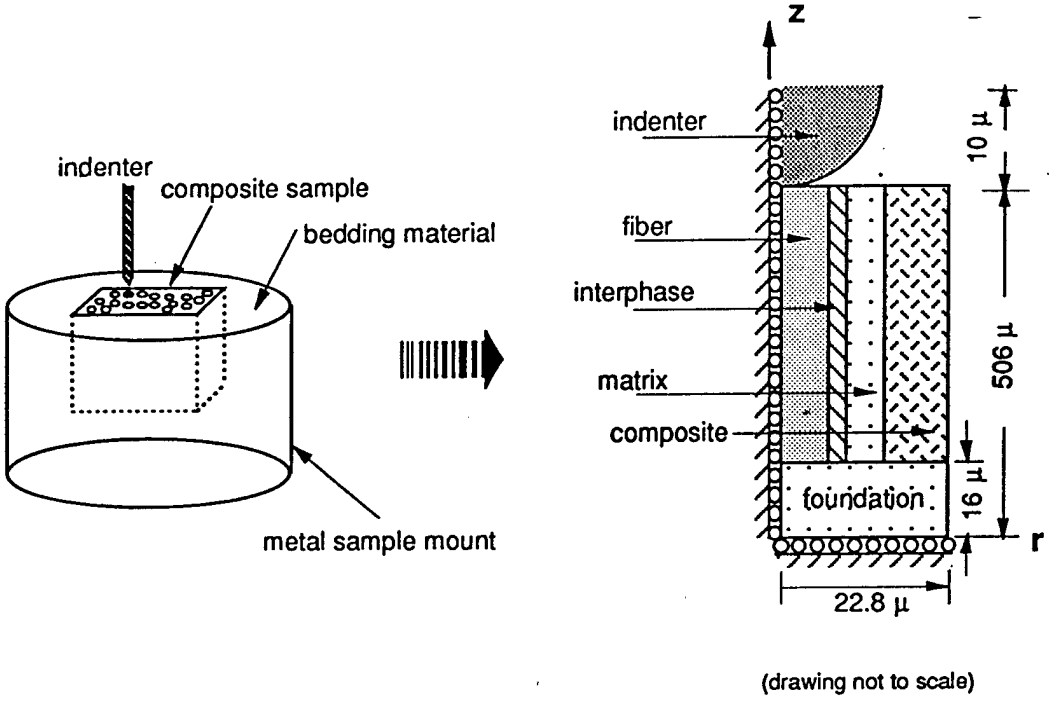

Figure 3.2.2. Finite element model of the micro-indentation test apparatus.

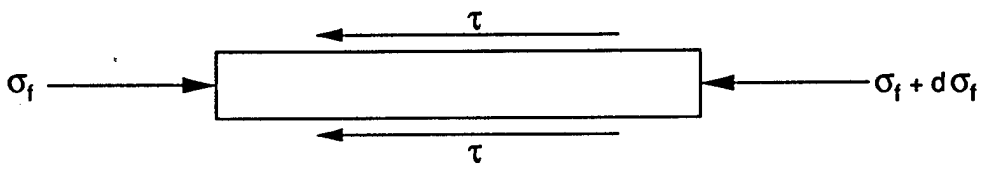

Figure 3.3.1. Free body diagram of a single-fiber segment.

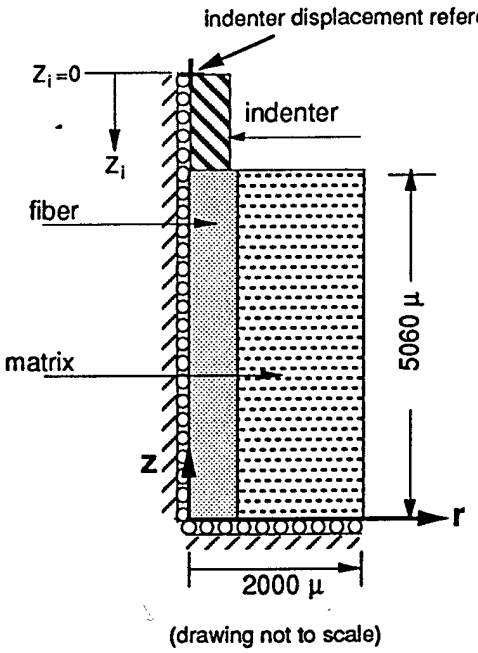

Figure 3.3.2. Finite element model for single-fiber micro-indentation specimen

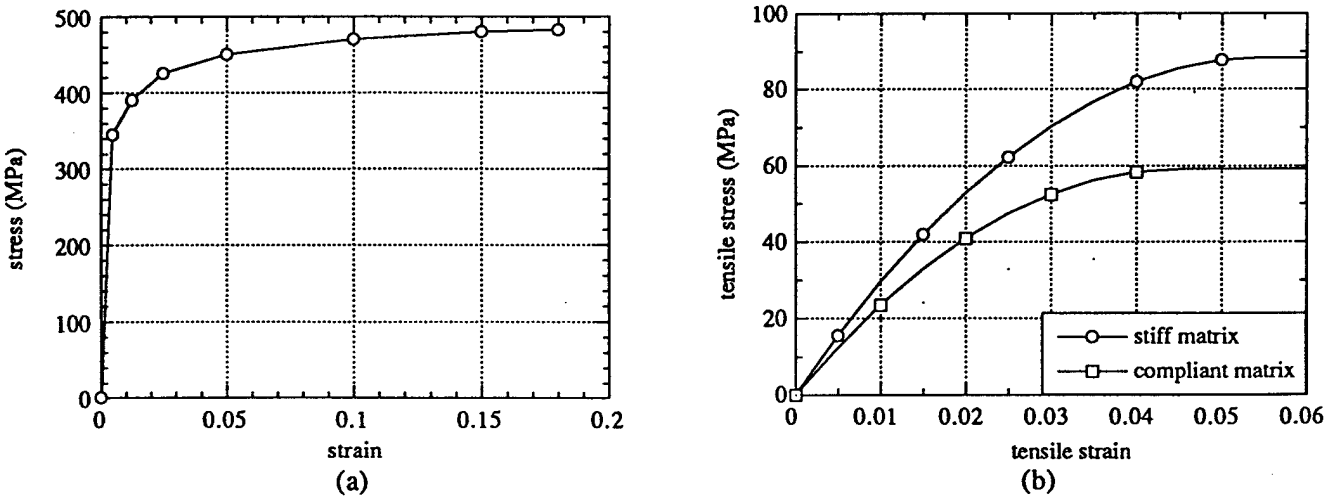

Figure 3.3.3. Constituent material behaviors for (a) aluminum alloy fiber, (b) Epon 828 matrix

Oscillating Behavior and Complex Modulus

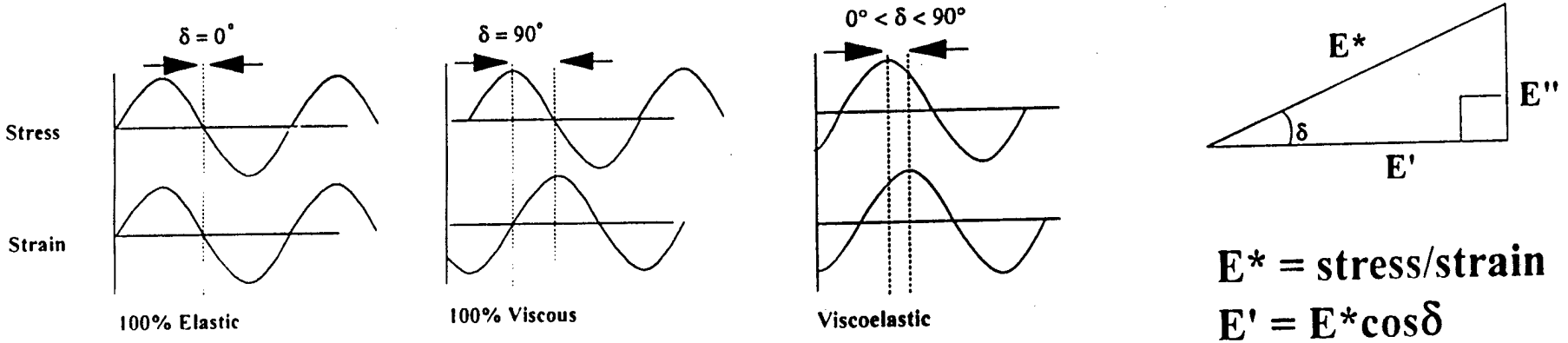

Figure 3.4.1 Oscillating Behavior and Complex Modulus

Chemical structure of resin and curing agents

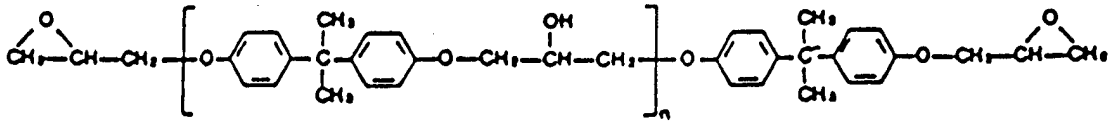

Shell Epon 828

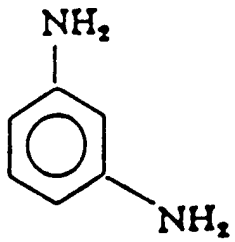

mPDA

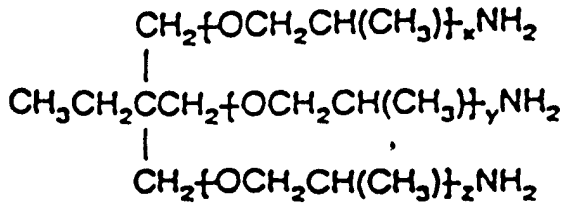

T-403 Jeffamine

Figure 3.4.2. Chemical structure of resin and curing agents

Tensile Clamping on the DMA

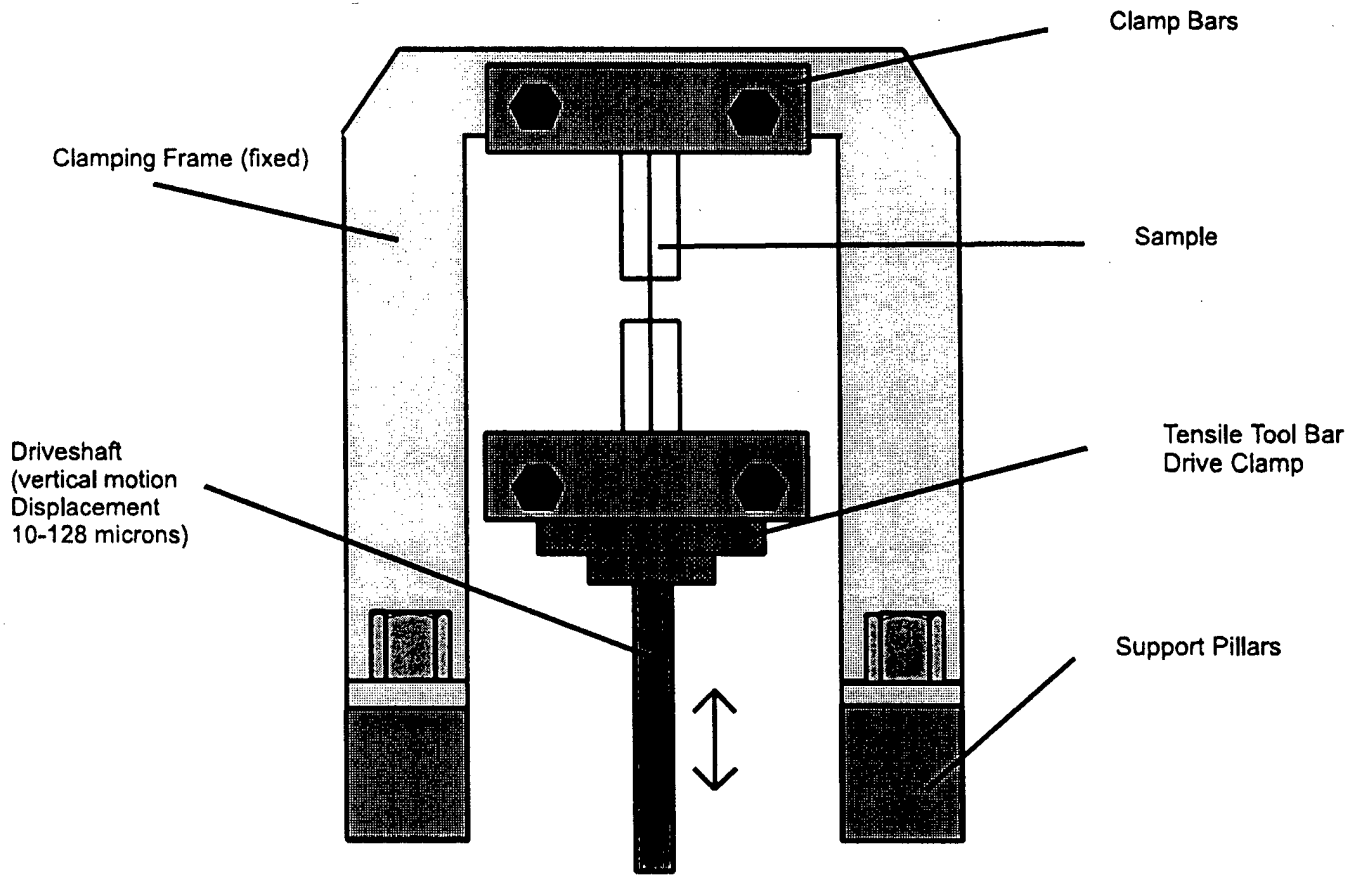

Figure 3.4.3. Tensile Clamping of Sample on the DMA

Photo of the Rheometrics DMA Mk III and the tensile clamping

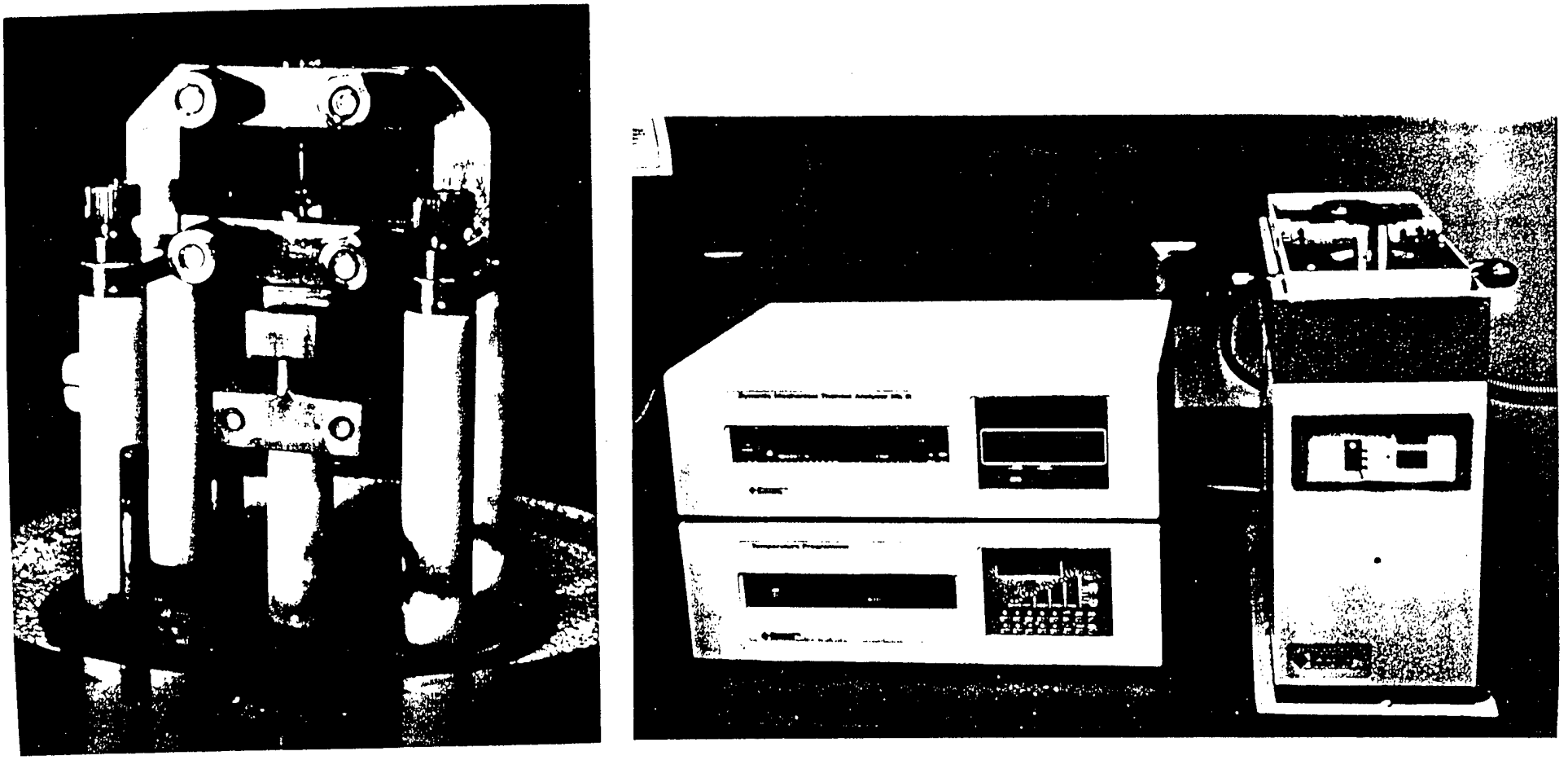

Figure 3.4.4. Photo of the Rheometrics DMA MkIII and the tensile clamps

Sample dimensions

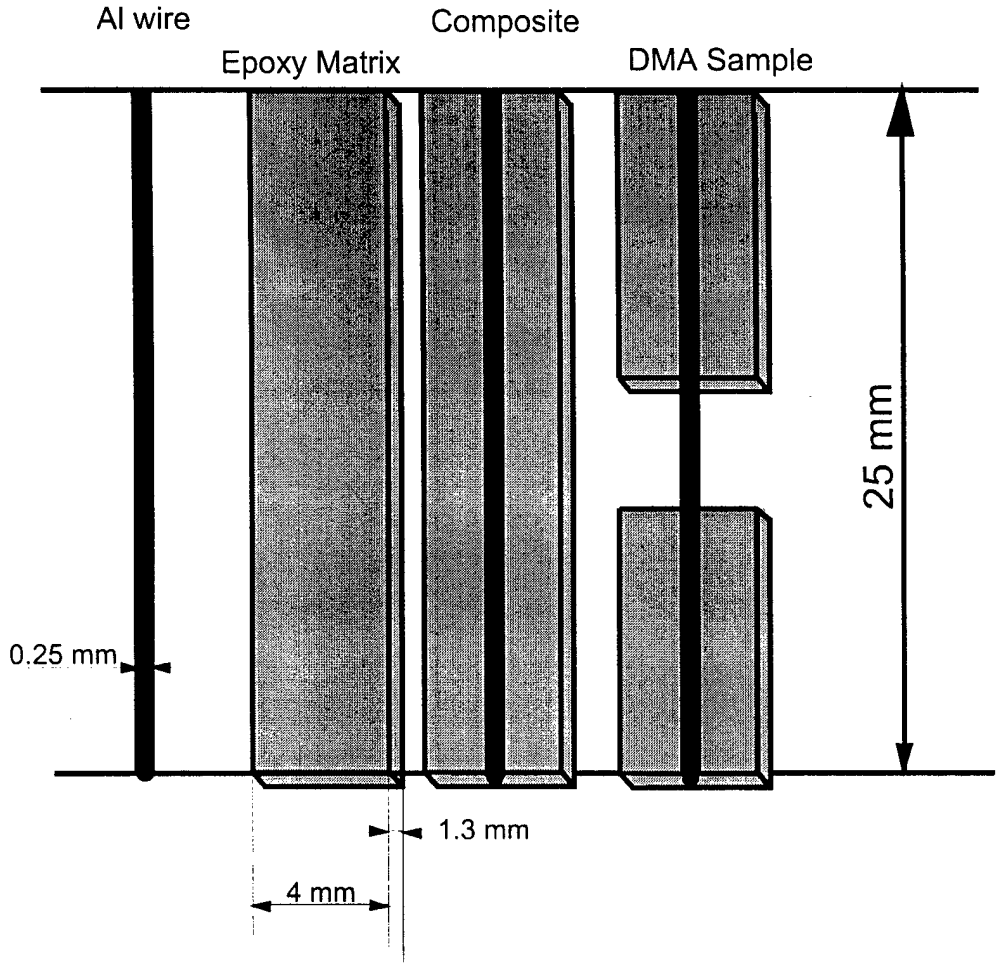

Figure 3.4.5. Sample dimensions

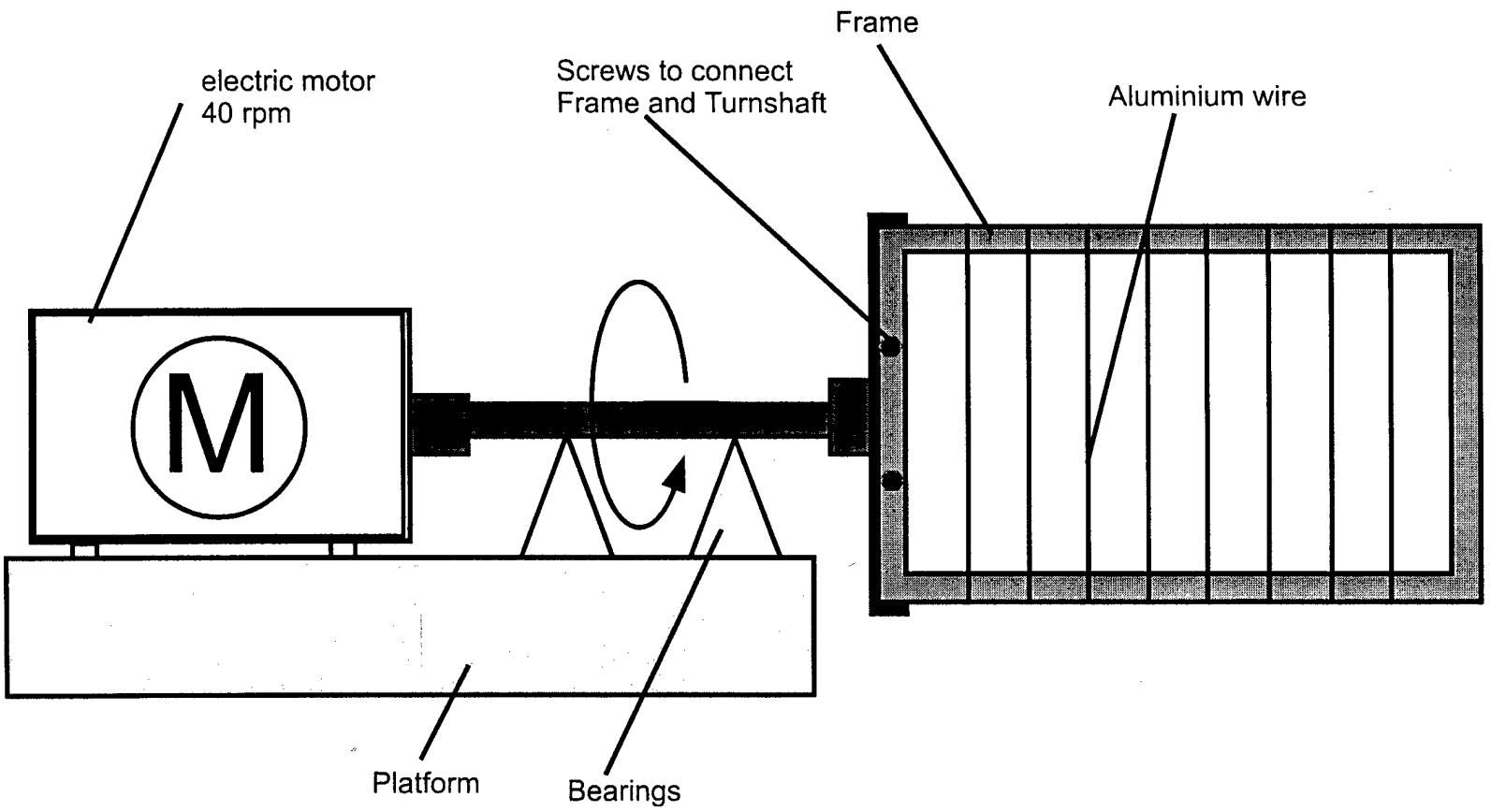

Figure 3.4.6. Motor bench to rotate frame with coated fibers

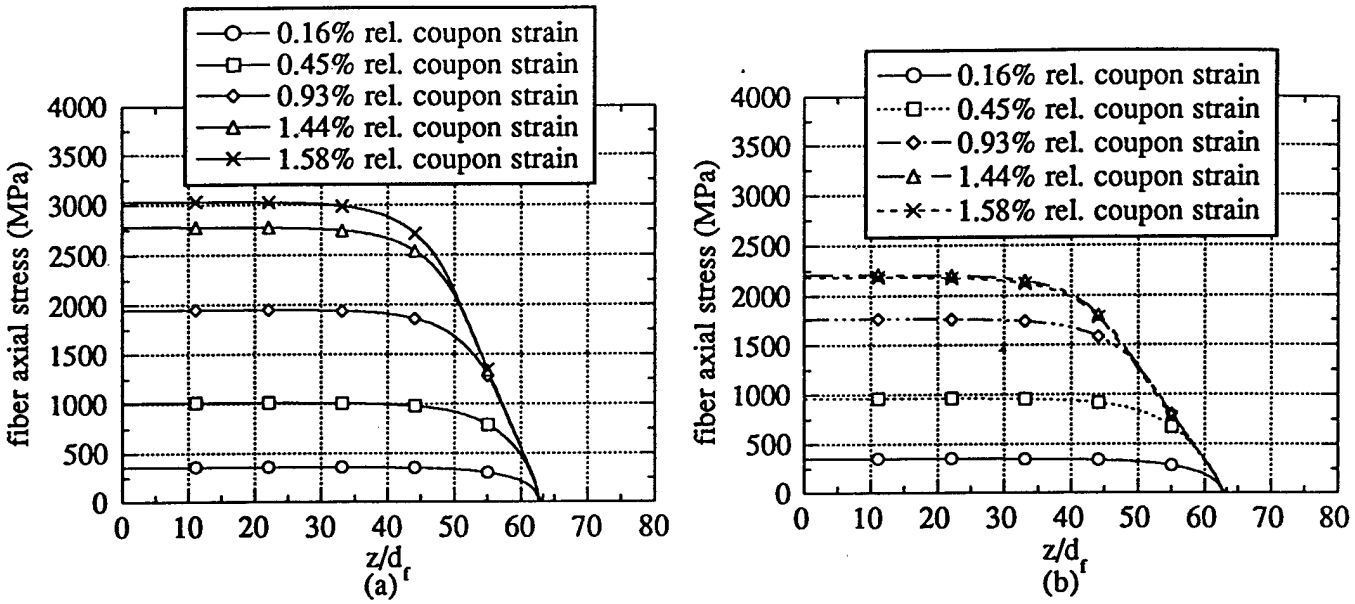

Figure 4.1.1. Fiber axial stress distributions for fragments at (a) 1% and (b) 2% matrix strains.

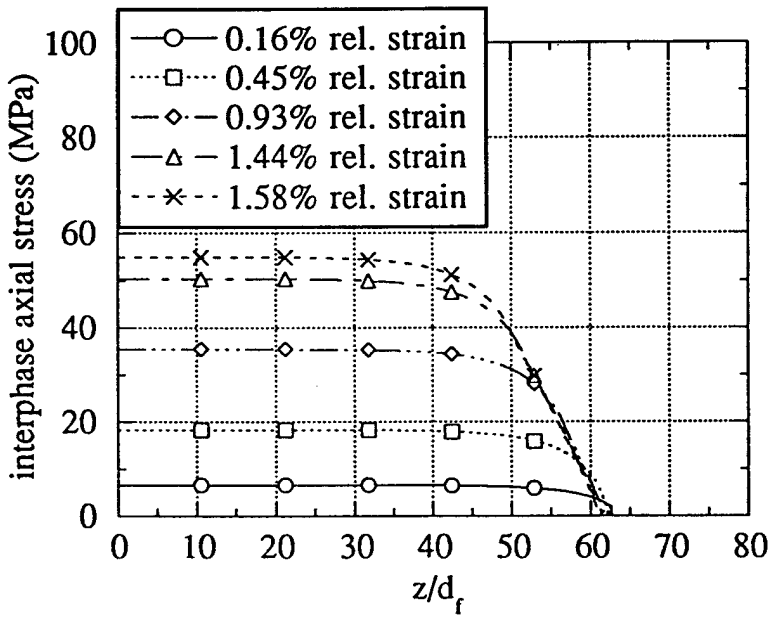

Figure 4.1.2. Interphase axial stress distribution for fragments created at 1% matrix strains.

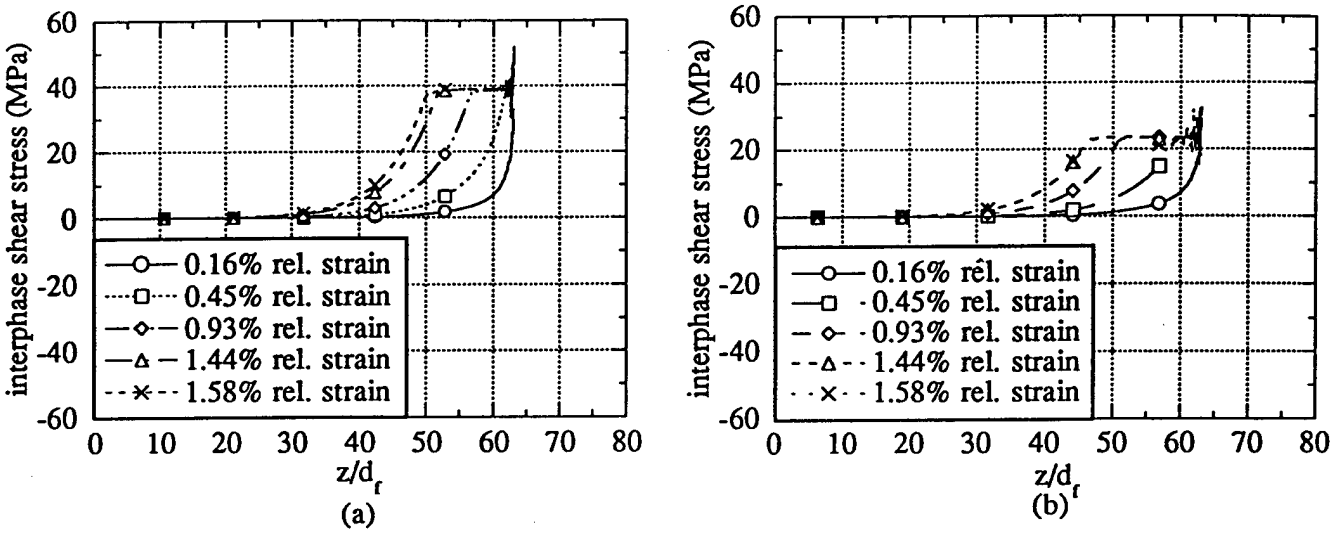

Figure 4.1.3. Interphase shear stress distribution for fragments created at (a) 1% and (b) 2% matrix strains.

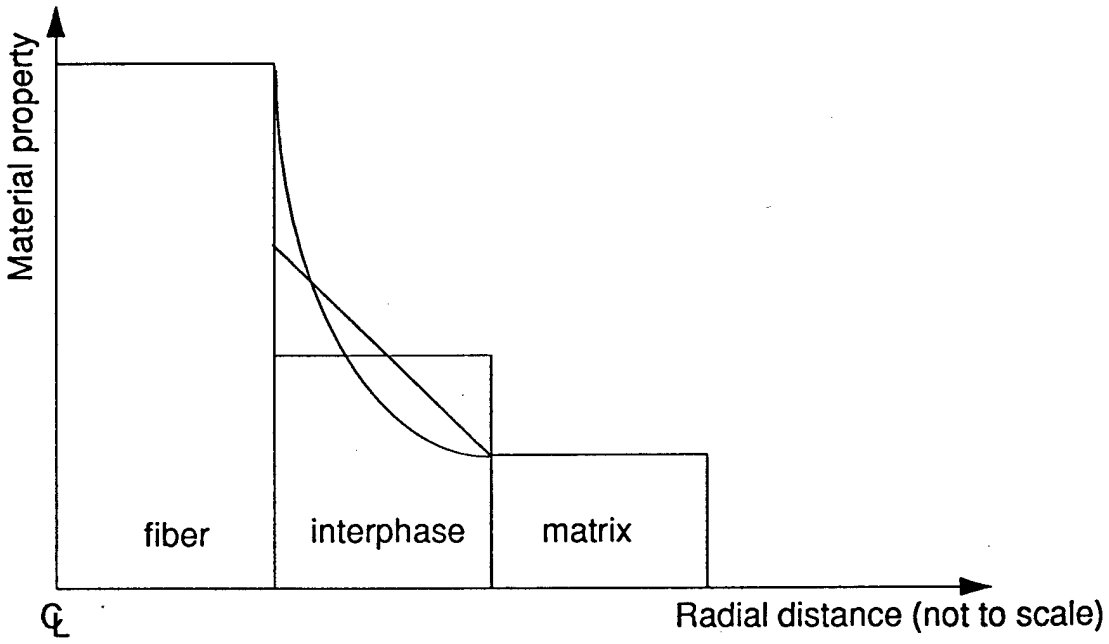

Figure 4.1.4. Interphase property gradients. Uniform, linear and power-law distributions are studied in the analysis. The average interphase properties are the same for the three cases.

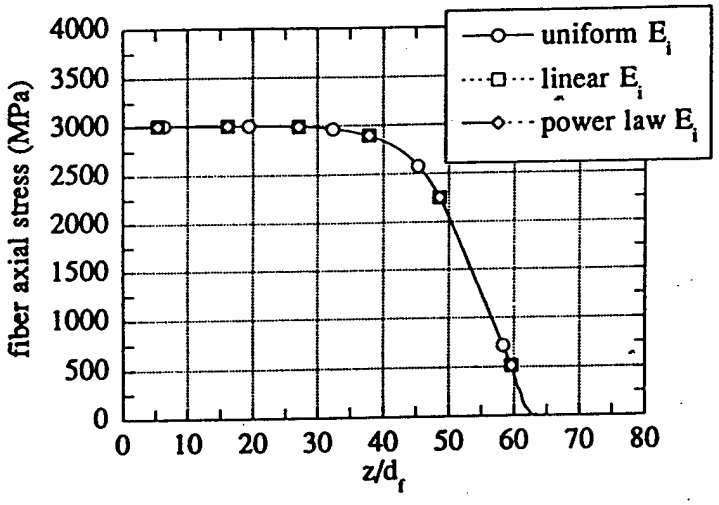

Figure 4.1.5. Fiber axial stress distributions for uniform, linear and power-law interphase property gradients.

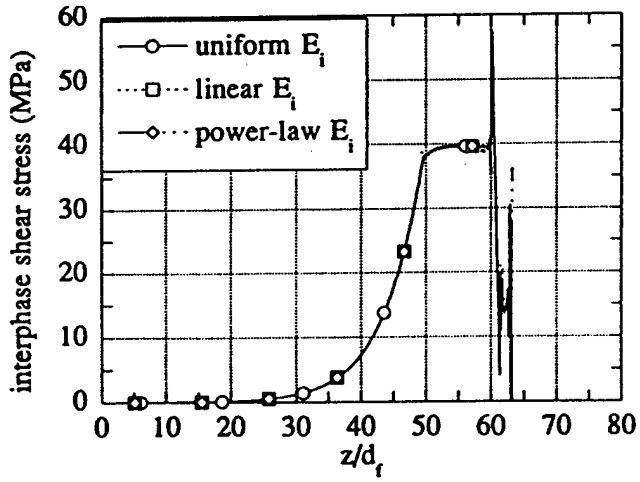

Figure 4.1.6. Interphase shear stress distributions for uniform, linear and power-law interphase property gradients.

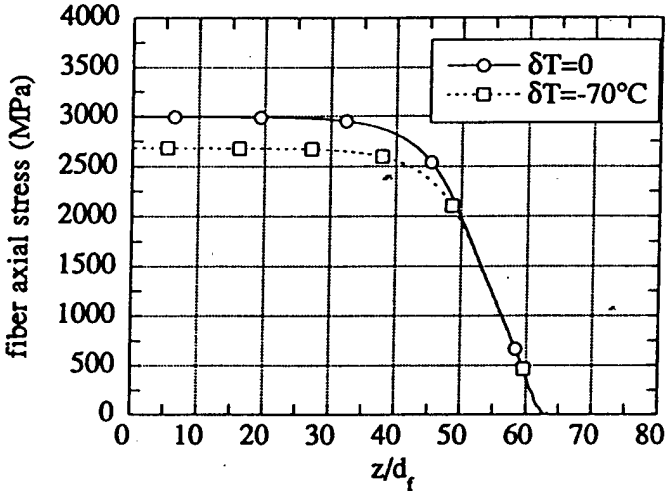

Figure 4.1.7. Fiber axial stress distributions with (∂T=-70°C) and without (∂T=0) thermal residual stresses.

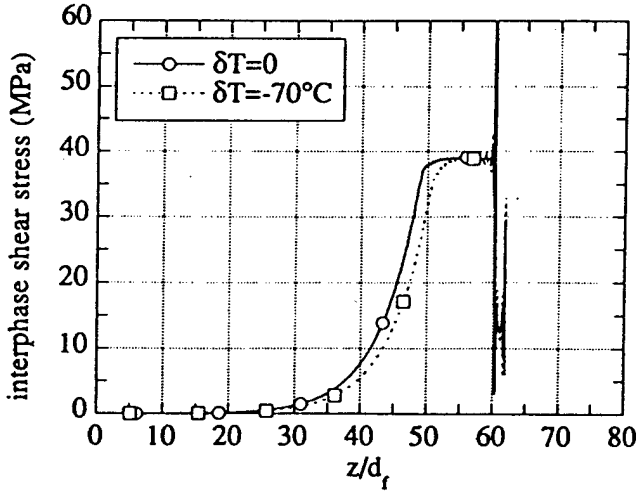

Figure 4.1.8. Interphase shear stress distributions with (∂T=-70°C) and without (∂T=0) thermal residual stresses.

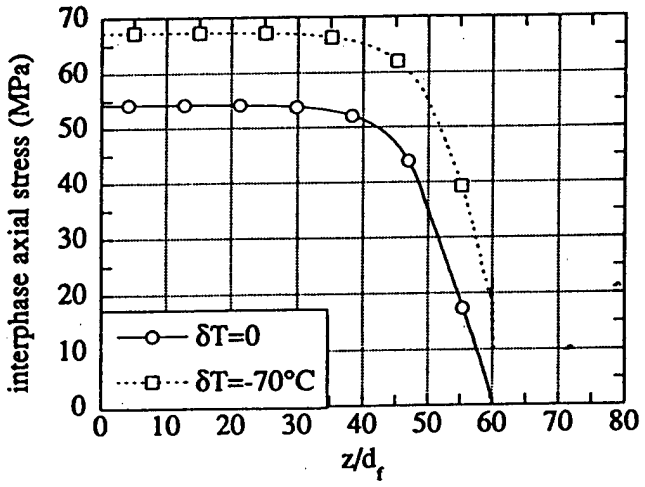

Figure 4.1.9. Interphase axial stress distributions with (∂T=-70°C) and without (∂T=0) thermal residual stresses.

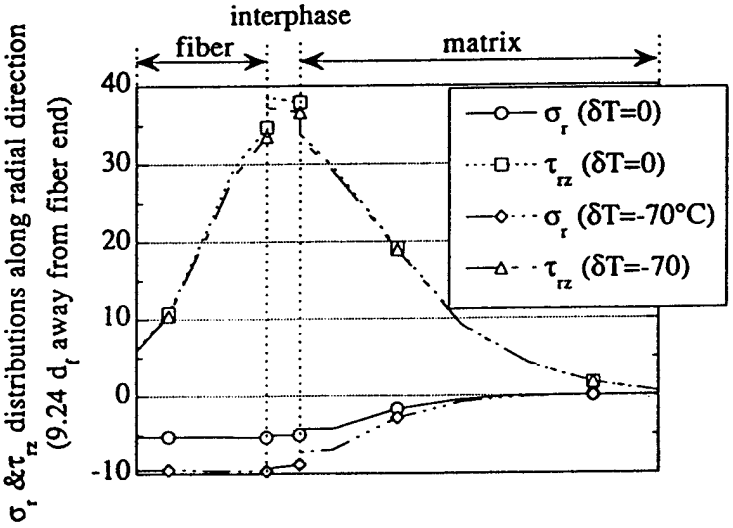

Figure 4.1.10. Radial and shear stress distributions in the radial direction at a plane 9.24 fiber diameters away from the fiber end.

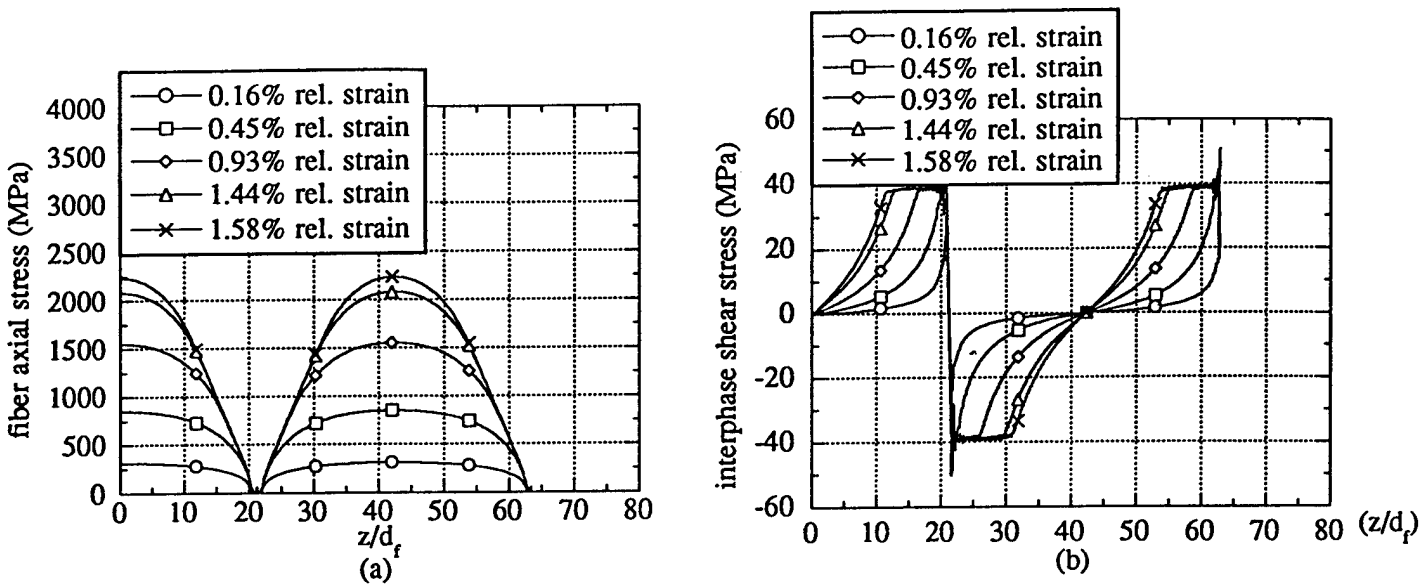

Figure 4.1.11. (a) Fiber axial stress distribution, (b) interphase shear stress distribution for fragments of low aspect ratio, L/df=42.

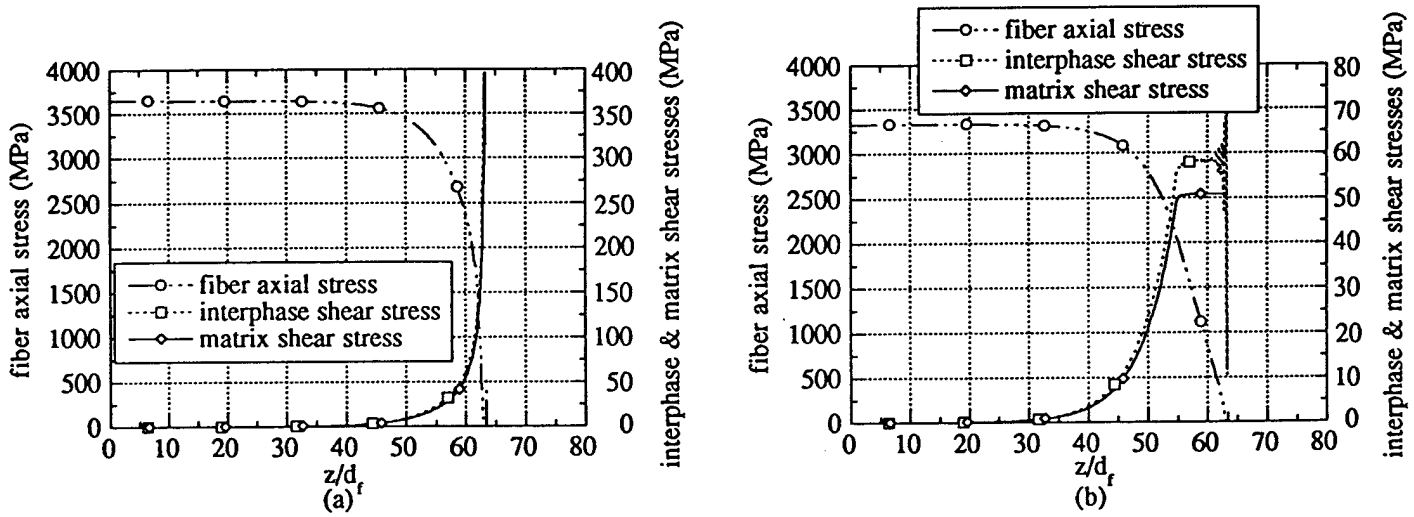

Figure 4.1.12. Fiber axial, interphase and matrix shear stress distributions for finite element analyses assuming (a) linear, (b) non-linear matrix properties. Perfect bond is assumed.

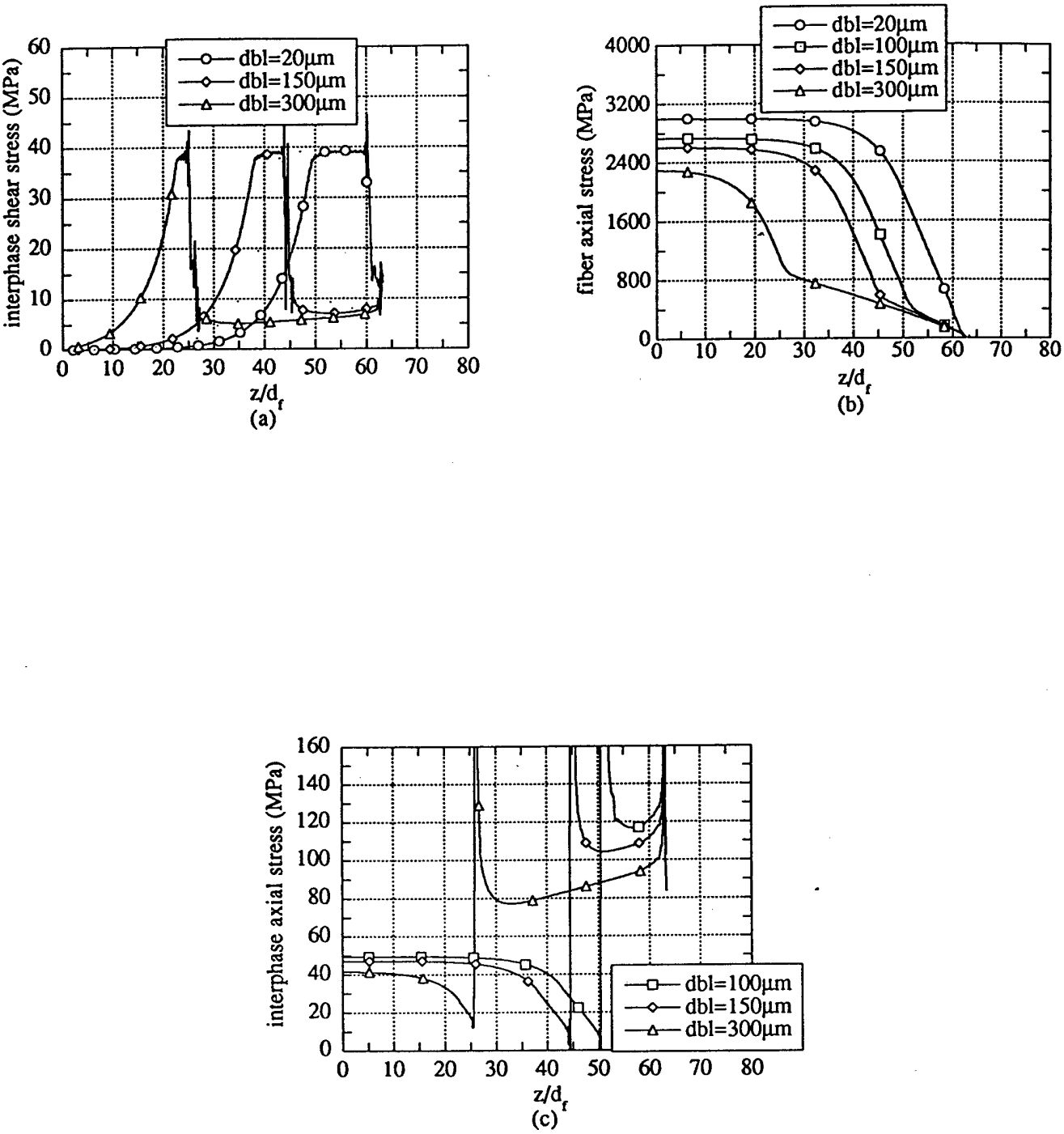

Figure 4.1.13. (a) Interphase shear stress, (b) fiber axial stress, (c) interphase axial stress distributions for fragments with various fiber/interphase debond lengths.

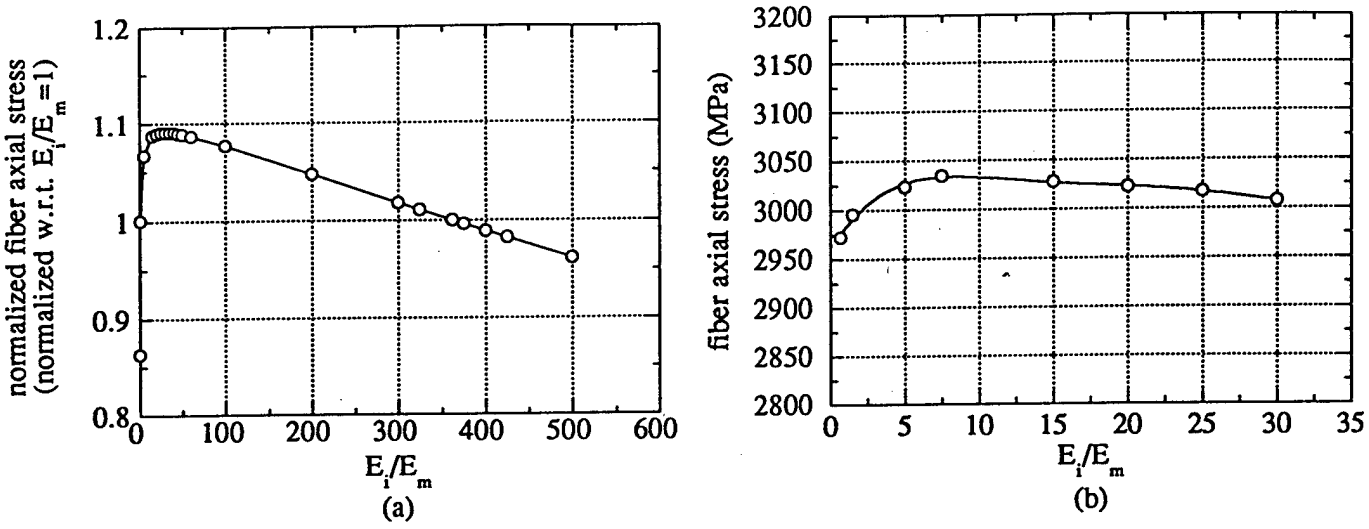

Figure 4.1.14. Maximum fiber axial stress as a function of E_i/E_m from (a) linear, (b) nonlinear finite element analysis.

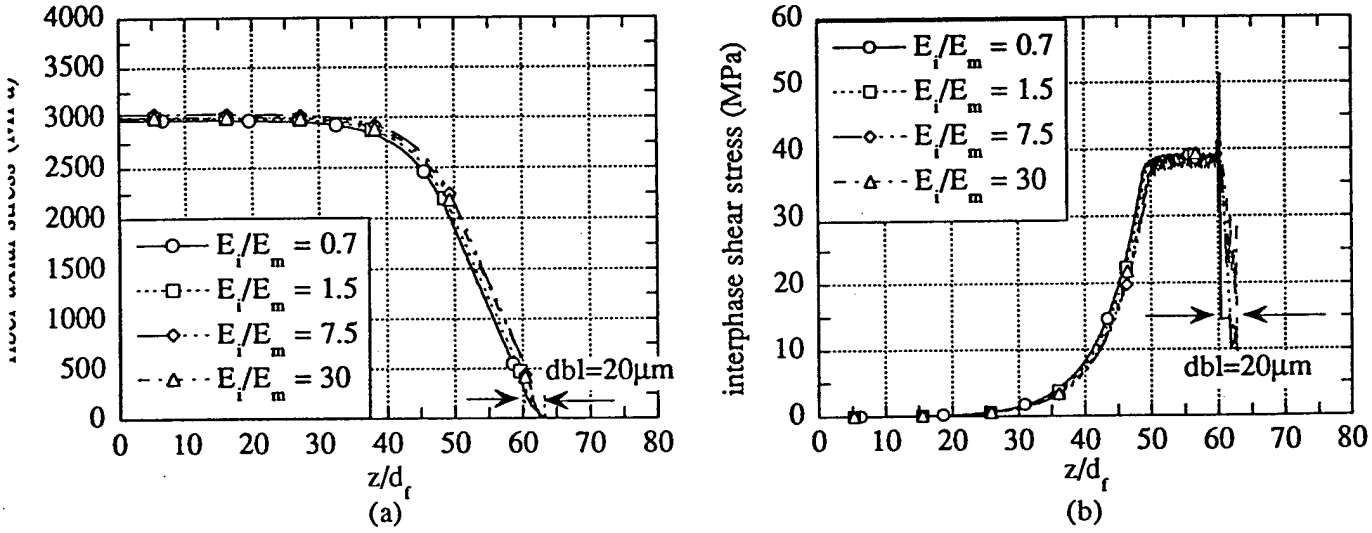

Figure 4.1.15. (a) Fiber axial, (b) interphase shear stress distributions for fragments with various E_i/E_m ratios. A 20 microns debond length is assumed at the fiber break.

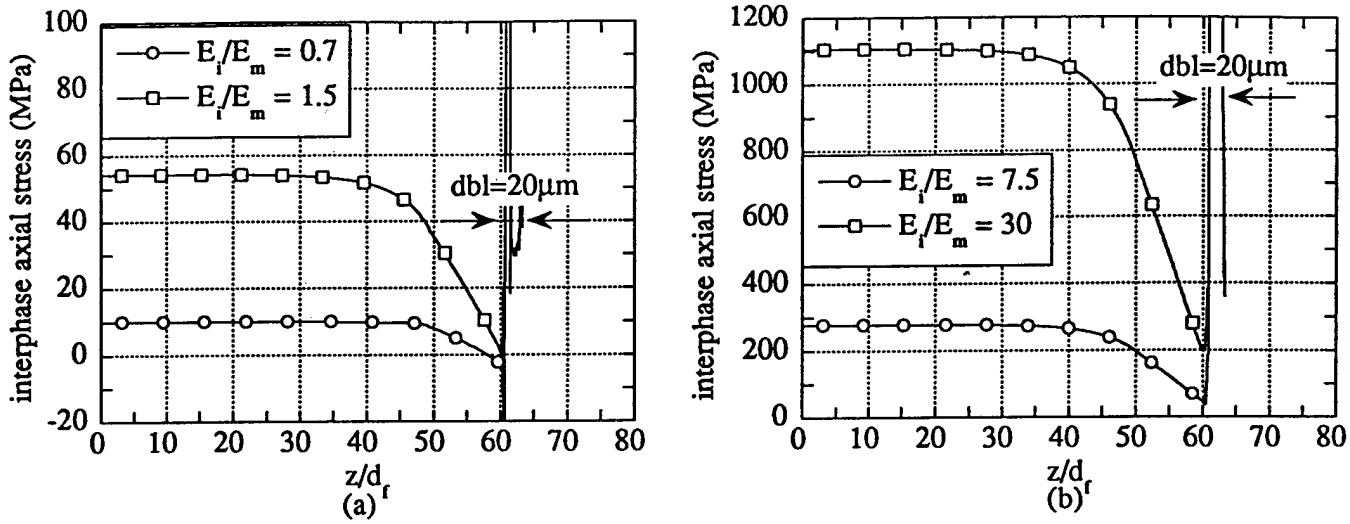

Figure 4.1.16. Interphase axial stress distributions for (a) E_i/E_m=0.7 and 1.5, (b) E_i/E_m=7.5 and 30. A 20 microns debond length is assumed at the fiber break.

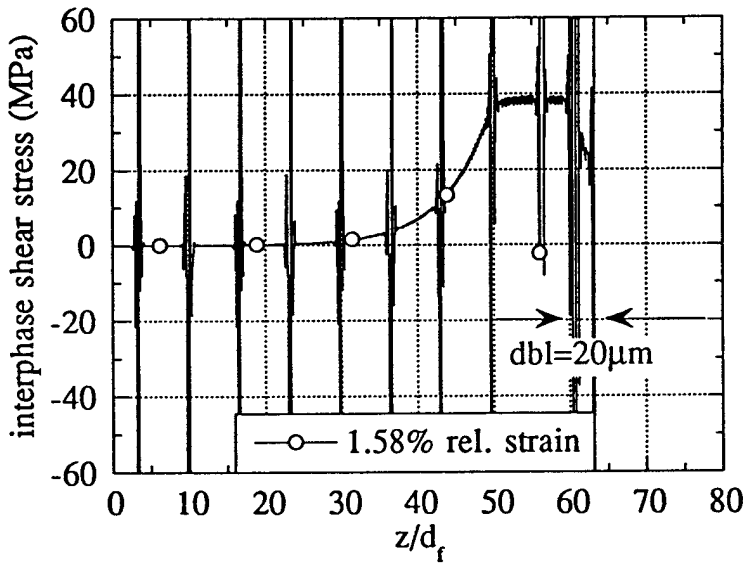

Figure 4.1.17. Effect of interphase fractures on the shear stress distributions for fragments with various interphase thickness for E_i/E_m=30. A 20 microns debond length is assumed at the fiber break.

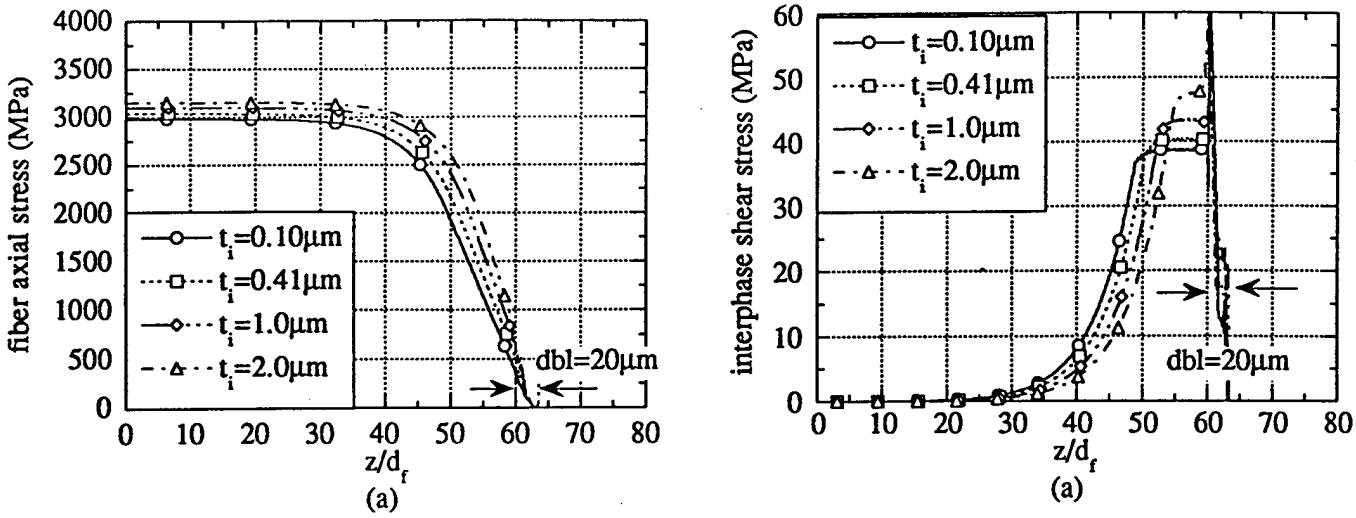

Figure 4.1.18. (a) Fiber axial, (b) interphase shear stress distributions for fragments with various interphaase thickness for E_i/E_m=1.8. A 20 microns debond length is assumed at the fiber break.

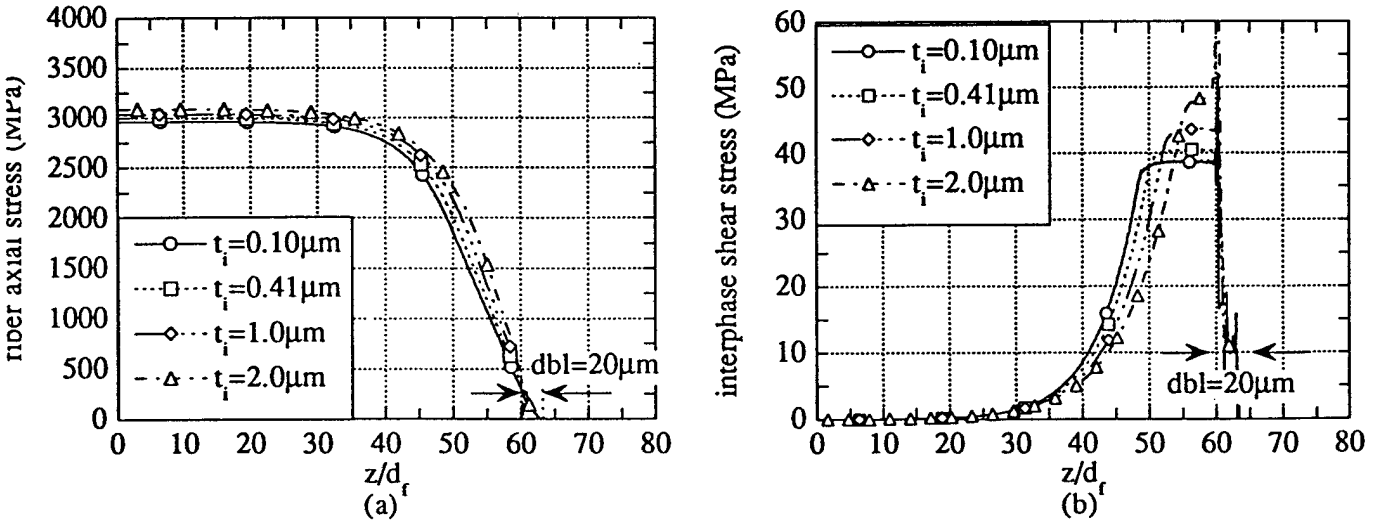

Figure 4.1.19. (a) Fiber axial, (b) inerphase shear stress distributions for fragments with various interphase thickness for E_i/E_m=0.3. A 20 microns debond length is assumed at the fiber break.

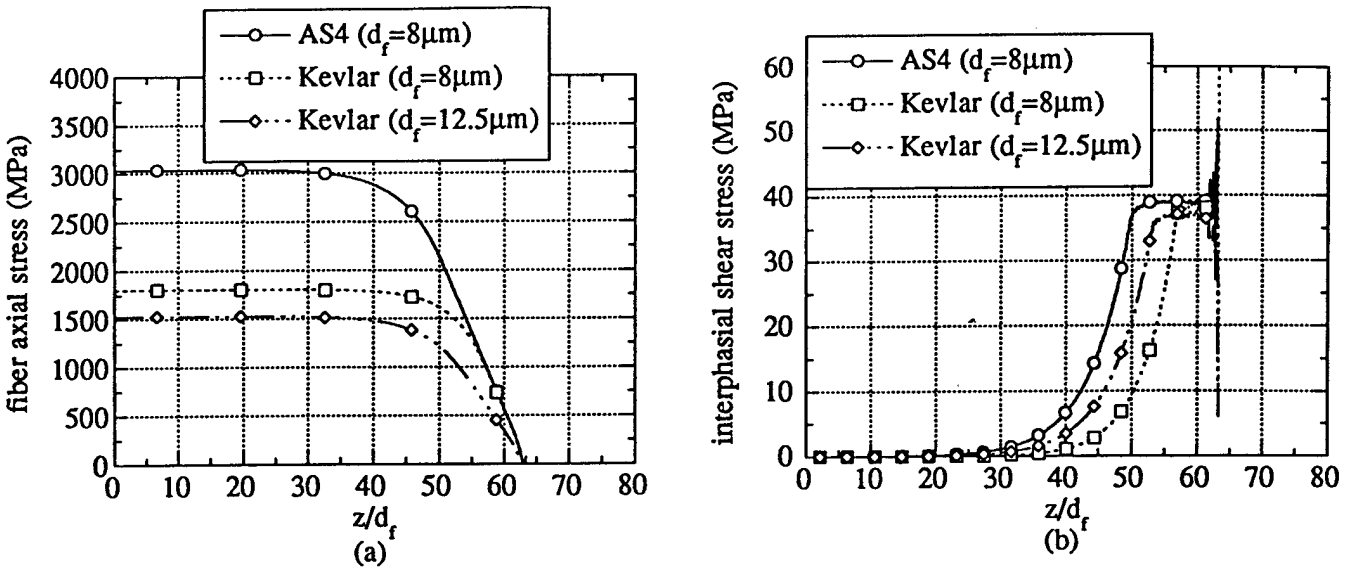

Figure 4.1.20. (a) Fiber axial, (b) interphase shear stress distributions for AS4, Kevlar I (df=8 microns) and Kevlar II (df=12.5 microns) fiber fragments. Perfect bond is assumed.

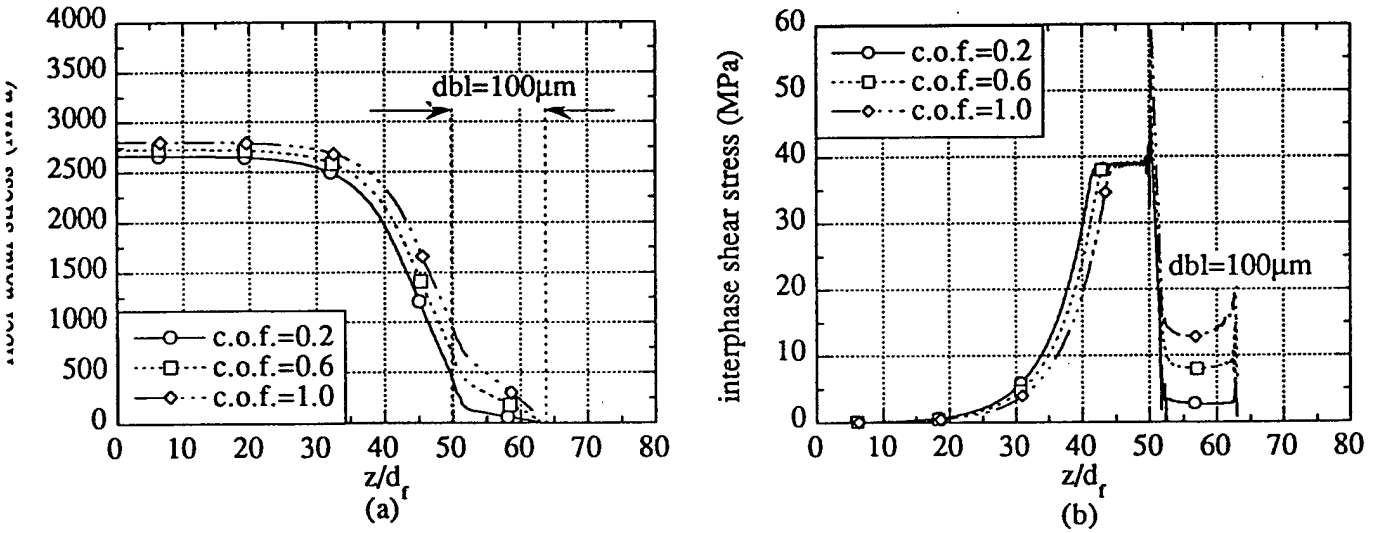

Figure 4.1.21. (a) Fiber axial stress distributions from direct finite element result and from curve-fitting, (b) interphase shear stress distributions from direct finite element result and from curve-fitted fiber stress using equation (17).

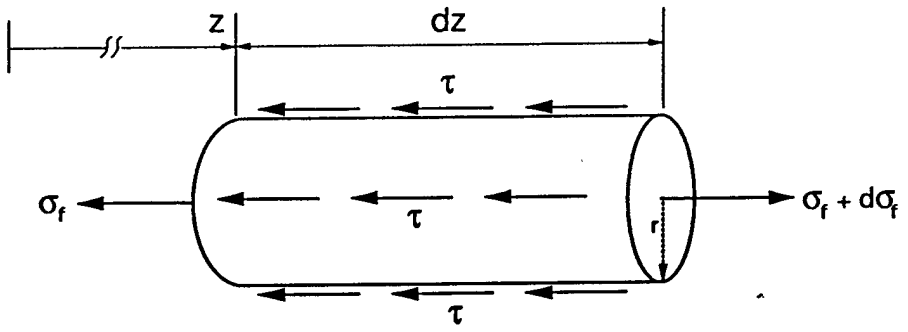

Figure 4.1.22. The force equilibrium of a volume element of a single fiber in infinite matrix.

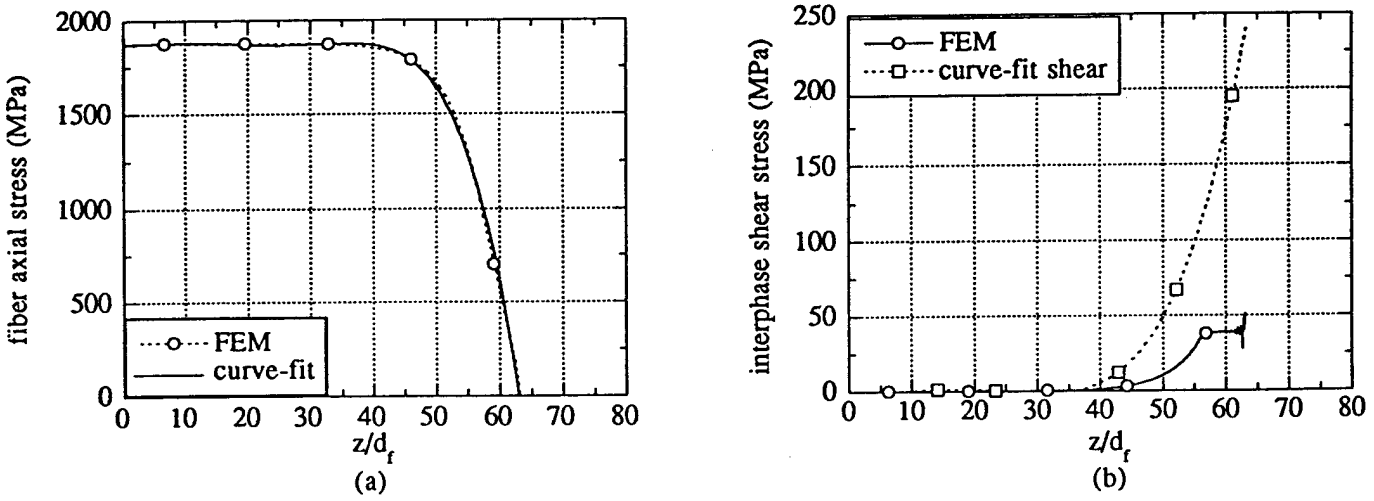

Figure 4.1.23. (a) Fiber axial stress distributions from direct finite element result and from curve-fitting, (b) interphase shear stress distributions from direct finite element result and from curve-fitted fiber stress using equation (17).

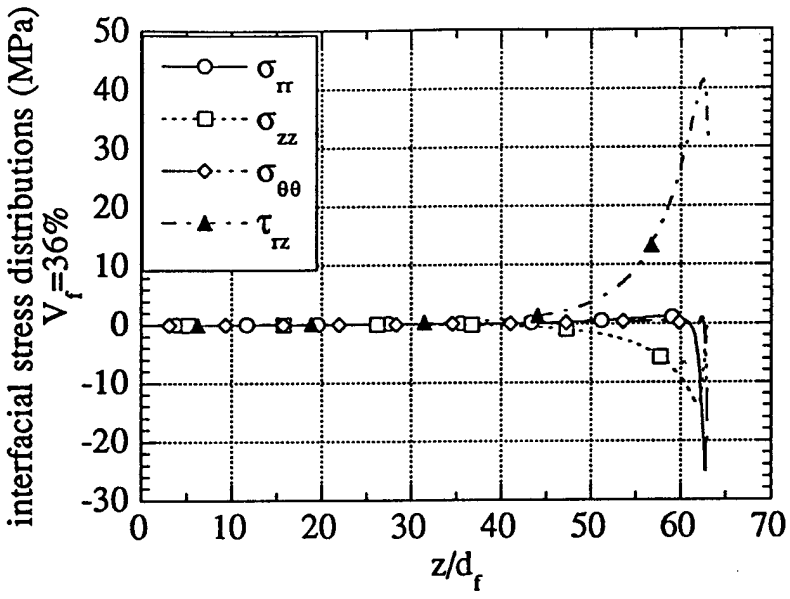

Figure 4.2.1. Interfacial stress distributions along longitudinal z-direction. The perturbed fiber length is about 36 fiber diameters.

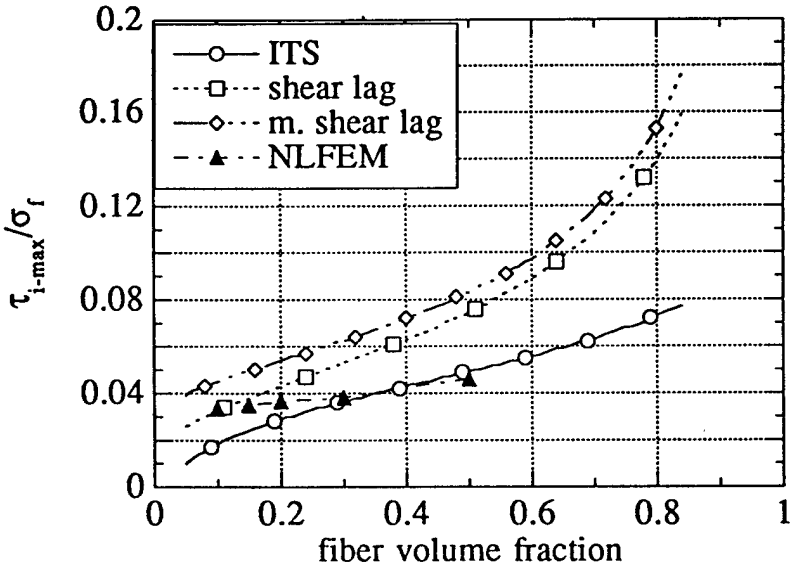

Figure 4.2.2. Normalized maximum interfacial shear stress obtained from nonlinear finite element method (NLFEM), empirical ITS equation (ITS), shear lag and modified shear lag (m. shear lag) equations as a function of fiber volume fraction.

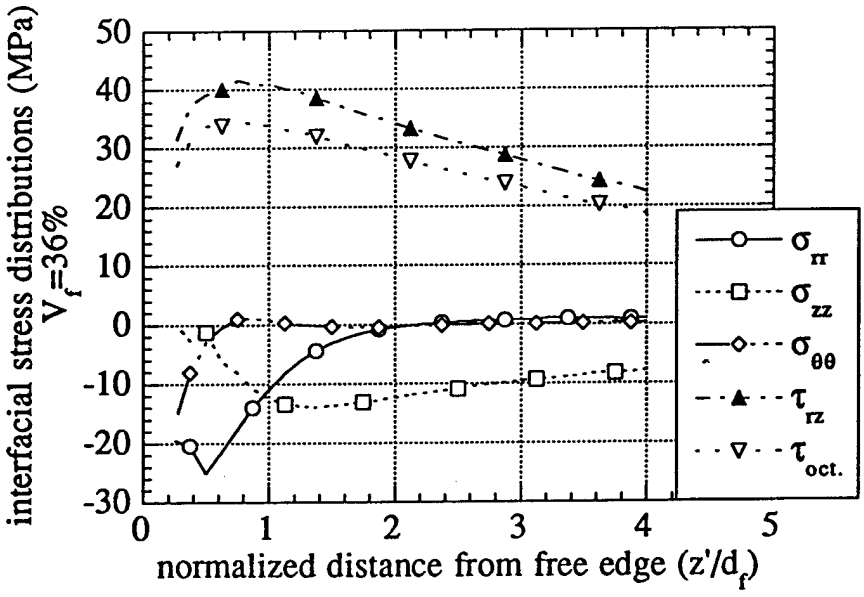

Figure 4.2.3. Interfacial stress distributions along longitudinal z-direction. Vf=36%.

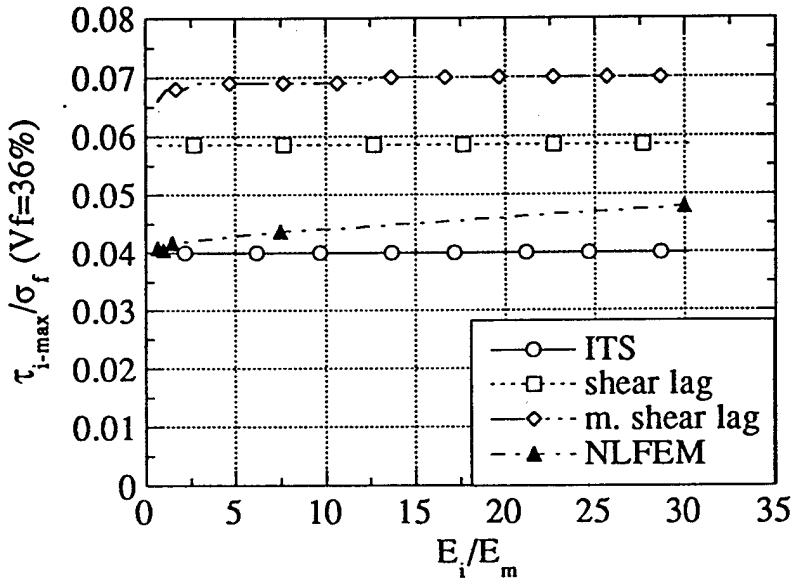

Figure 4.2.4. Normalized maximum interfacial shear stress obtained from nonlinear finite element method (NLFEM), empirical ITS equation (ITS), shear lag and modified shear lag (m. shear lag) equations as a function of normalized interphase modulus. Vf=36%.

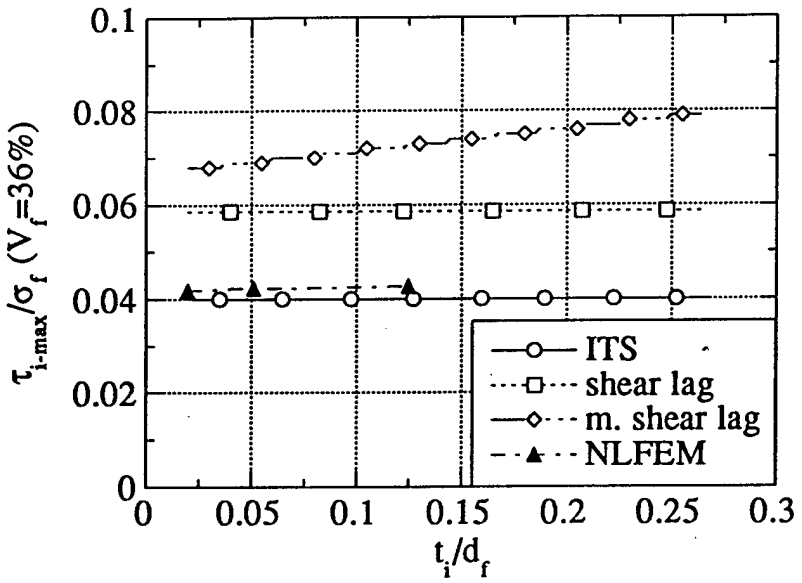

Figure 4.2.5. Normalized maximum interfacial shear stress obtained from nonlinear finite element method (NLFEM), empirical ITS equation (ITS), shear lag and modified shear lag (m. shear lag) equations as a function of normalized interphase thickness. Vf=36%.

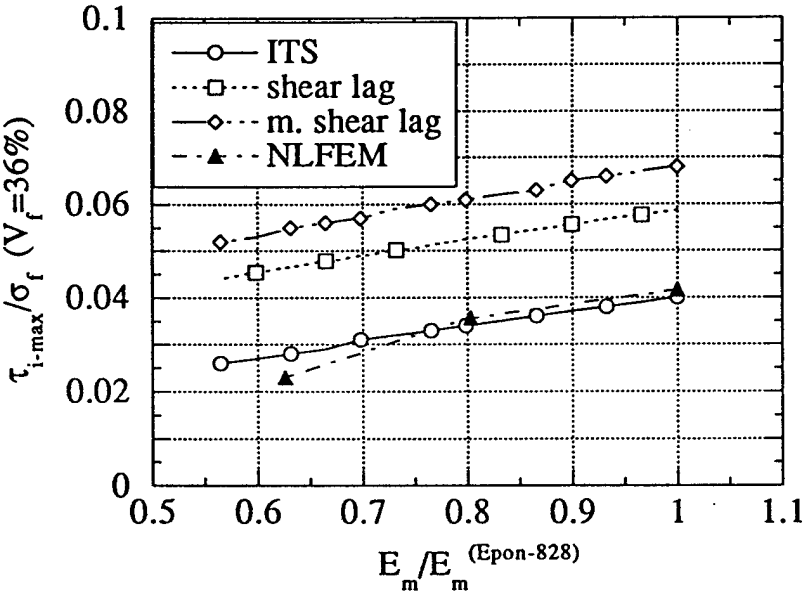

Figure 4.2.6. Normalized maximum interfacial shear stress obtained from nonlinear finite element method (NLFEM), empirical ITS equation (ITS), shear lag and modified shear lag (m. shear lag) equations as a function of normalized matrix stiffness. Vf=36%.

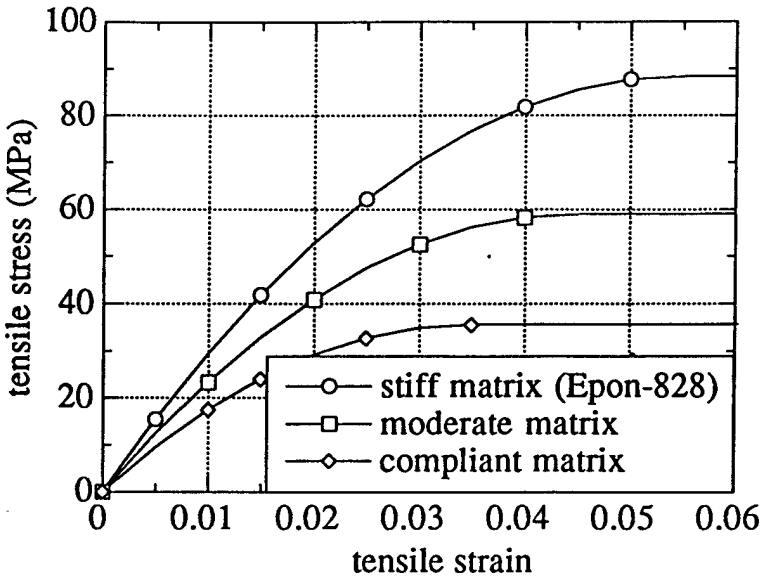

Figure 4.2.7. Constitutive curves for Epon 828 with 14.5 phr of mPDA and two other fictitious more compliant matrix systems.

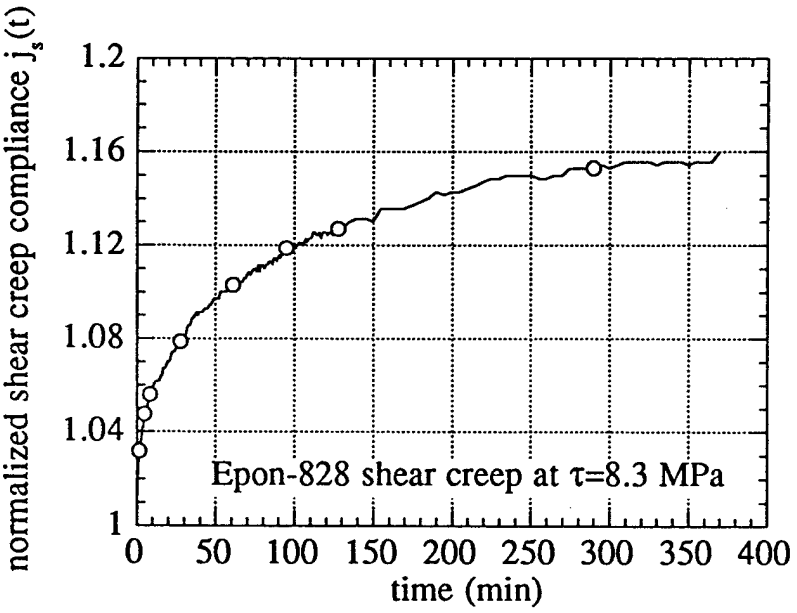

Figure 4.2.8. Time-dependent shear creep compliance of Epon-828 matrix.

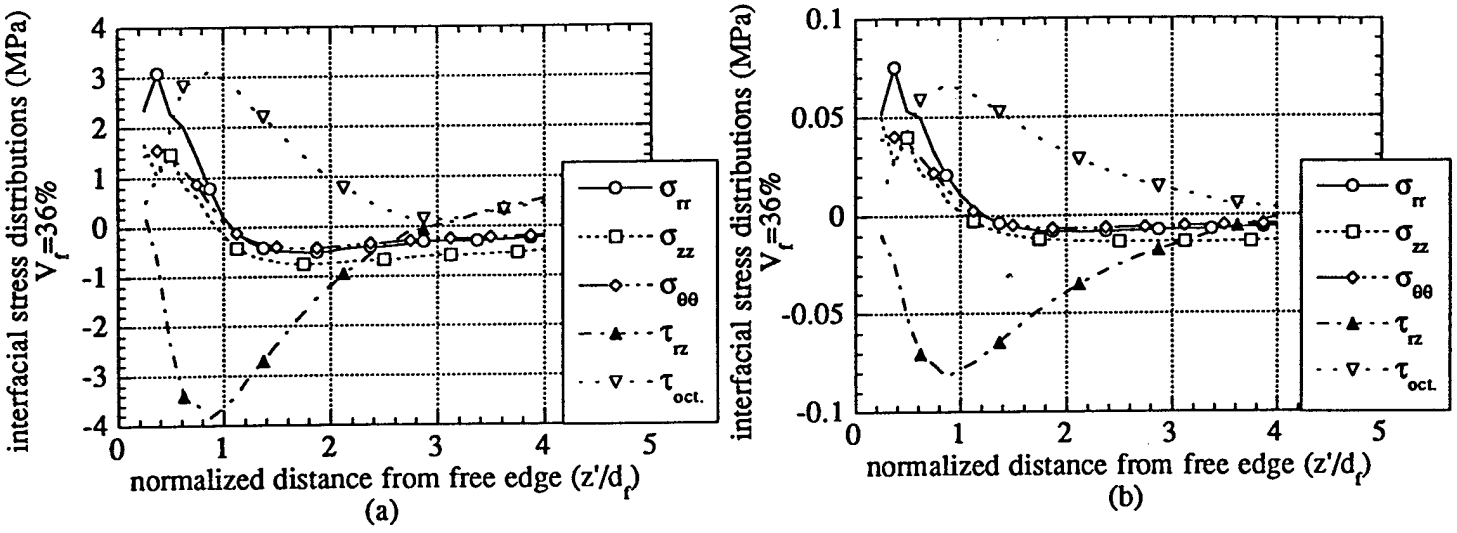

Figure 4.2.9. Interfacial residual stresses along longitudinal z-direction due to (a) nonlinearly elastic/plastic, (b) viscoelastic matrix behavior. Vf=36%.

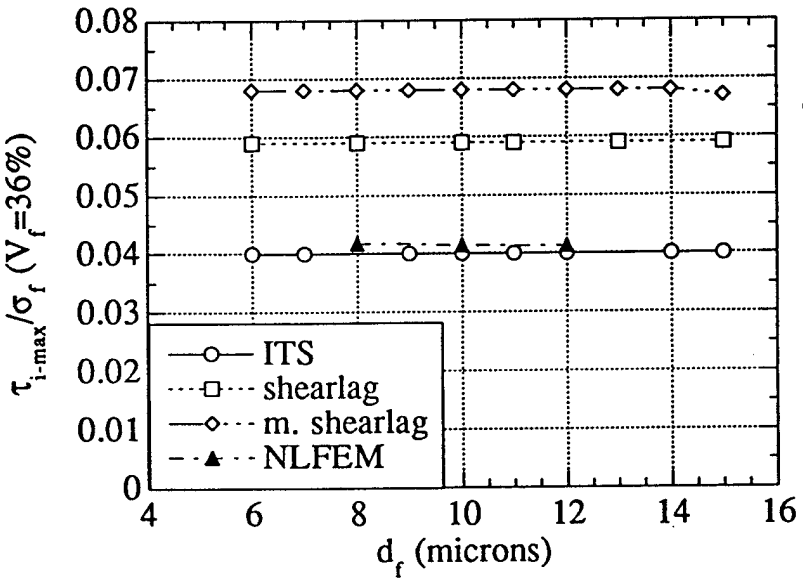

Figure 4.2.10. Normalized maximum interfacial shear stress obtained from nonlinear finite element method (NLFEM), empirical ITS equation (ITS), shear lag and modified shear lag (m. shear lag) equations as a function of fiber diameter. Vf=36%.

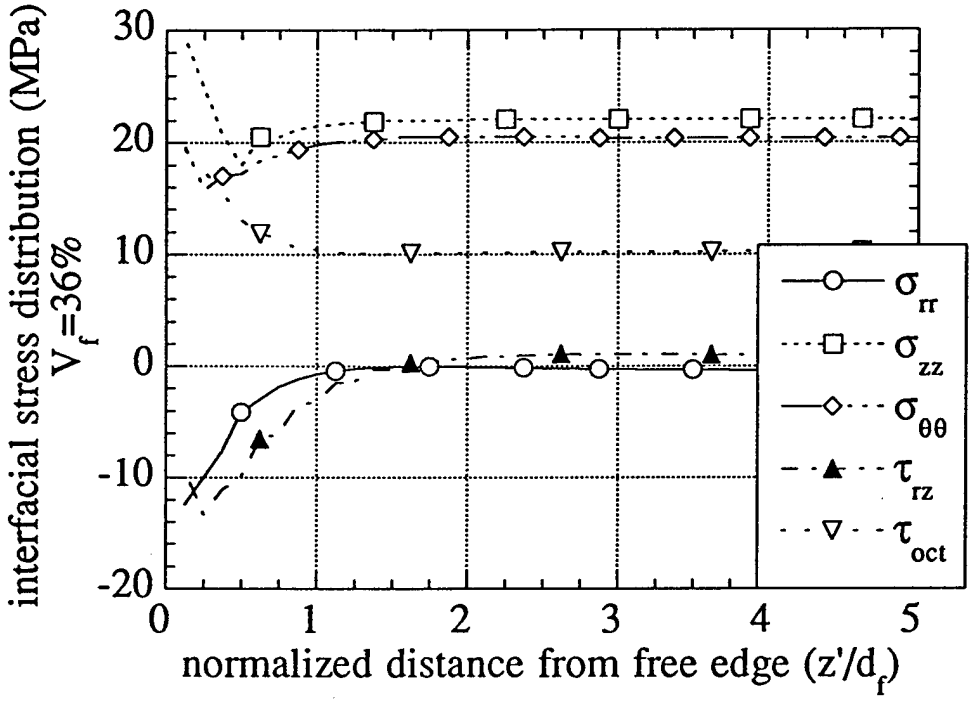

Figure 4.2.11. Interfacial thermal residual stress distributions for ∂T=-70°C. Vf=36%.

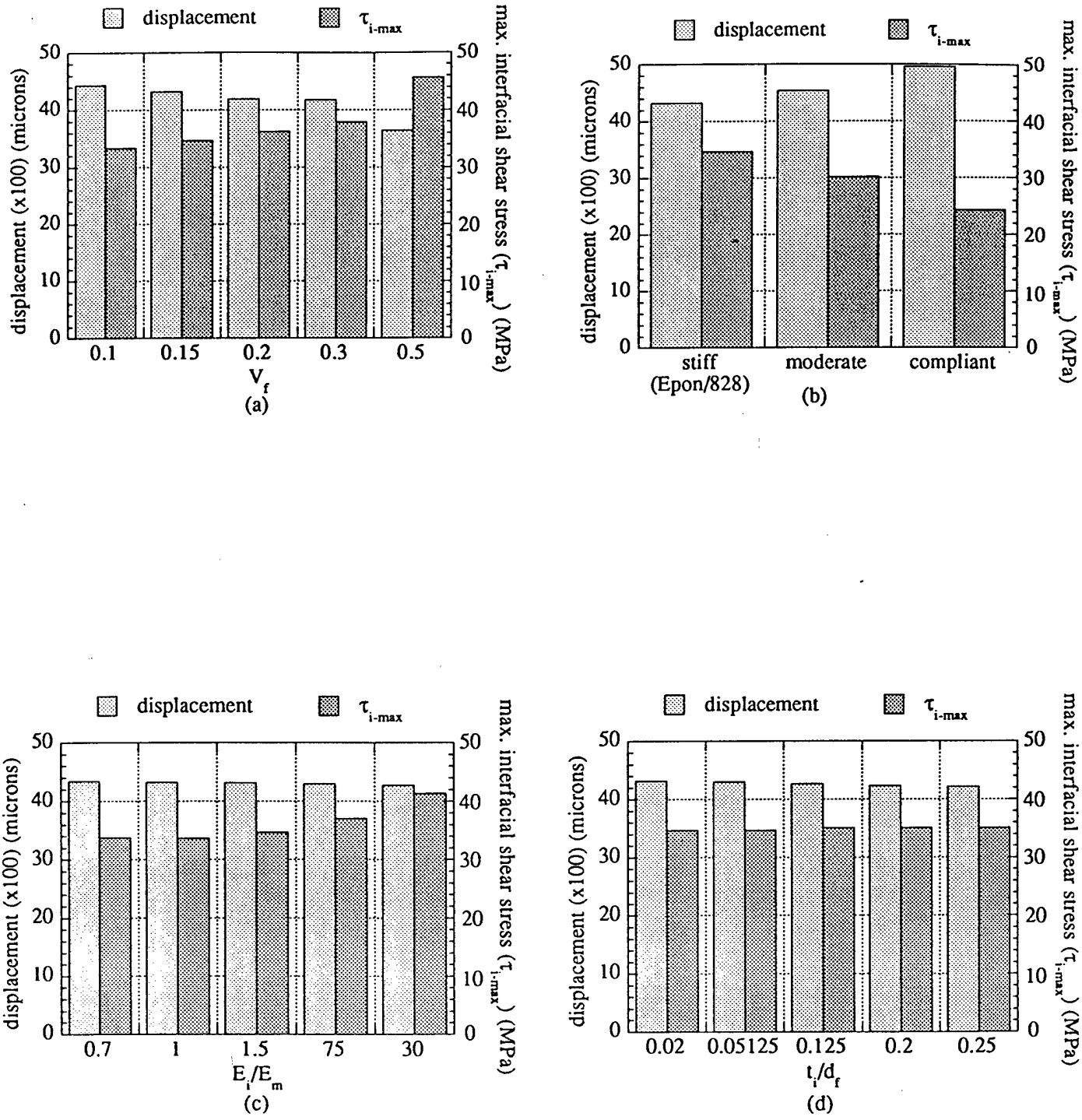

Figure 4.2.12. Indenter displacement and maximum interfacial shear stress as afunction of (a) fiber volume fraction, (b) matrix modulus, (c) interphase modulus, and (d) interphase thickness.

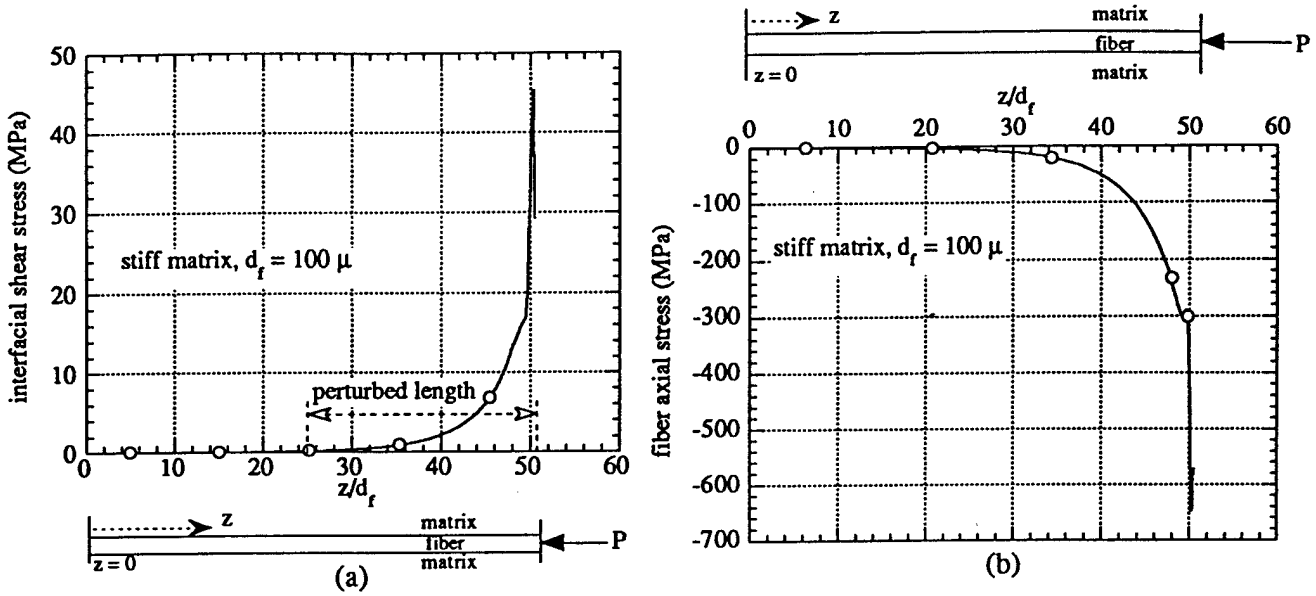

Figure 4.3.1. (a) Interfacial shear stress distribution, (b) fiber axial stress distribution for single aluminum alloy fiber/Epon 828 14.5 phr of mPDA matrix at indenter displacement Zi=4 microns

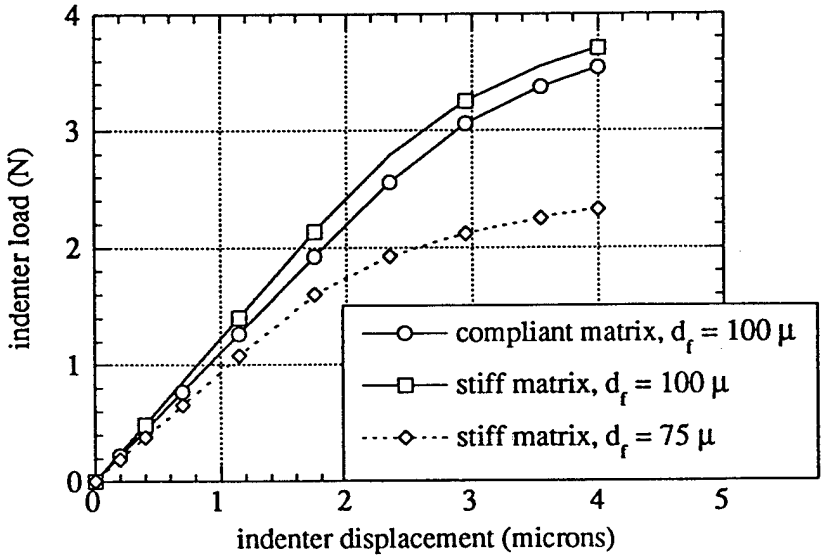

Figure 4.3.2. Load-displacement data for single aluminum alloy fiber/Epon 828 matrix composites. Aluminum alloy is linearly elastic/non-linearly plastic.

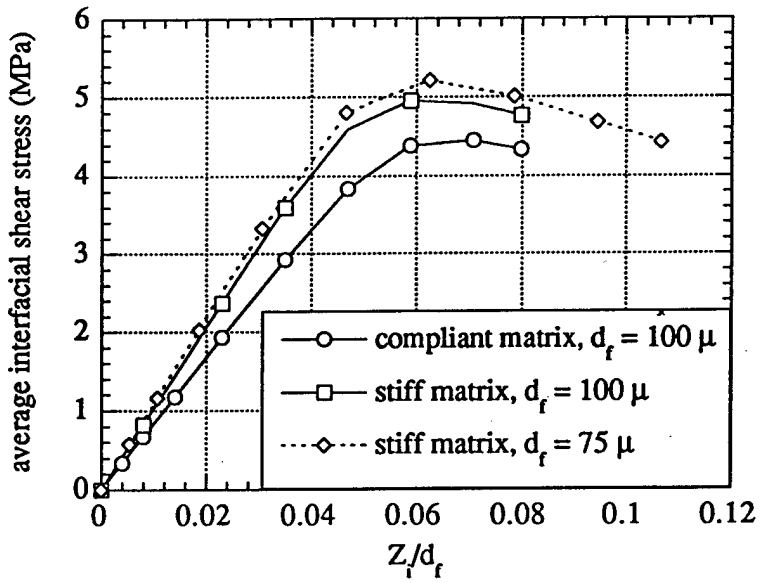

Figure 4.3.3. Average interfacial shear stress-pseudo interfacial shear strain data for single aluminum alloy fiber/Epon 828 matrix composites. Aluminum alloy is linearly elastic/non-linearly plastic.

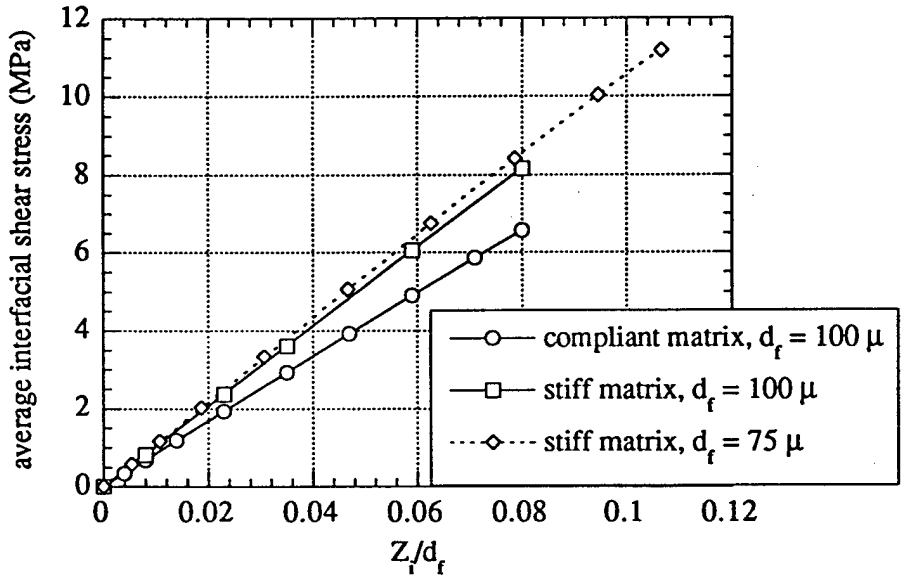

Figure 4.3.4. Average interfacial shear stress-pseudo interfacial shear strain data for single aluminum alloy fiber/Epon 828 matrix composites. Aluminum alloy is linearly elastic.

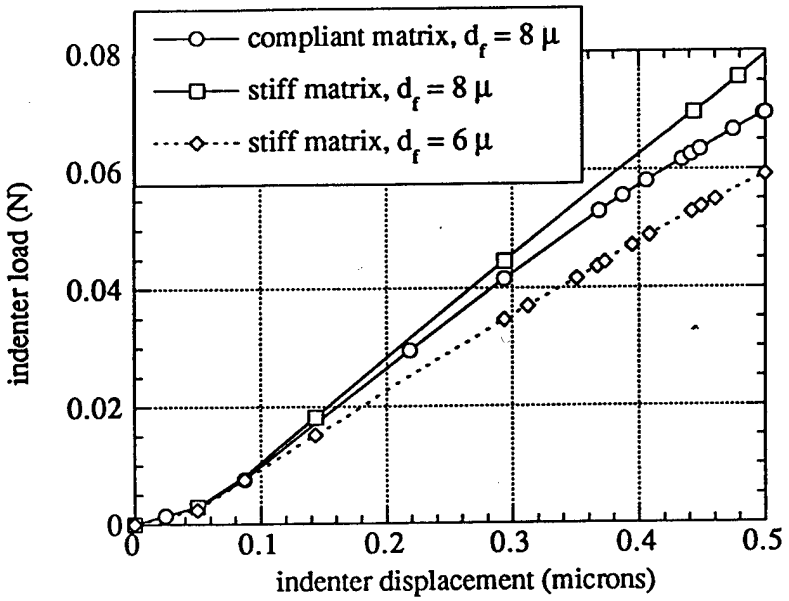

Figure 4.3.5. Load-displacement data for in-situ carbon fiber/Epon 828 matrix composites. Fiber volume fraction is 36%.

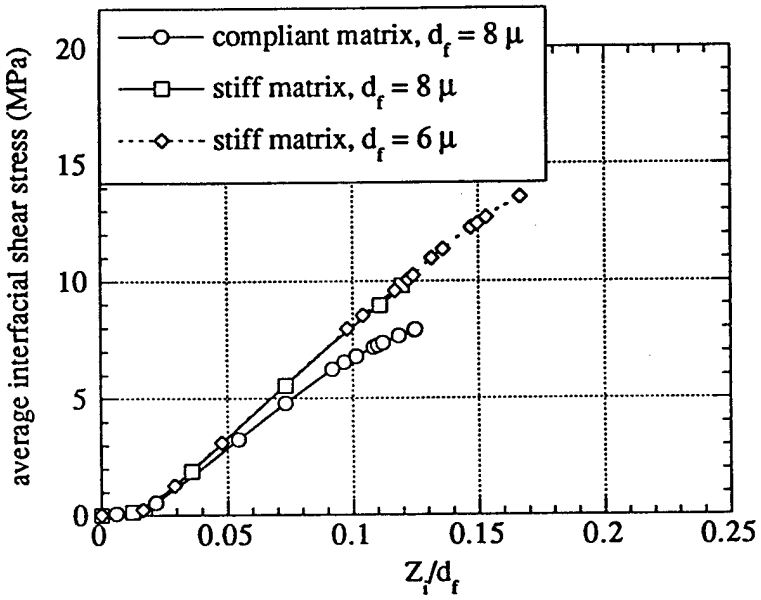

Figure 4.3.6. Average interfacial shear stress-pseudo interfacial shear strain data for in-situ carbon fiber/Epon 828 matrix composites. Fiber volume fraction is 36%.

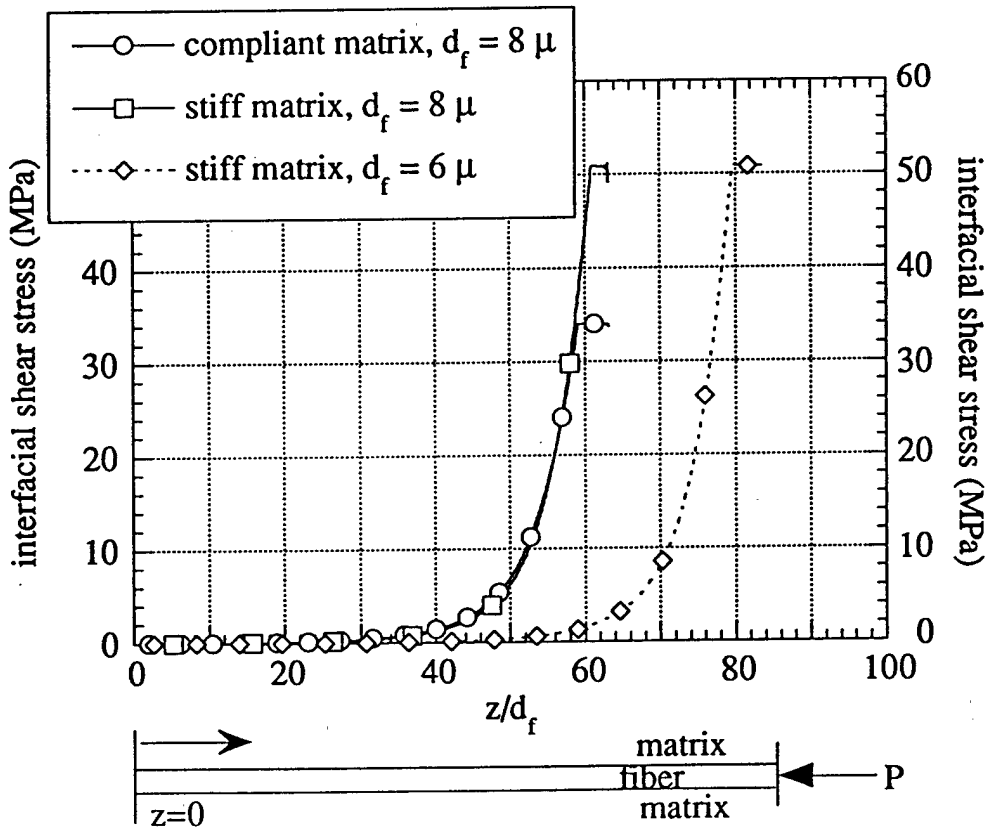

Figure 4.3.7. Interfacial shear stress distribution for in-situ carbon fiber/Epon 828 matrix composites. Fiber volume fraction is 36%.

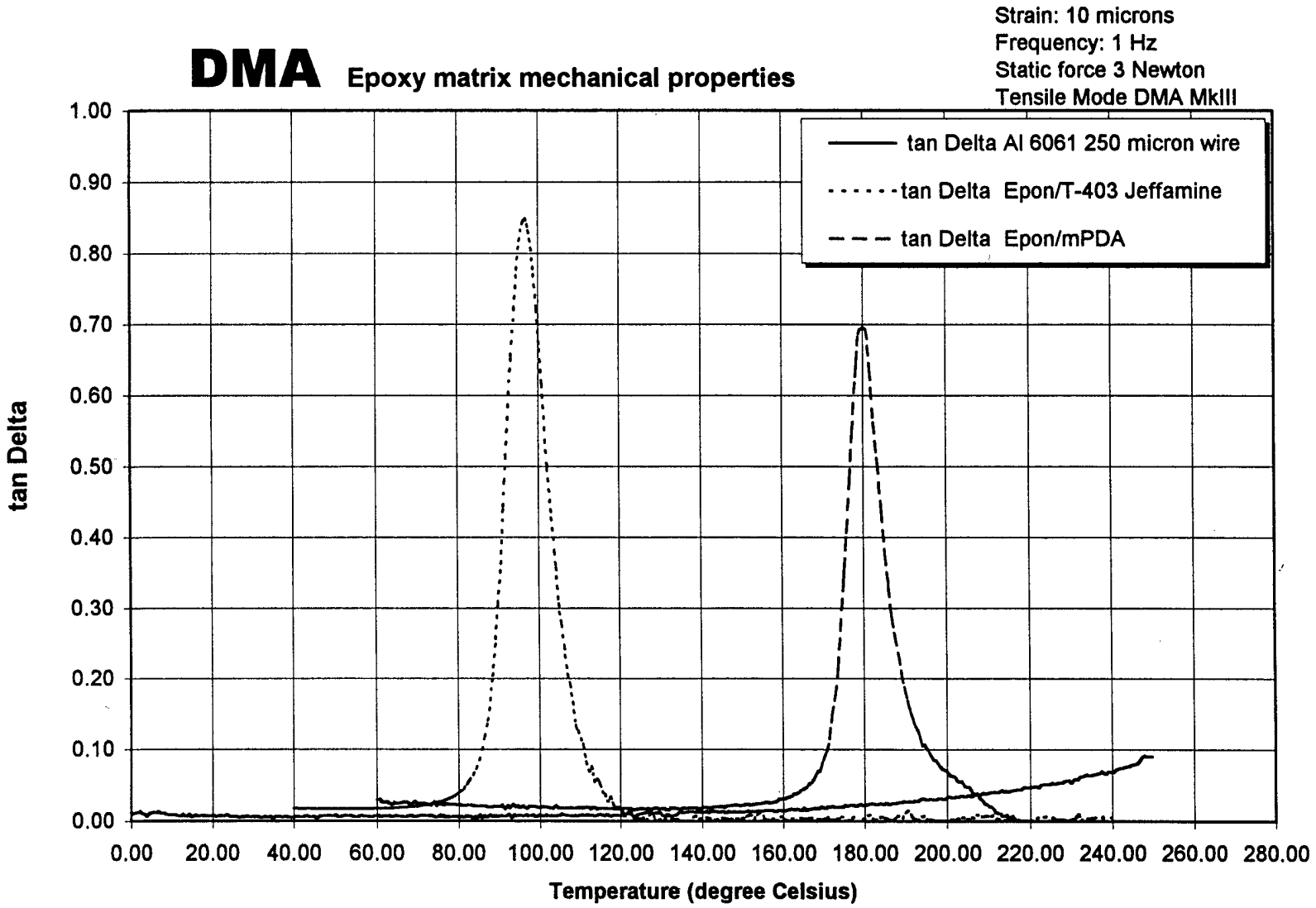

Figure 4.1.1. Epoxy matrix mechanical properties: tan Delta curve

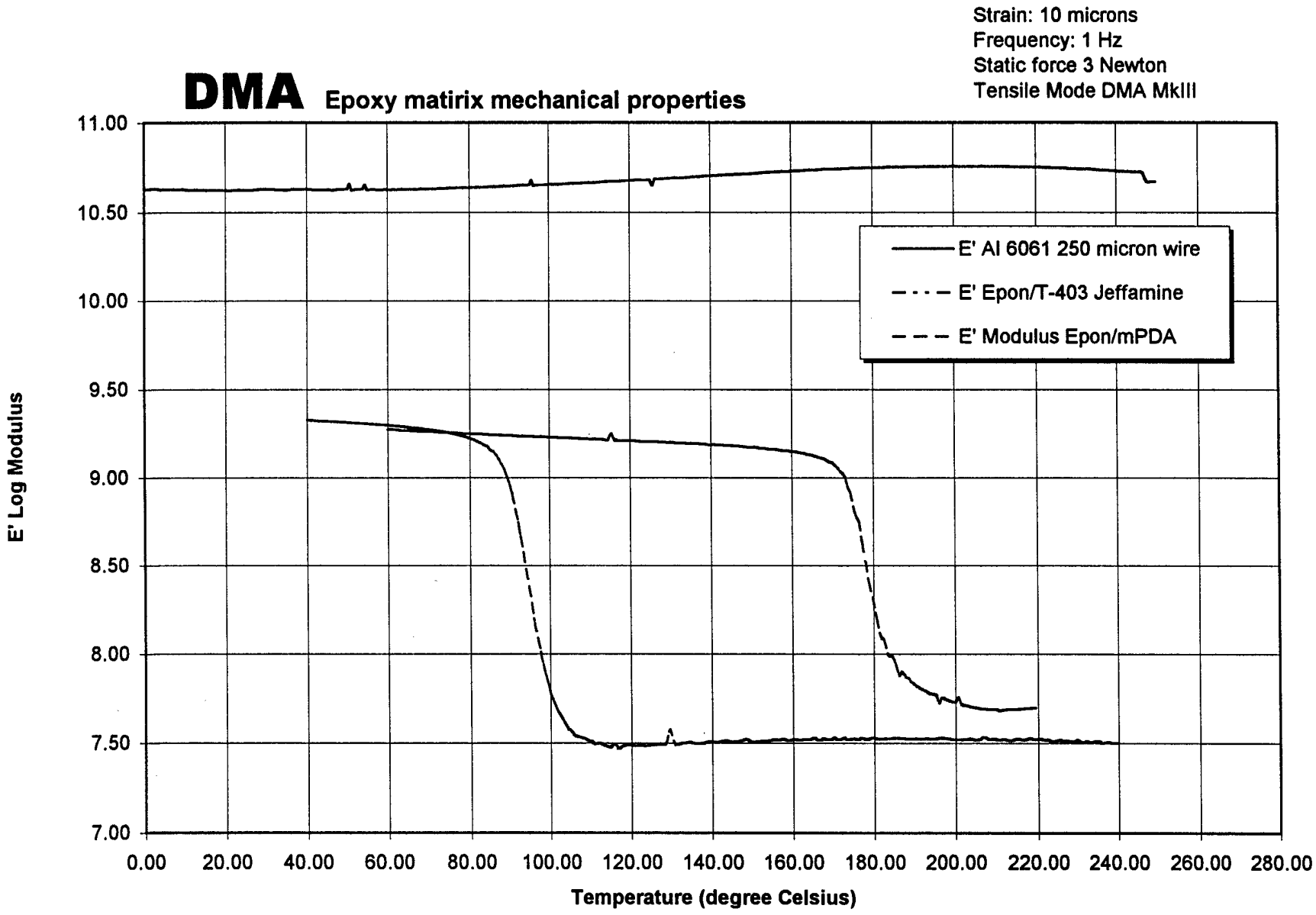

Figure 4.4.2 Epoxy matrix mechanical properties: E' curve

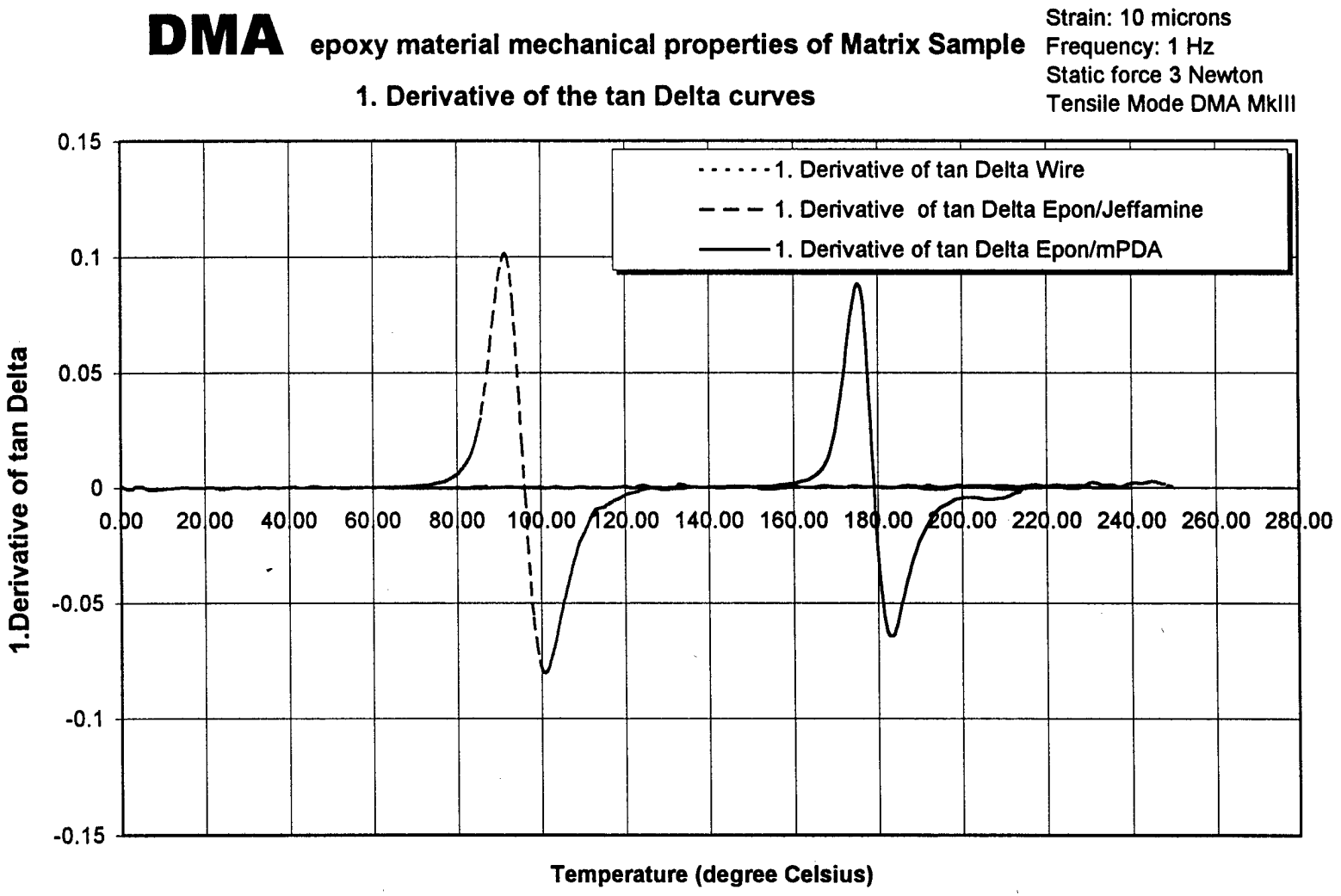

Figure 4.4.3. Epoxy matrix mechanical properties: first derivative of tan Delta

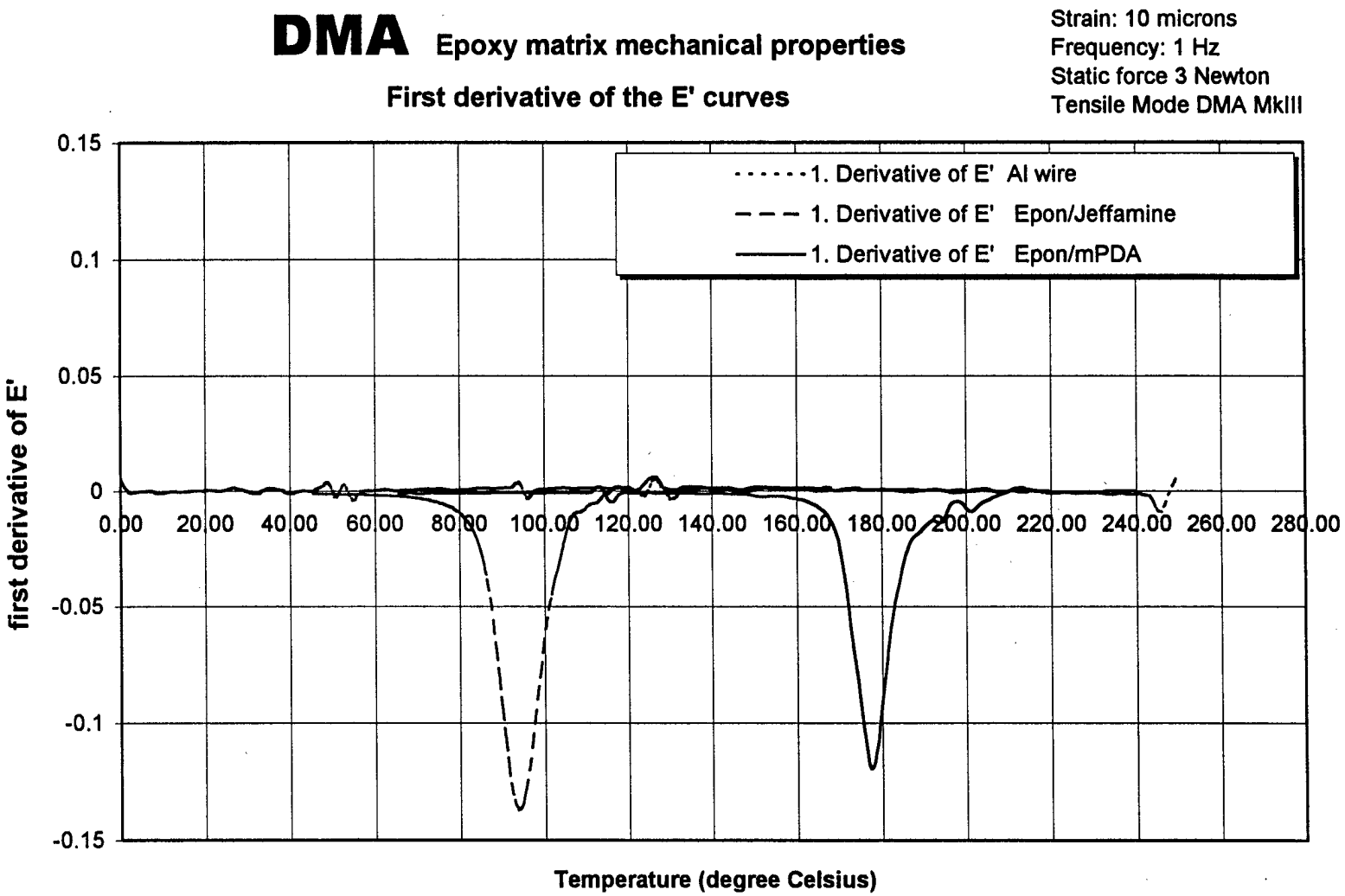

Figure 4.4.4. Epoxy matrix mechanical properties: first derivative of storage modulus

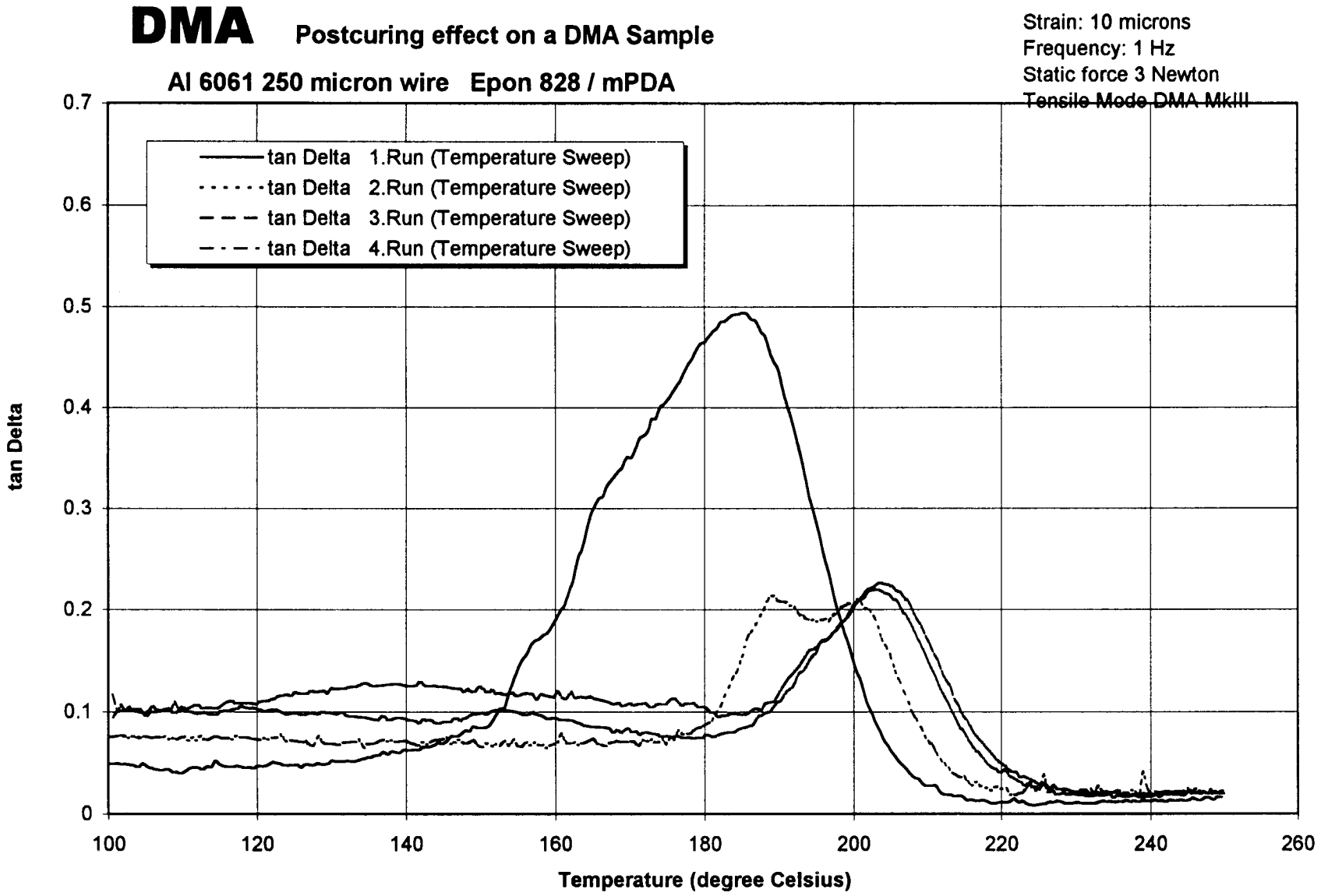

Figure 4.4.5. Postcuring effect on a DMA Sample

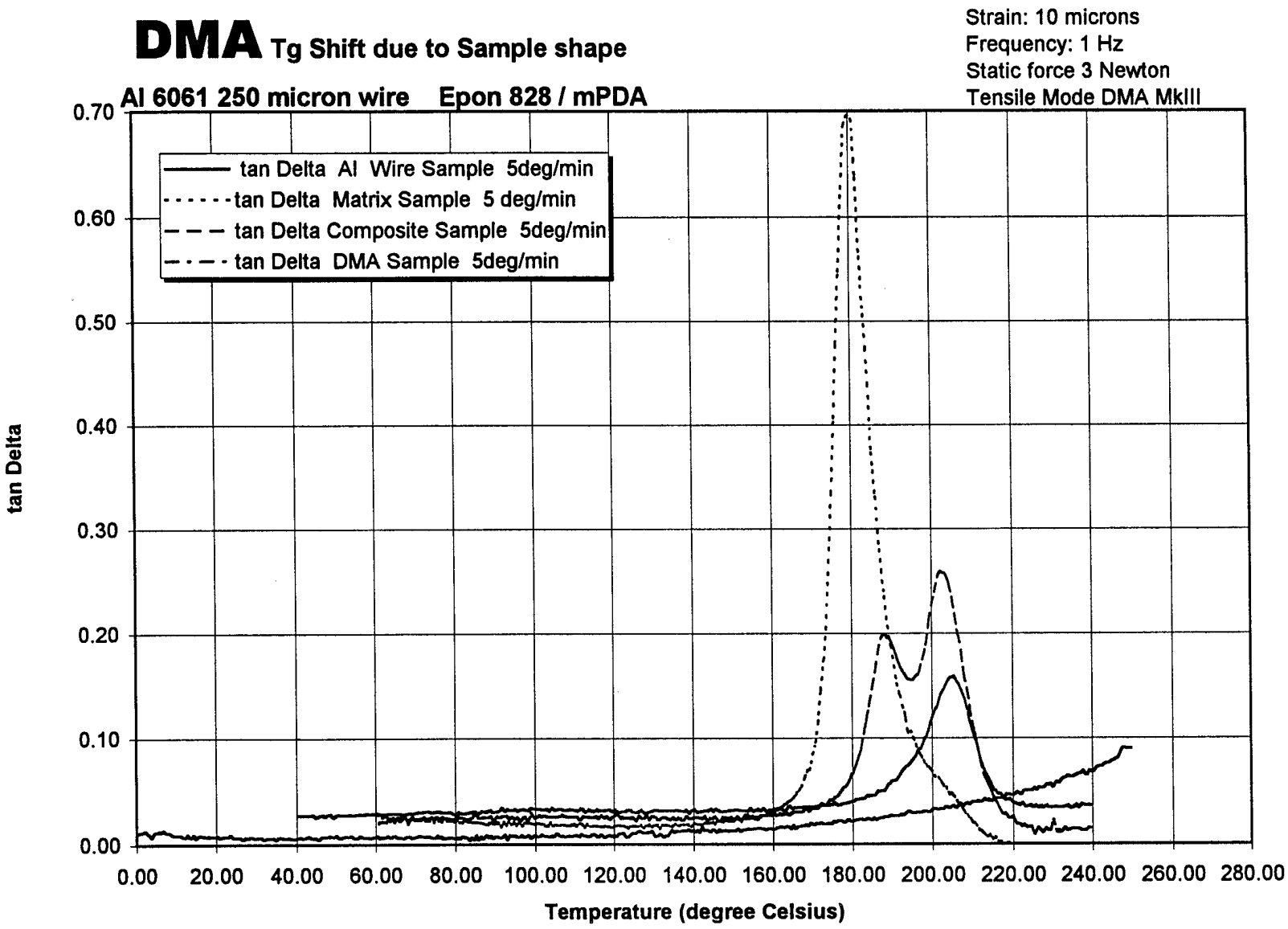

Figure 4.4.6. Tg Shift due to Sample shape

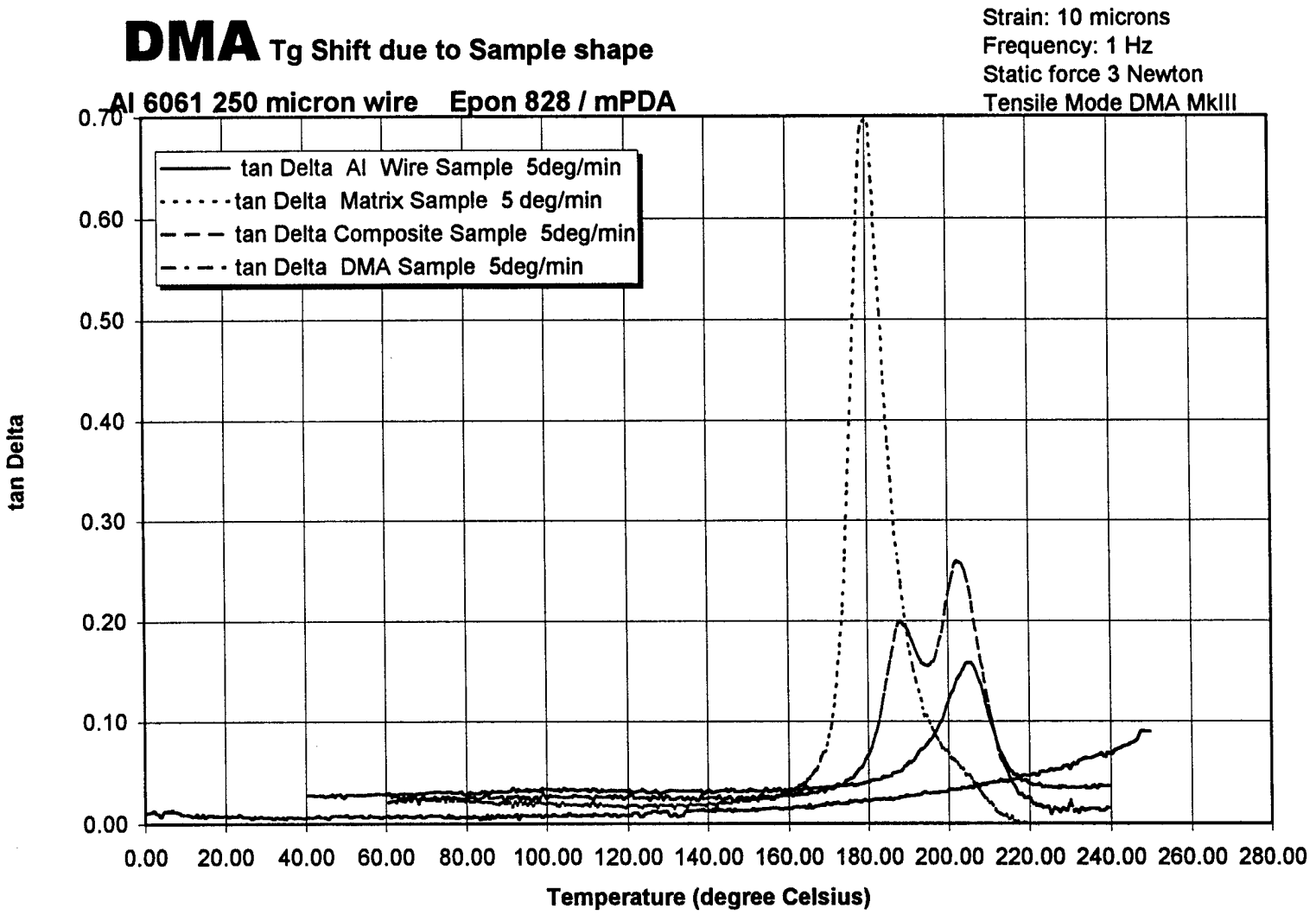

Figure 4.4.7. Tg Shift due to Sample shape

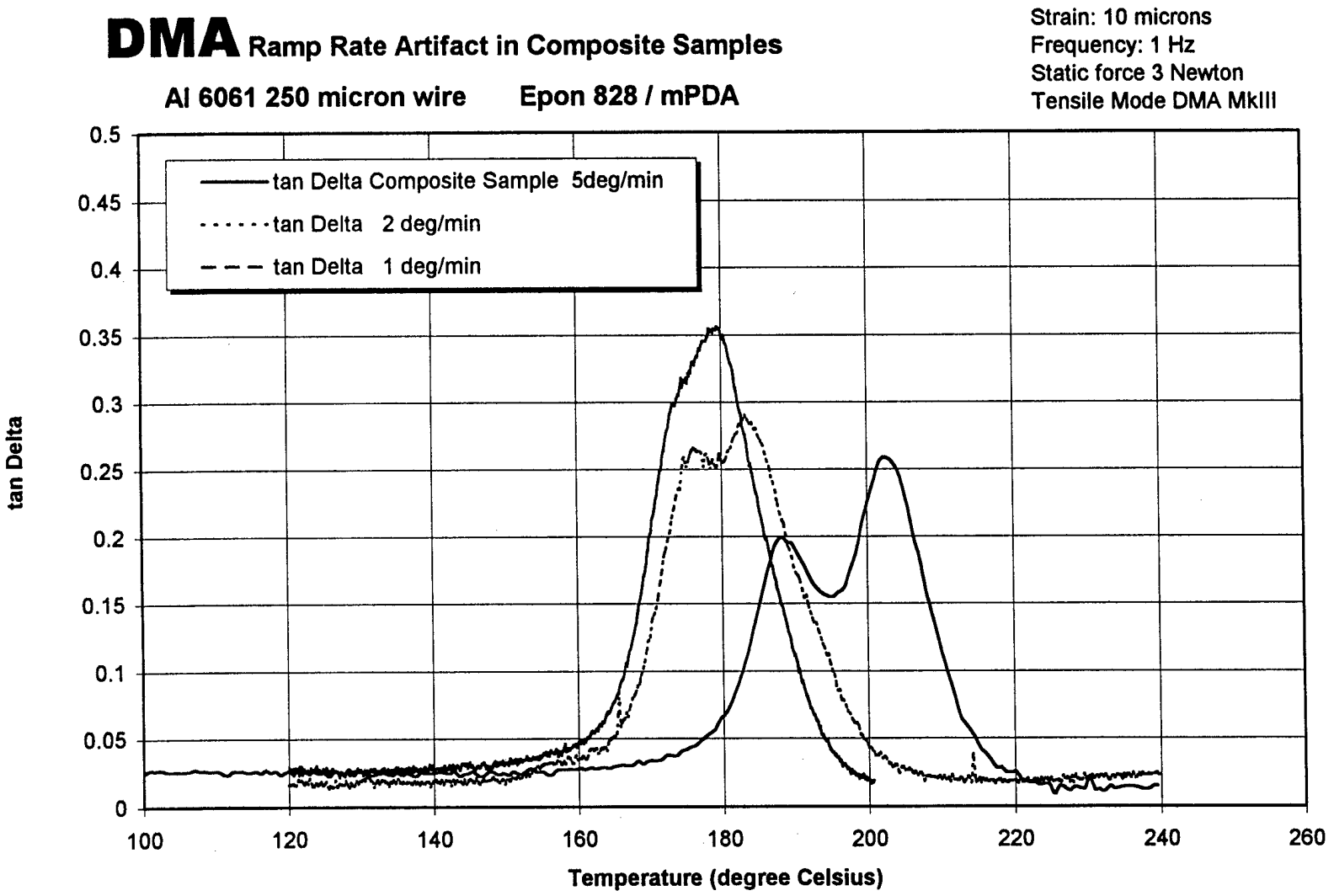

Figure 4.4.8. Ramp Rate Artifact in Composite Samples

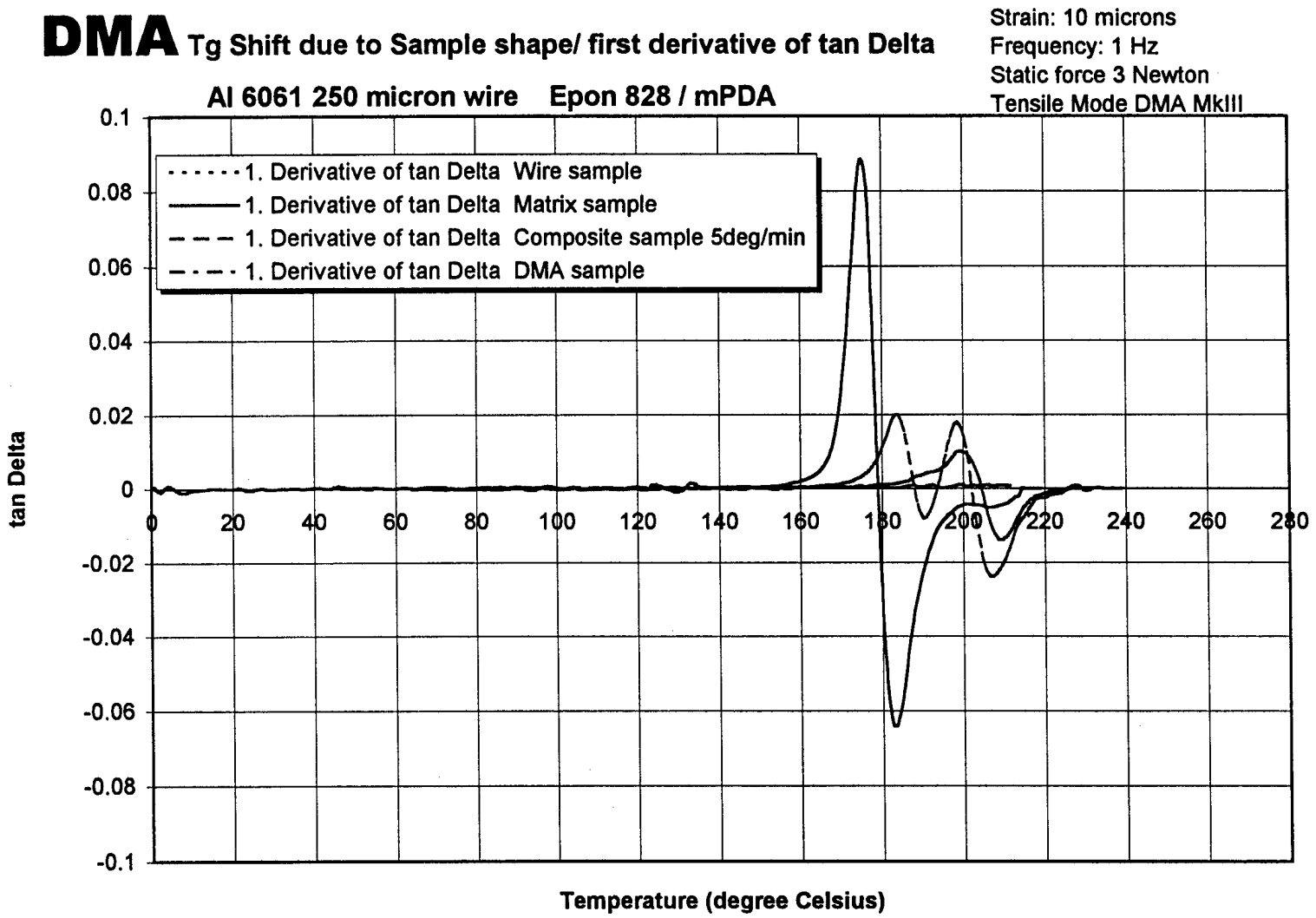

Figure 4.4.9. Sample shape effect: first derivative of tan Delta

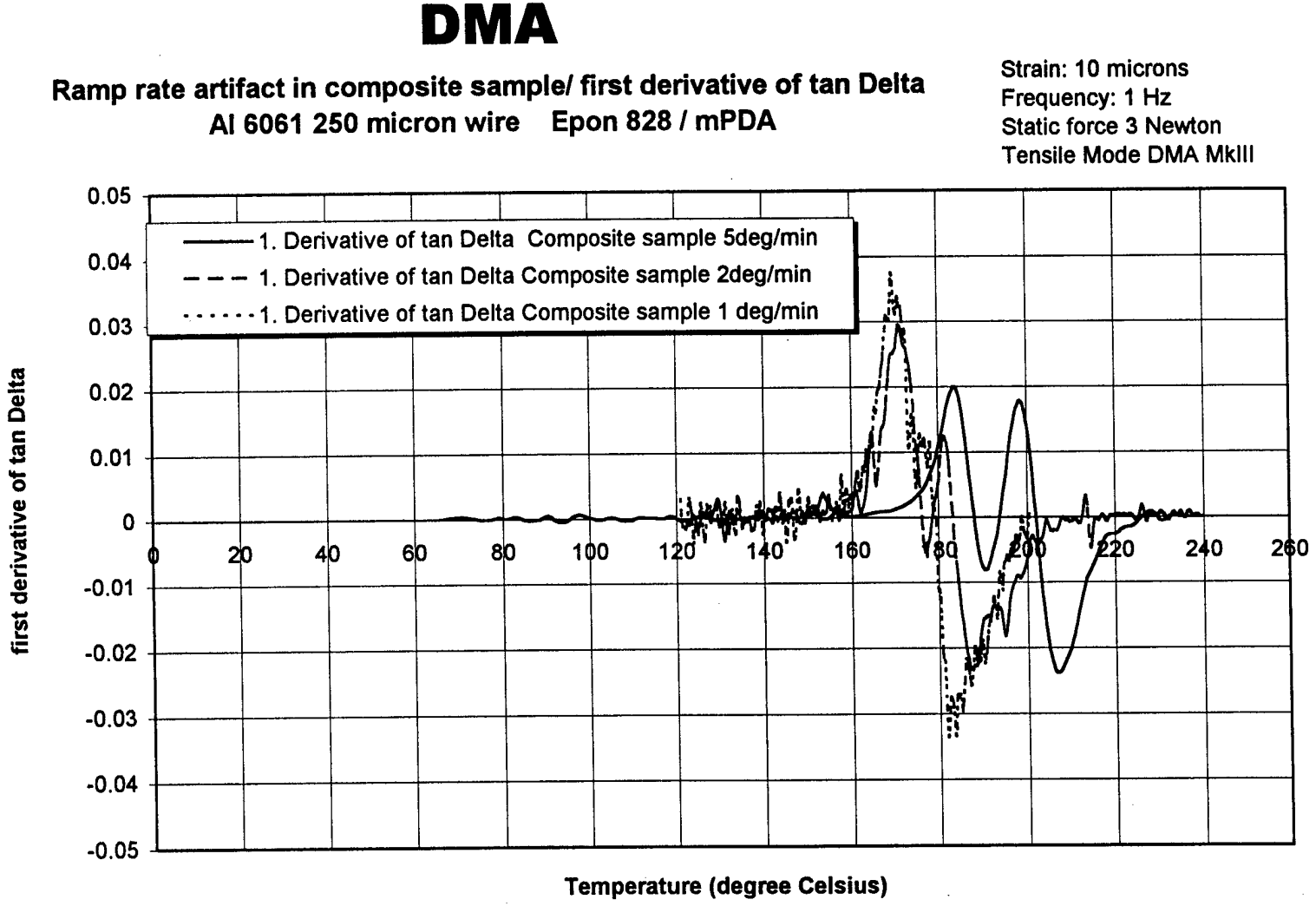

Figure 4.4.10. Ramp artifact in composite samples: first derivative of tan Delta

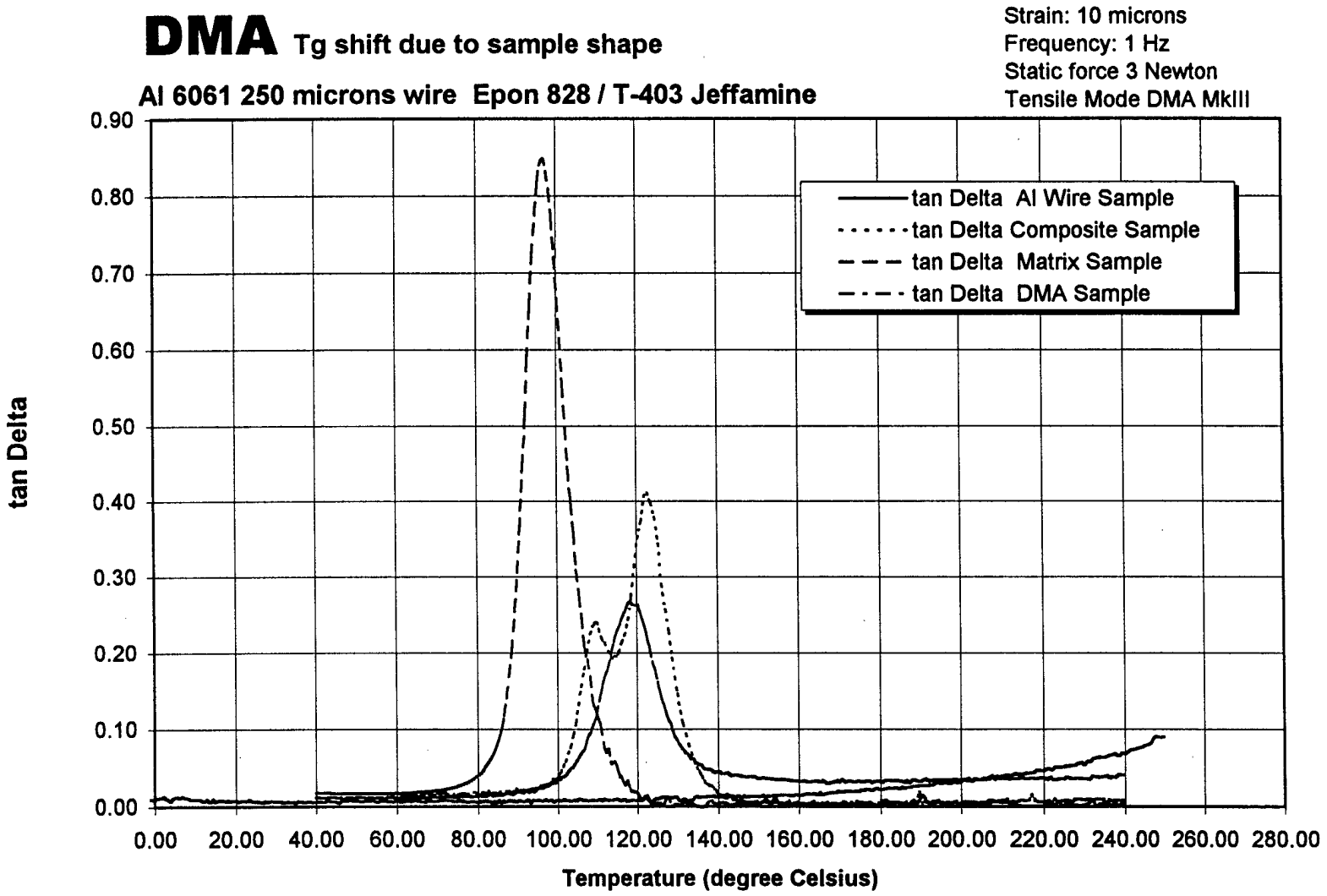

Figure 4.4.11. Tg shift due to sample shape

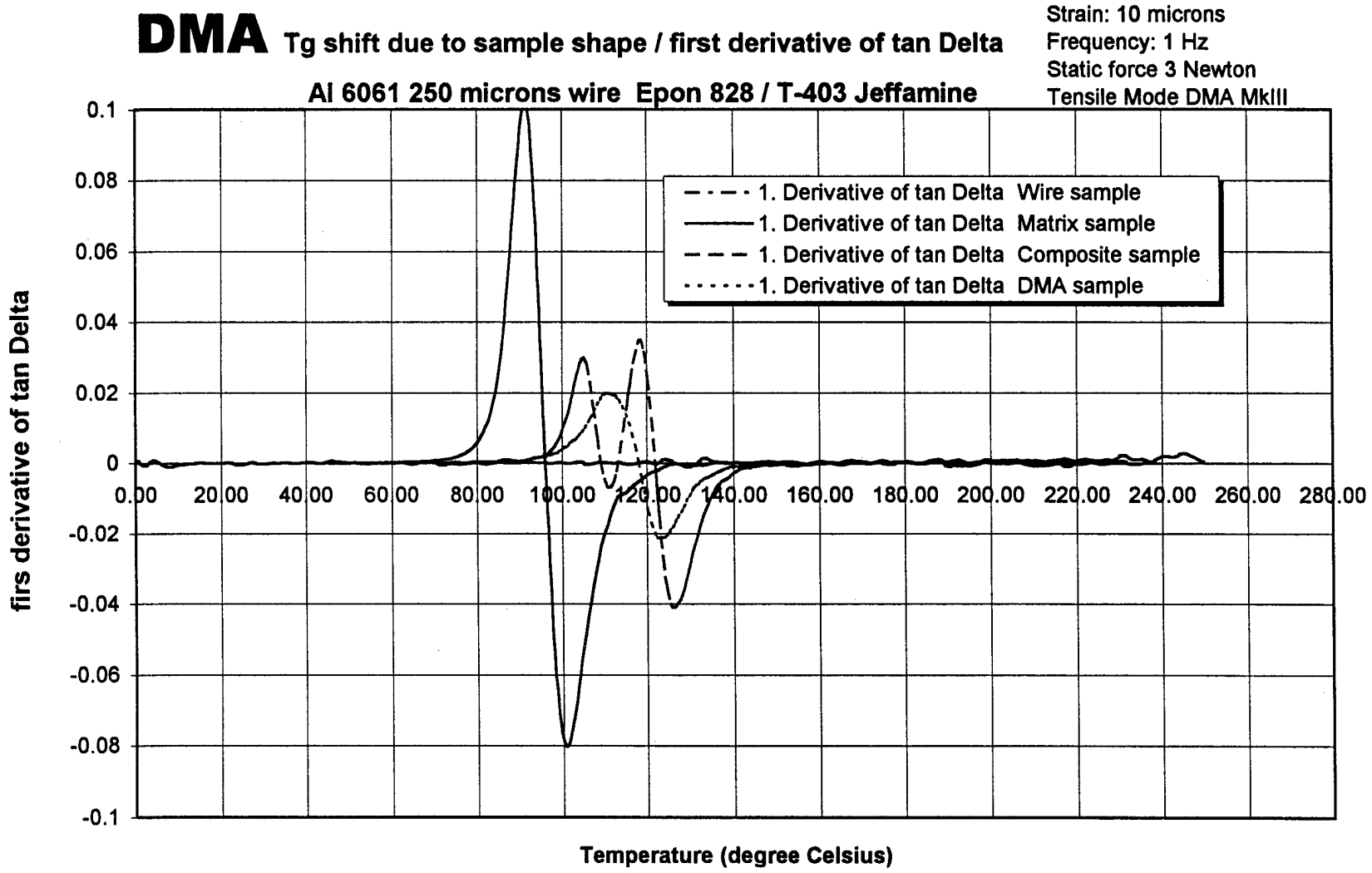

Figure 4.4.12. Sample shape effect Epon: first derivative of tan Delta

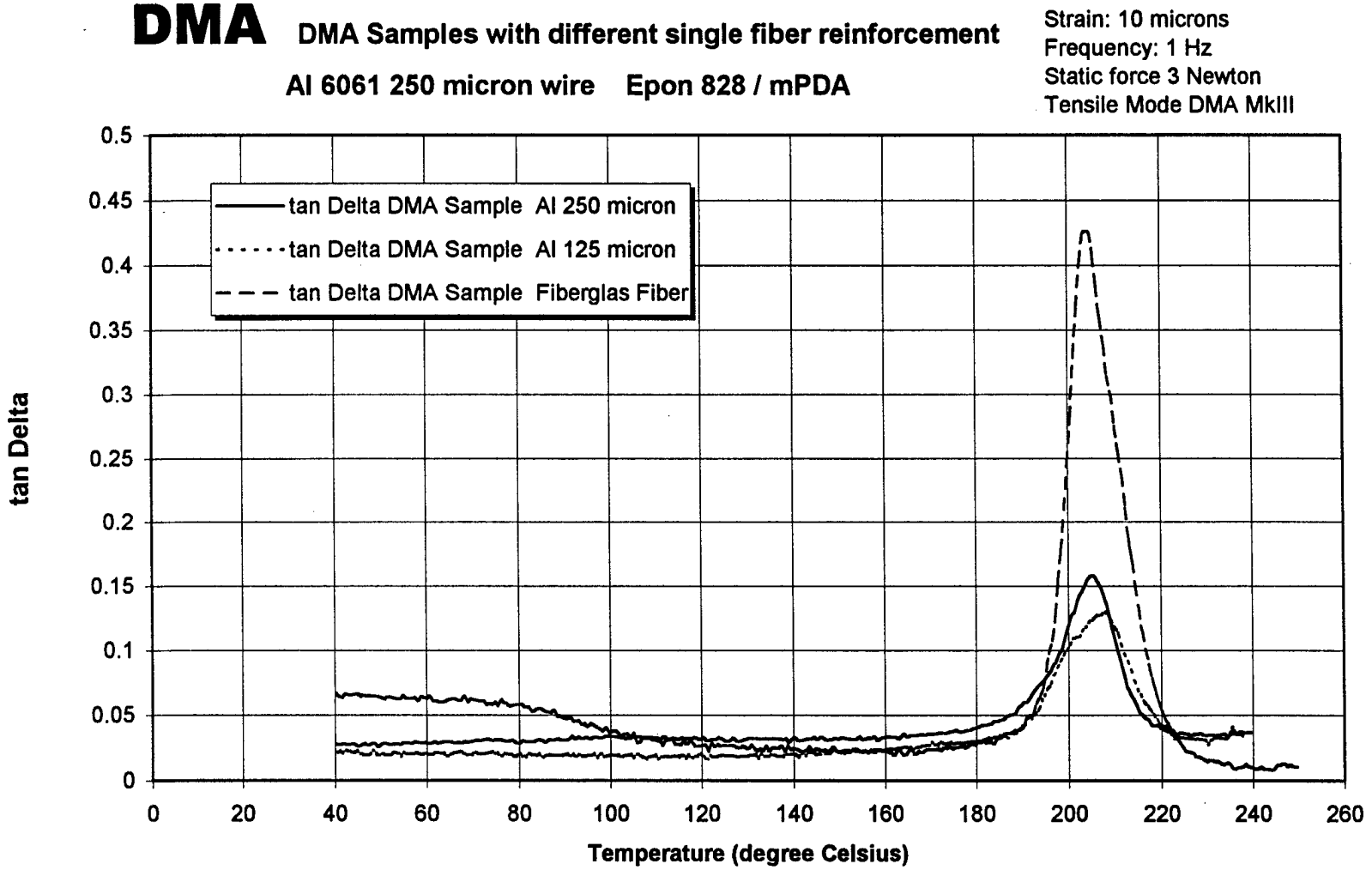

Figure 4.4.13. DMA Samples with different single fiber reinforcement

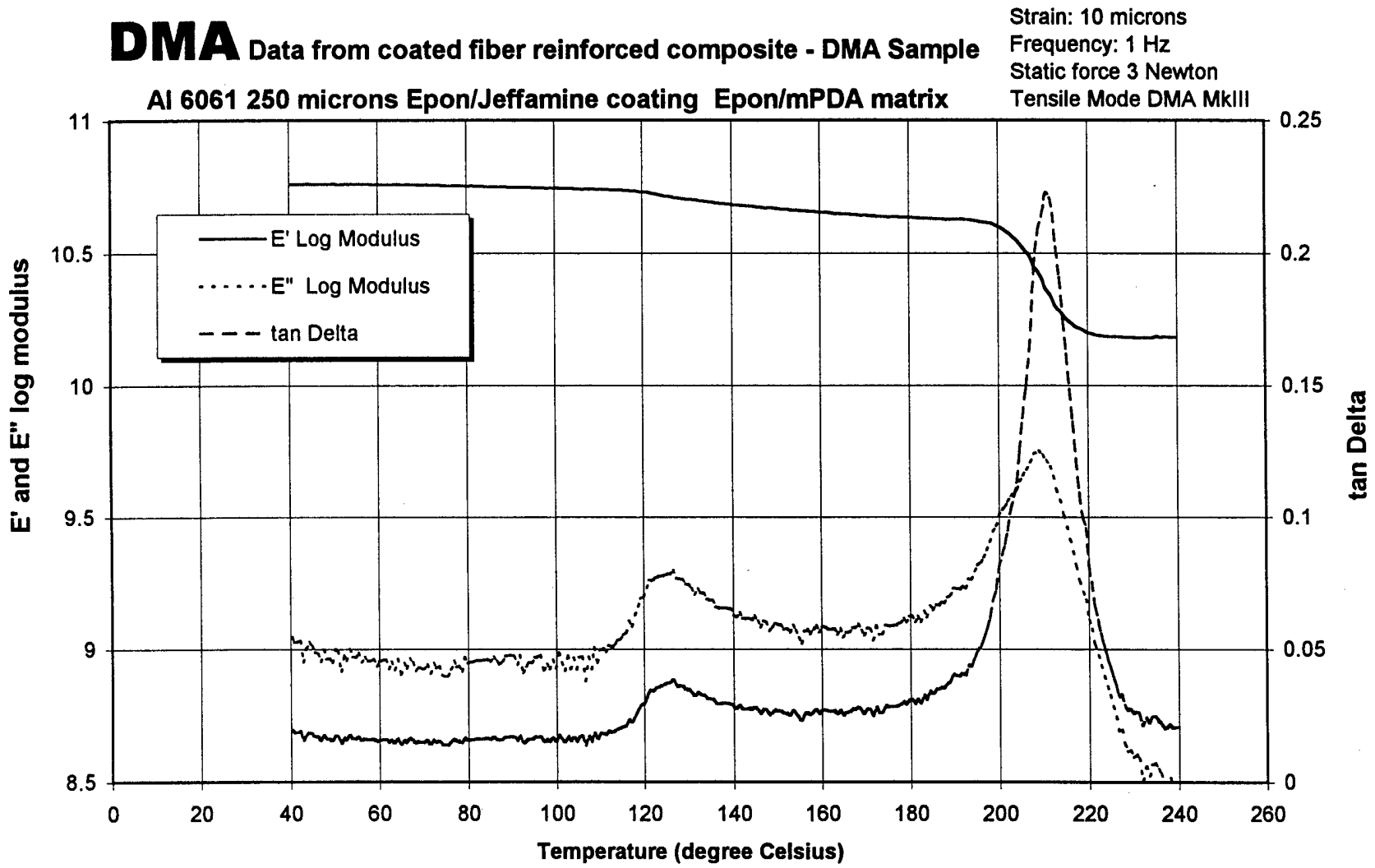

Figure 4.4.14 DMA data from coated fiber reinforced composite

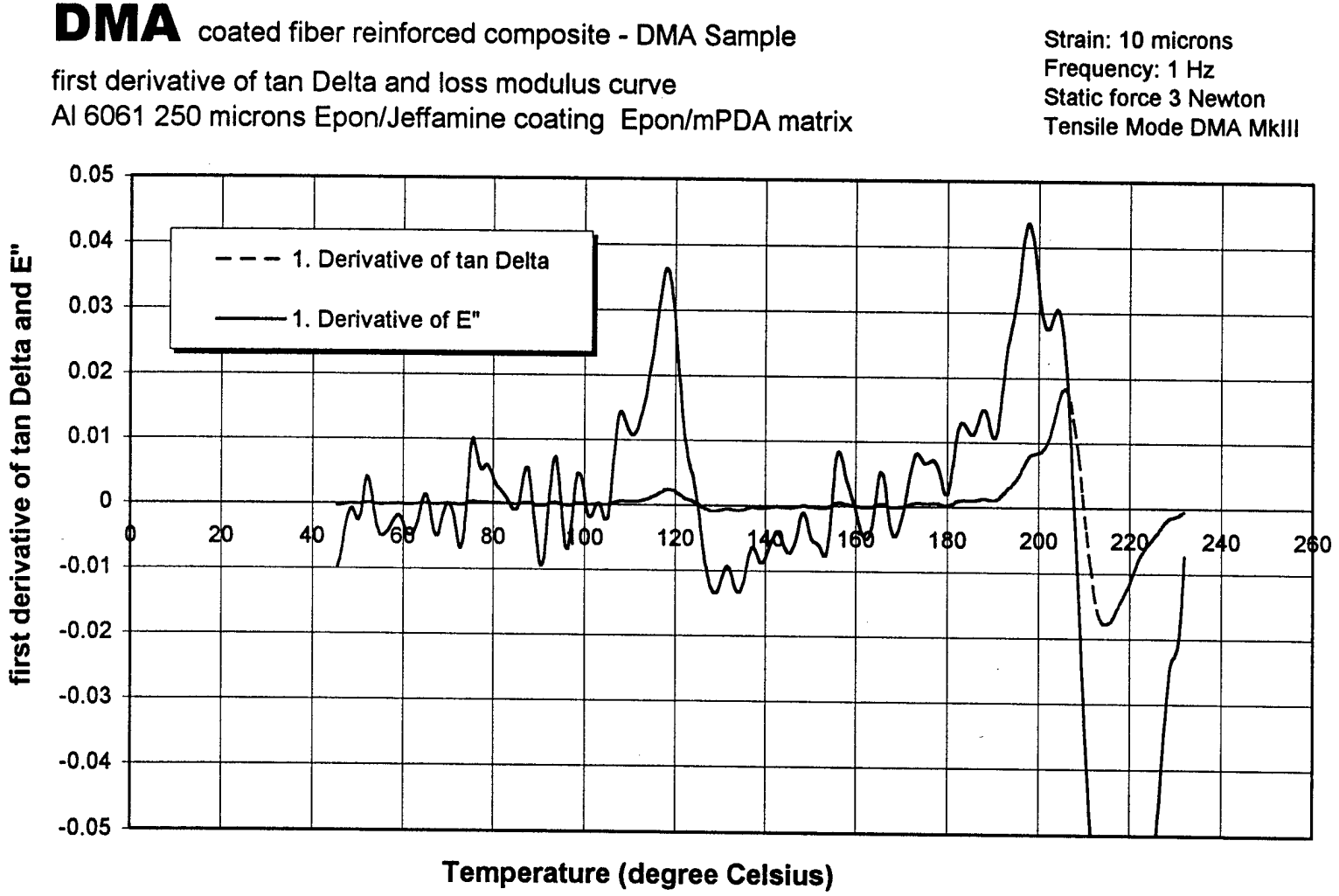

Figure 4.4.15. Coated DMA sample: first derivative of tan Delta and E"curve

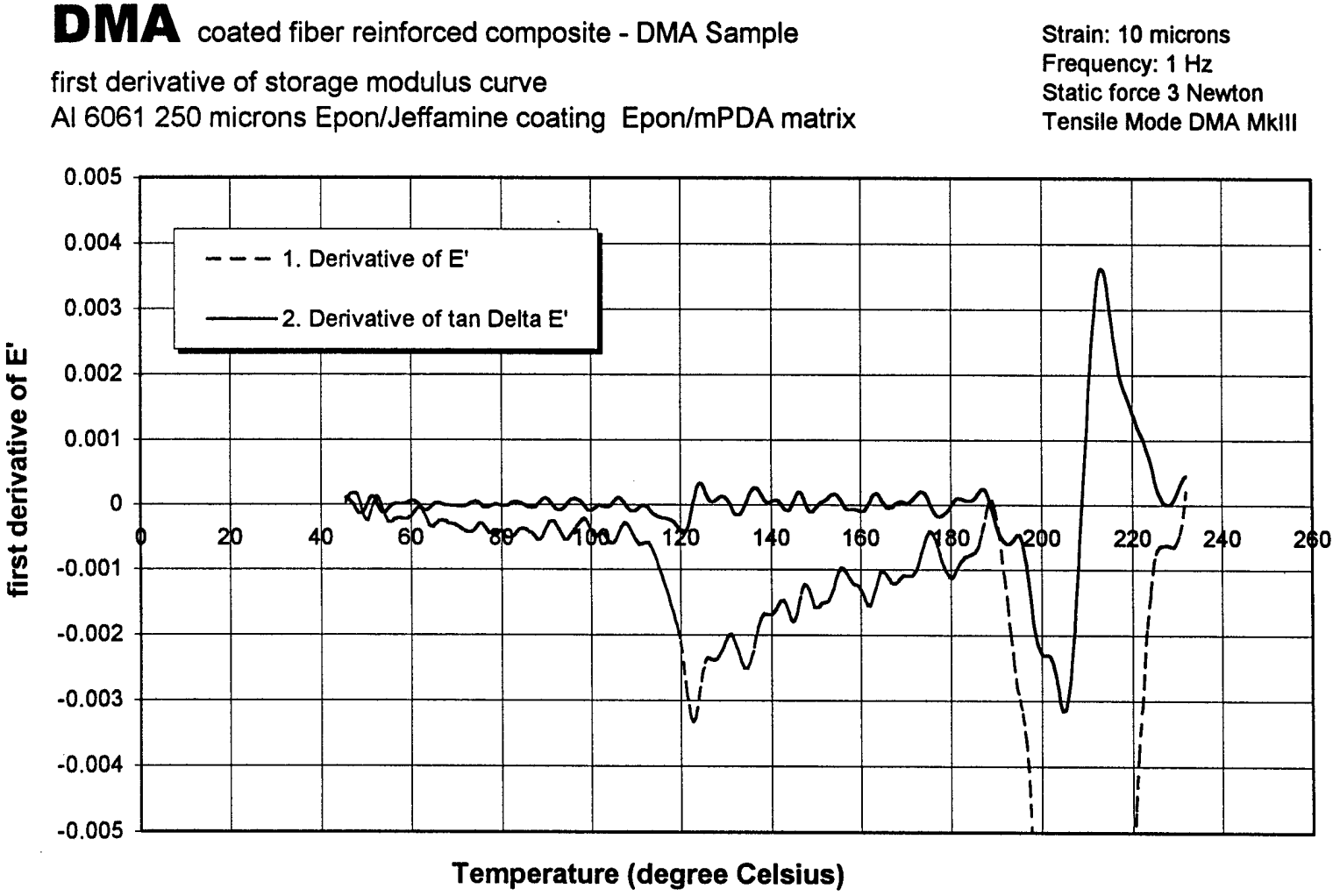

Figure 4.4.16. First derivative of storage modulus of the coated fiber DMA sample

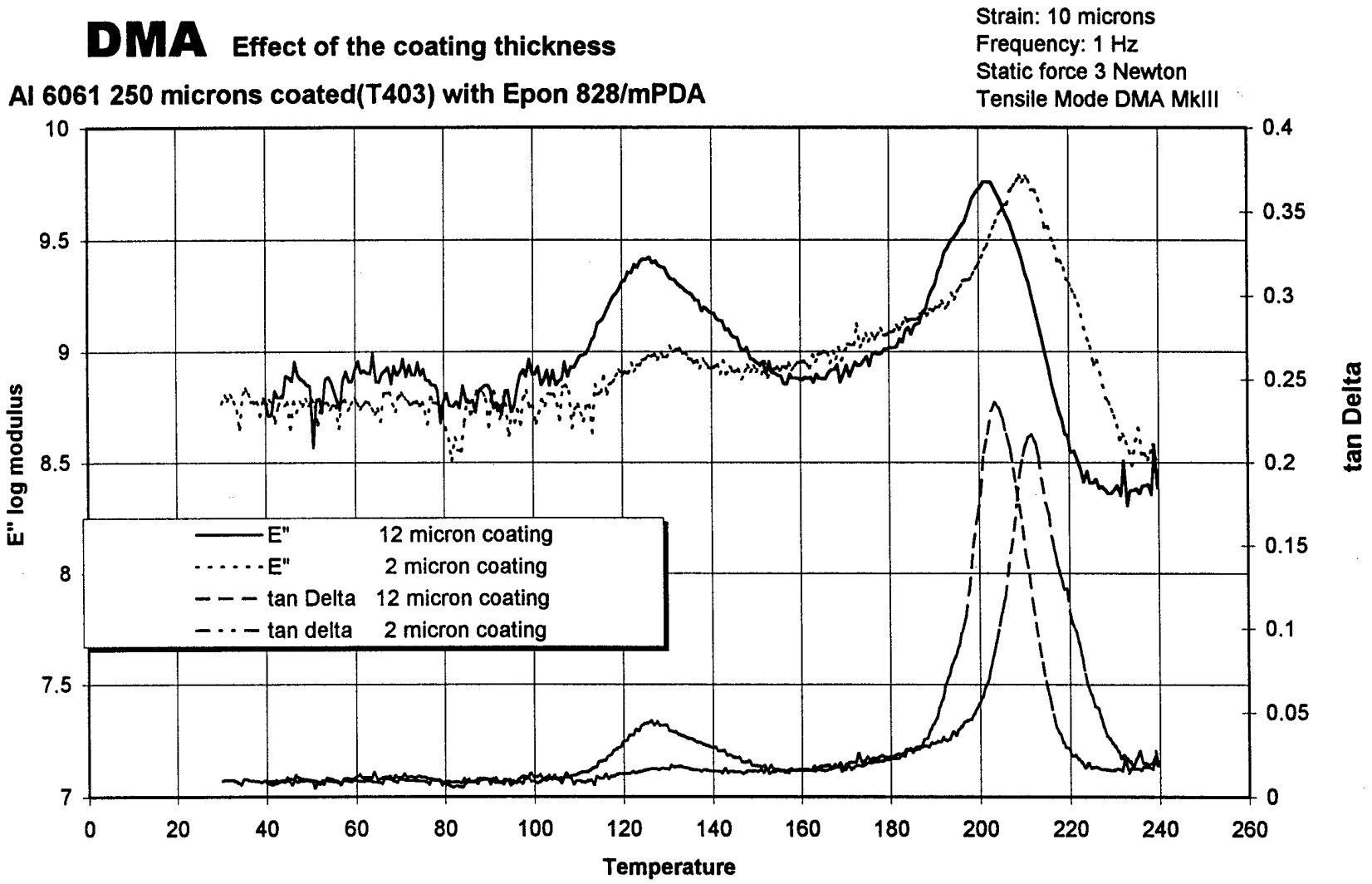

Figure 4.4.17. Effect of the coating thickness

ESEM pictures of a Epon/T-403 coated Aluminium6061 wire

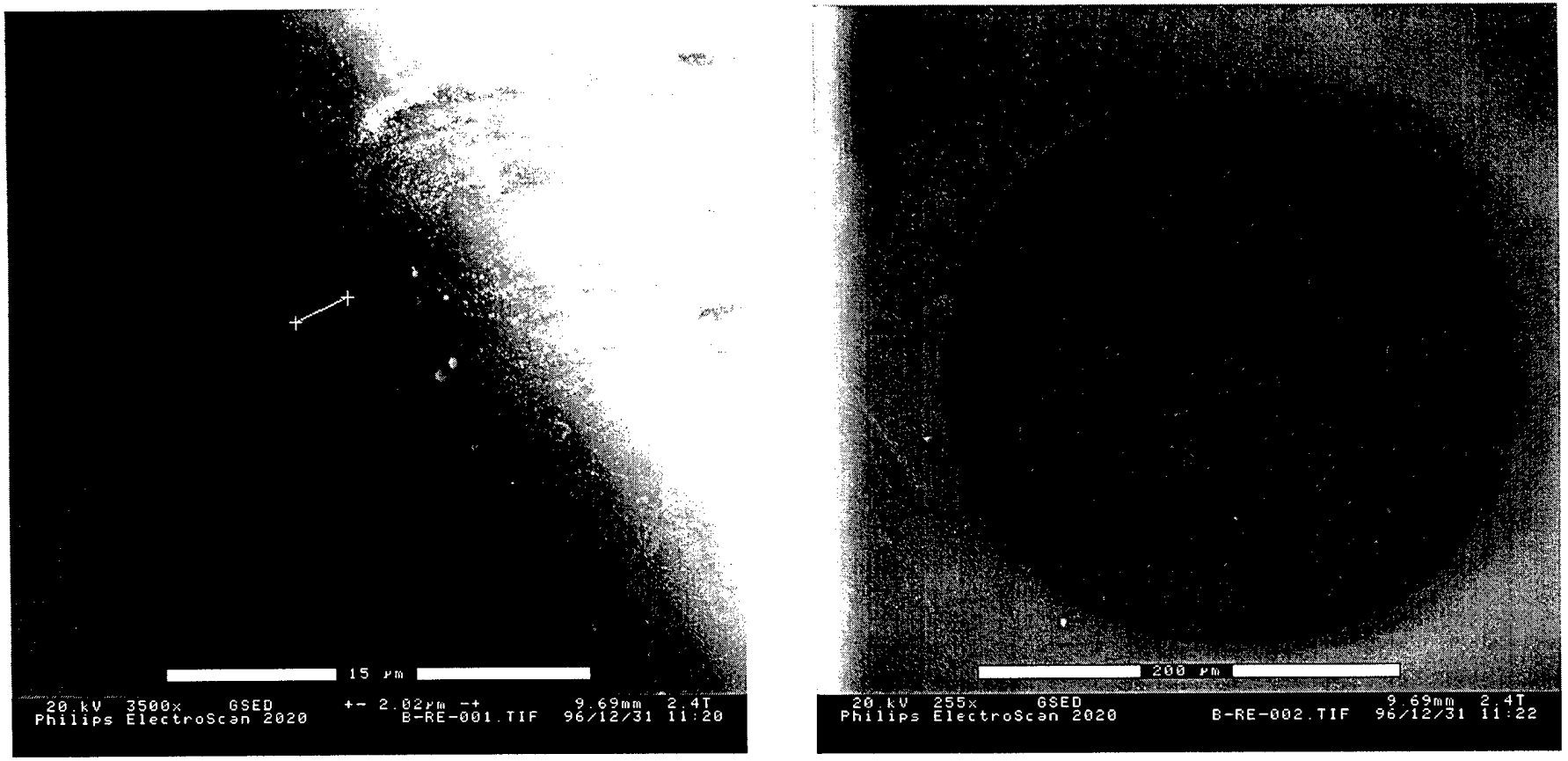

Figure 4.4.18. ESEM picture of the 2 micron coating

ESEM pictures of a Epon/T-403 coated Aluminium6061 wire

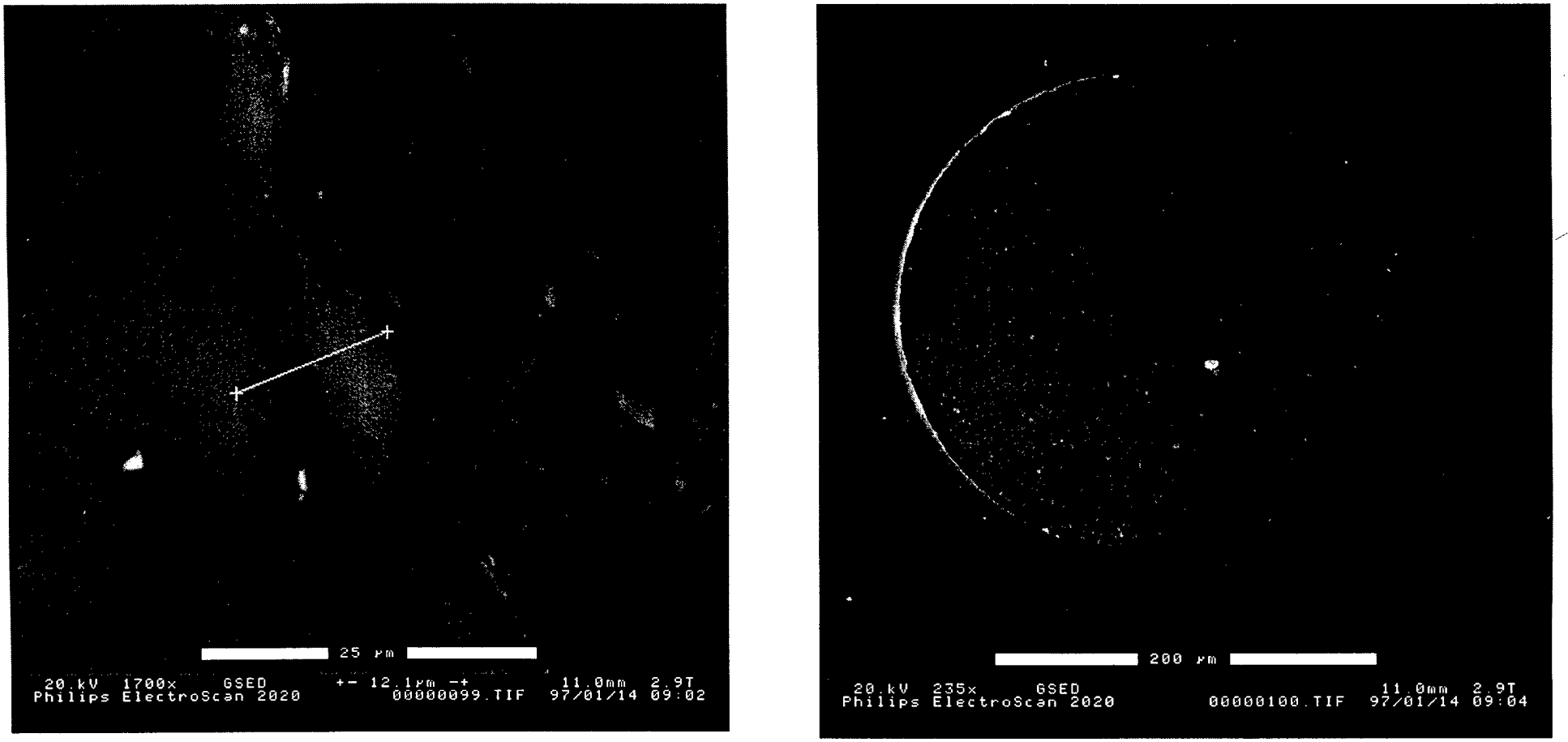

Figure 4.4.19. SEM picture of the 12 micron coating

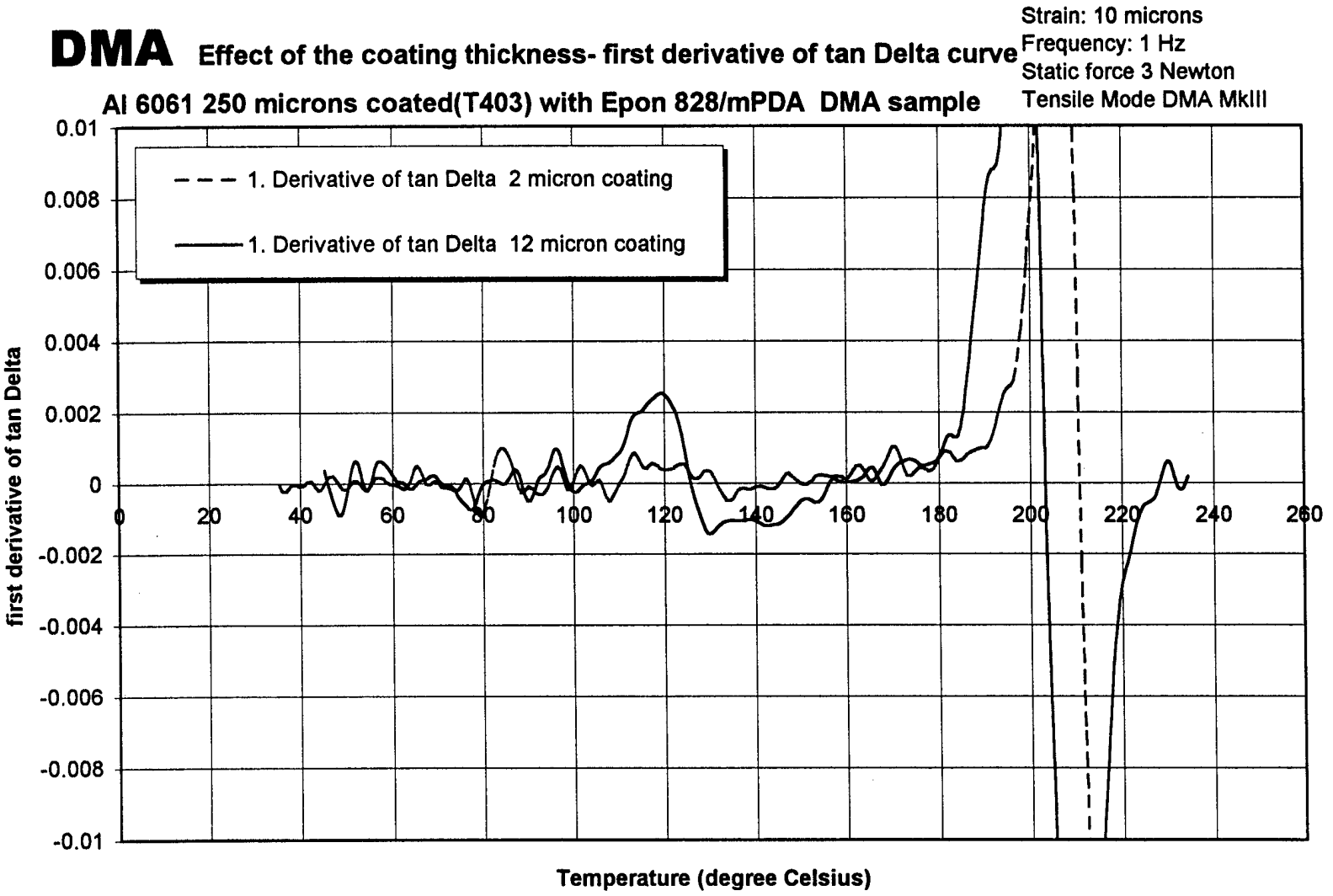

Figure 4.4.20. Effect of coating thickness: first derivative of tan Delta

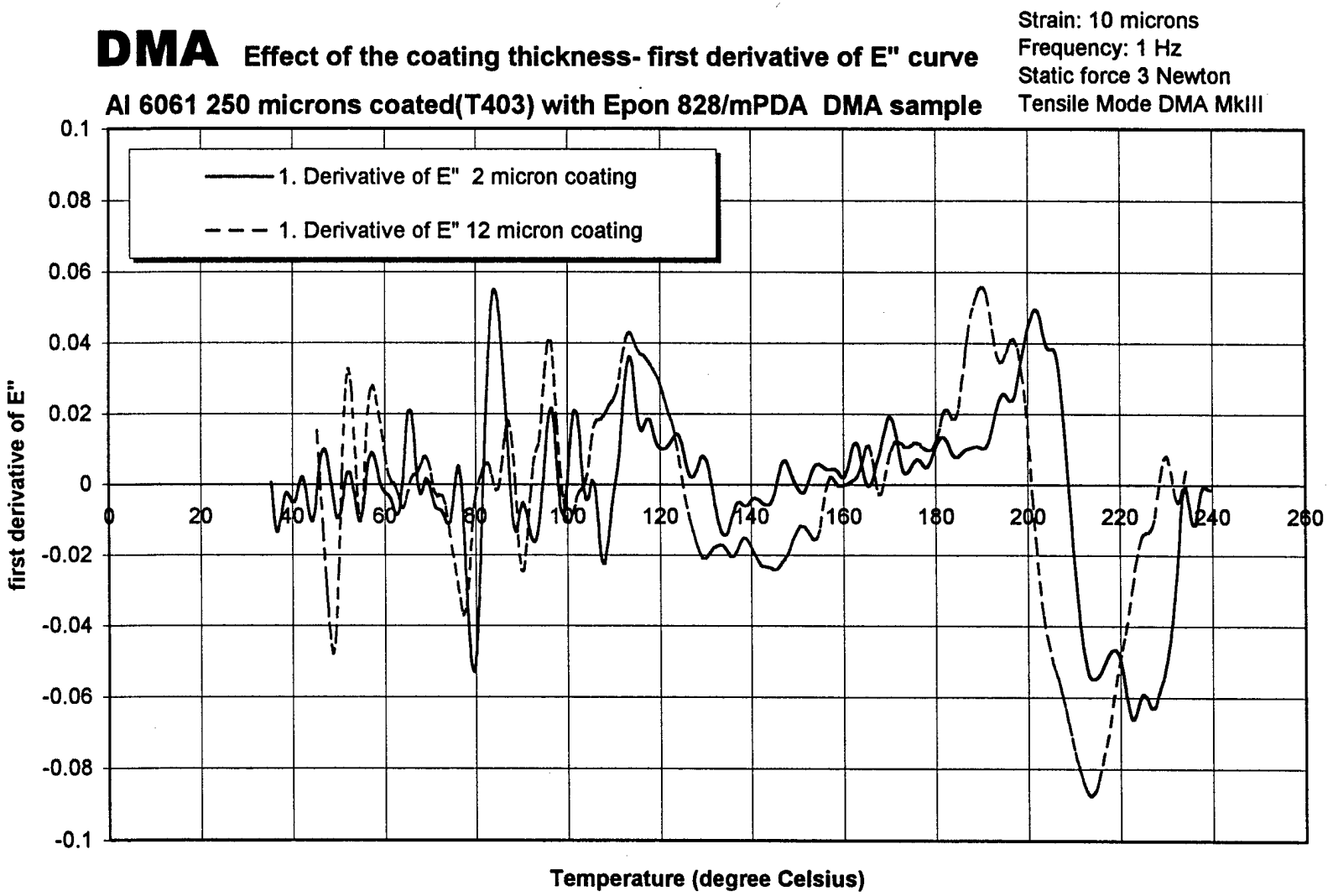

Figure 4.4.21. Effect of the coating thickness: first derivative of the loss modulus

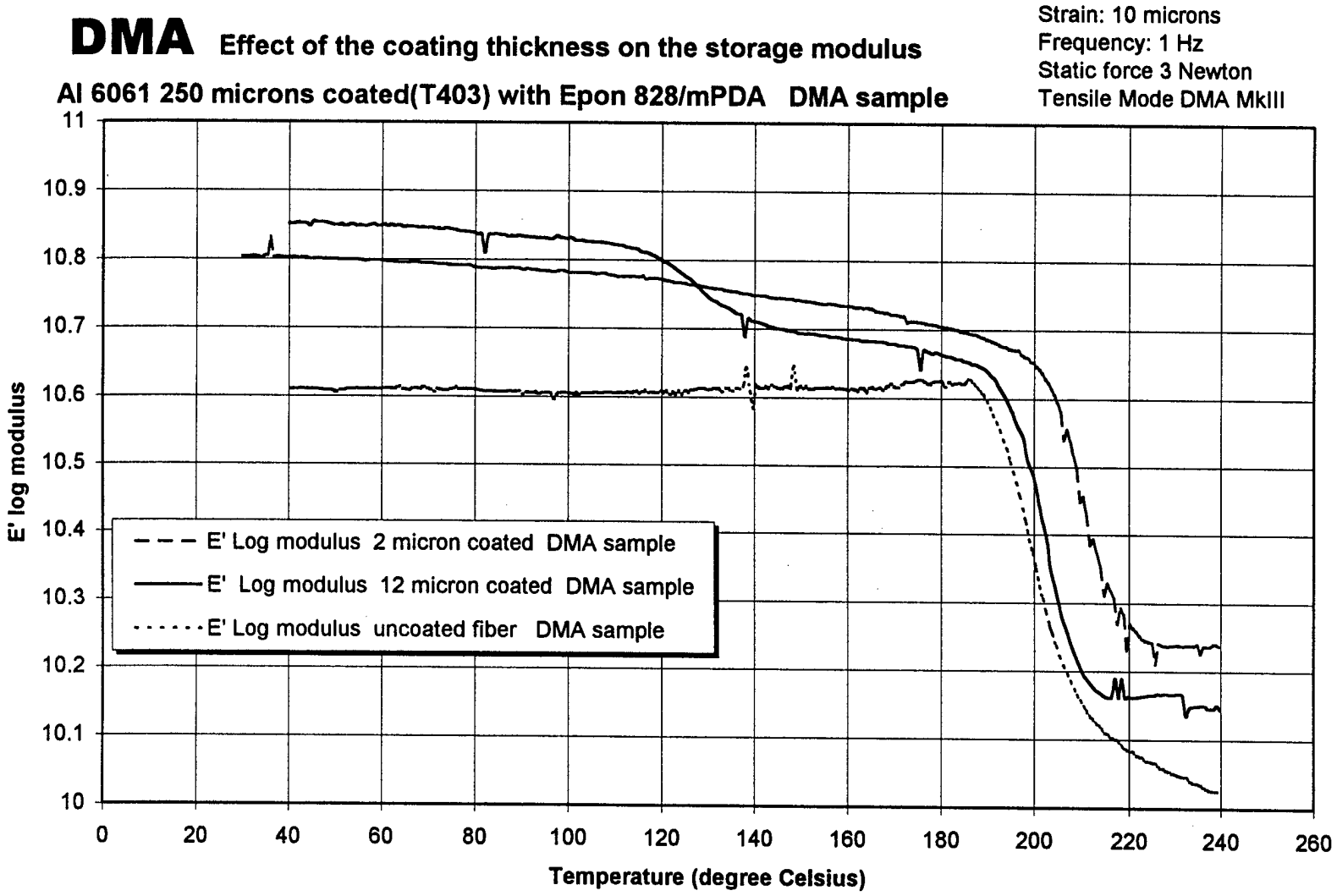

Figure 4.4.22. Effect of coating thickness on the storage modulus

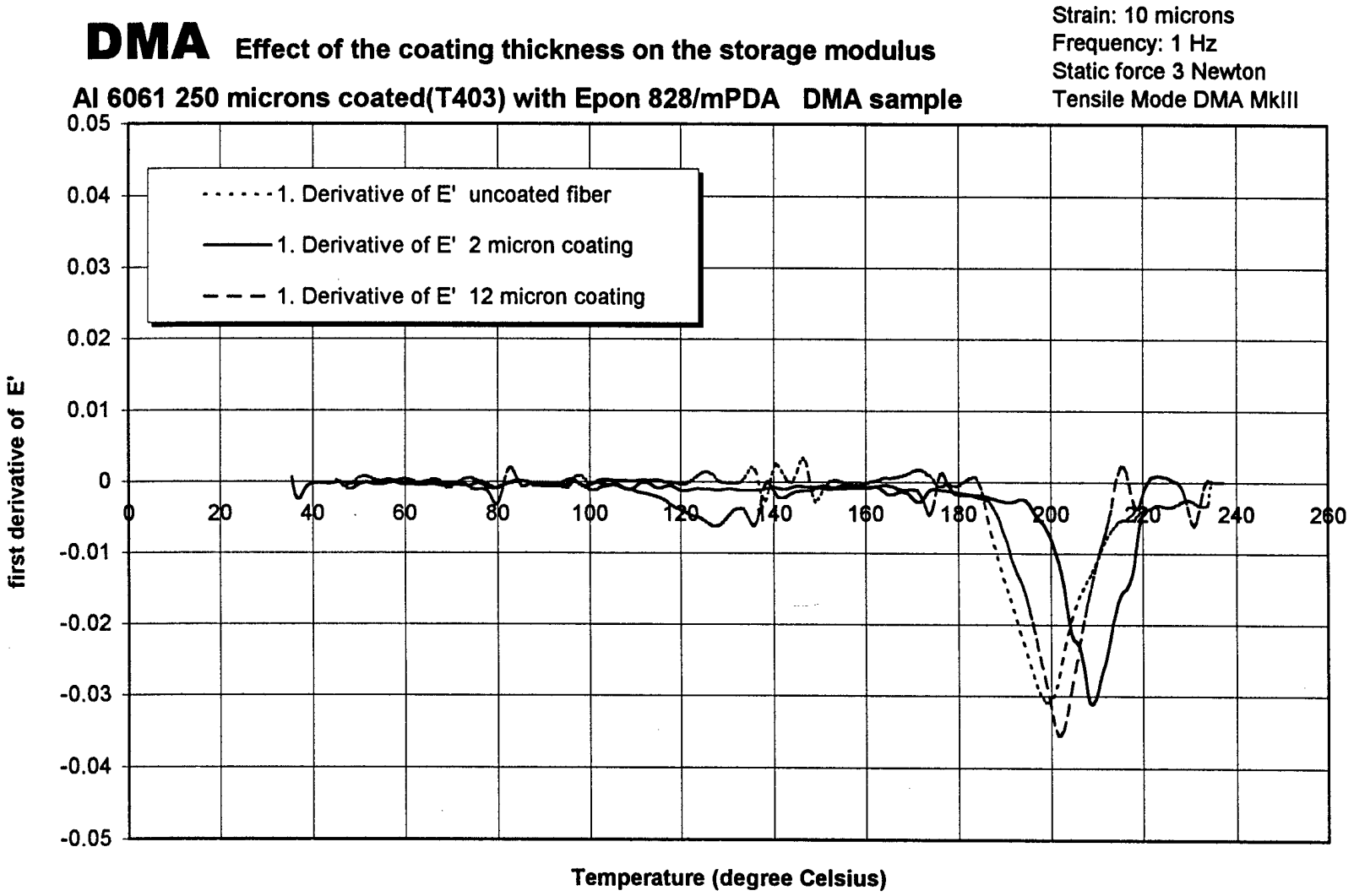

Figure 4.4.23. Effect of coating thickness: first derivative of storage modulus

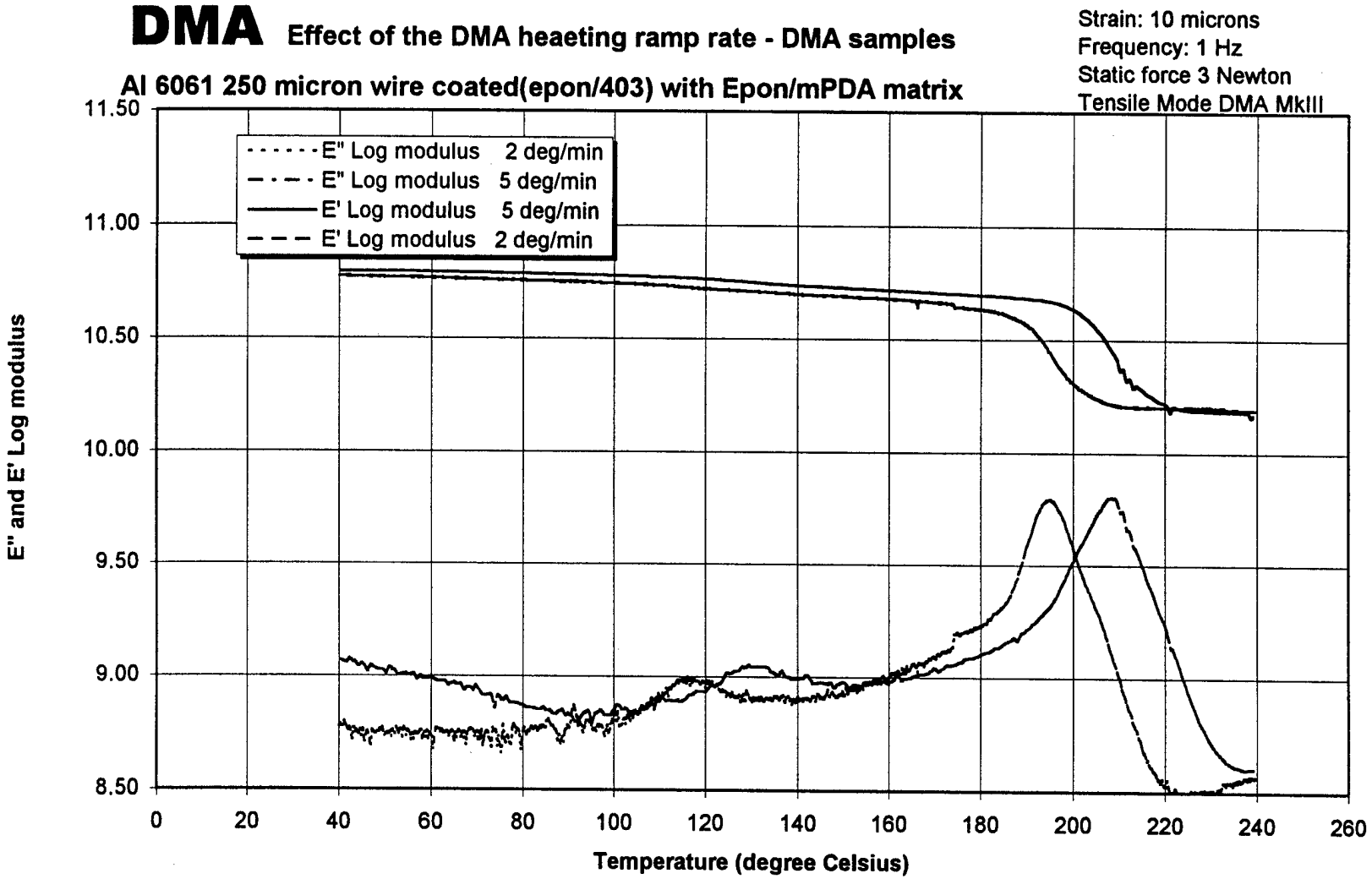

Figure 4.4.24. Effect of the heating rate on E' and E"

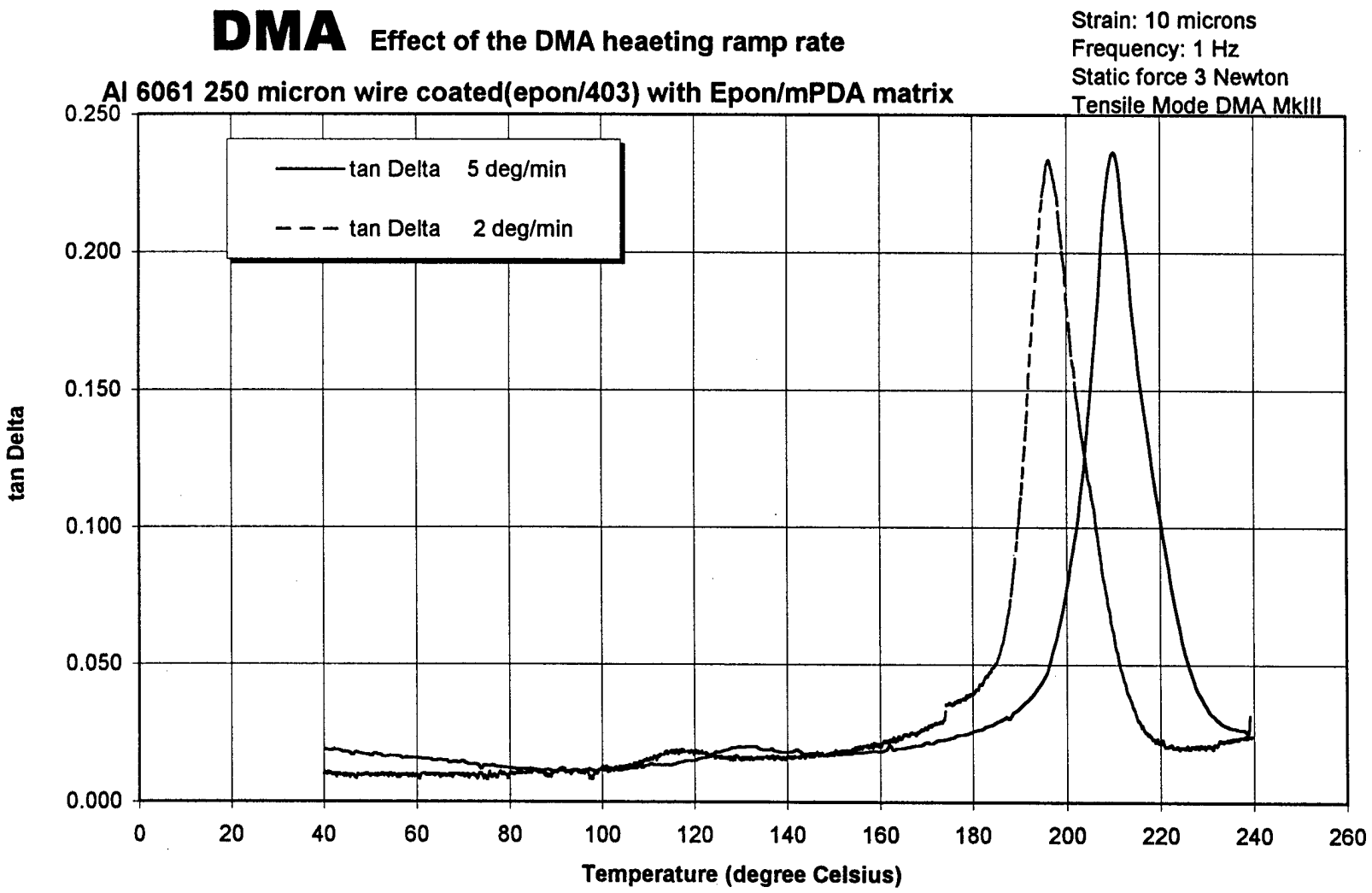

Figure 4.4.25. Effect of the heating rate on tan Delta

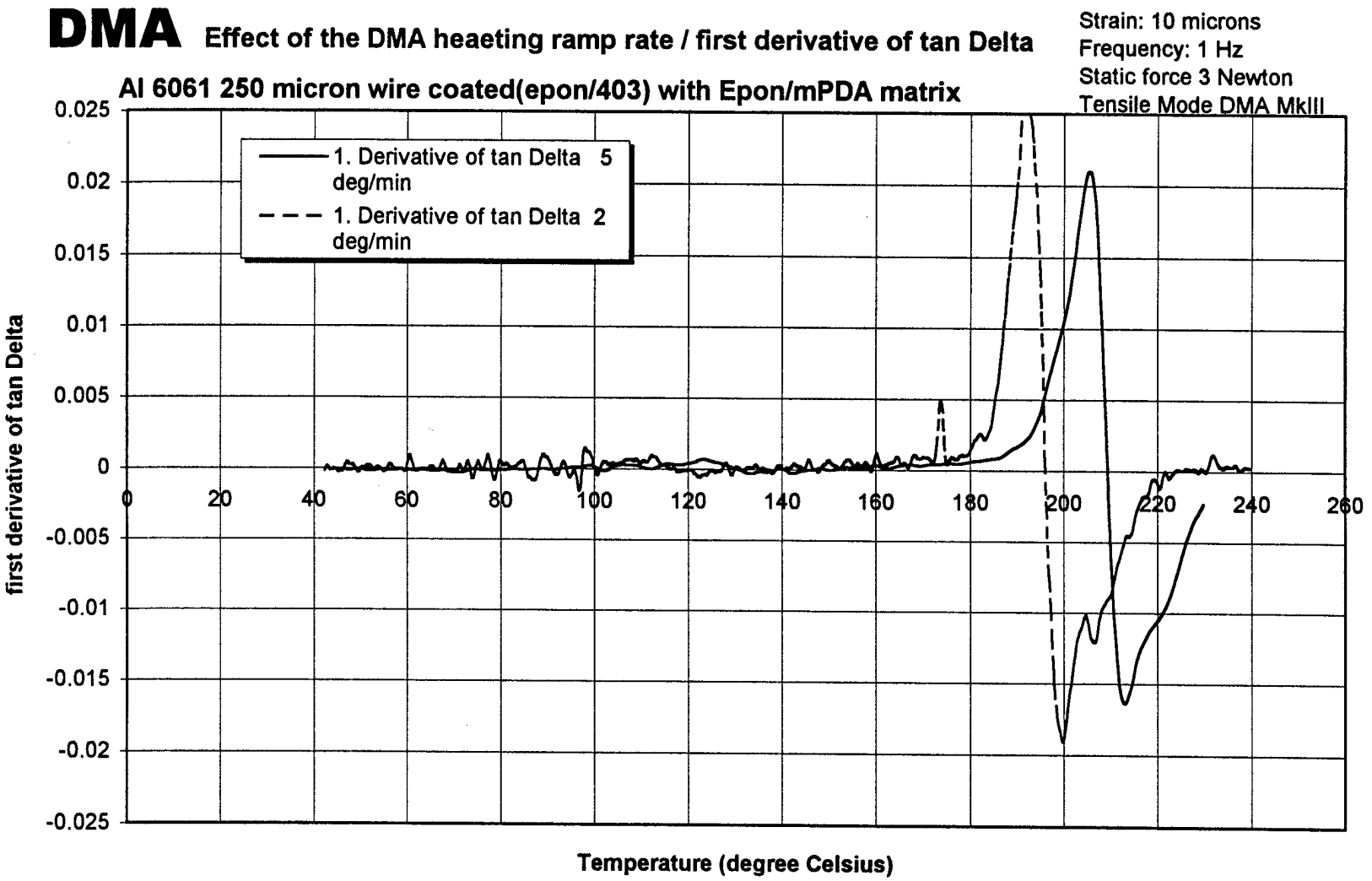

Figure 4.4.26. Effect of the heating rate on the first derivative of tan Delta

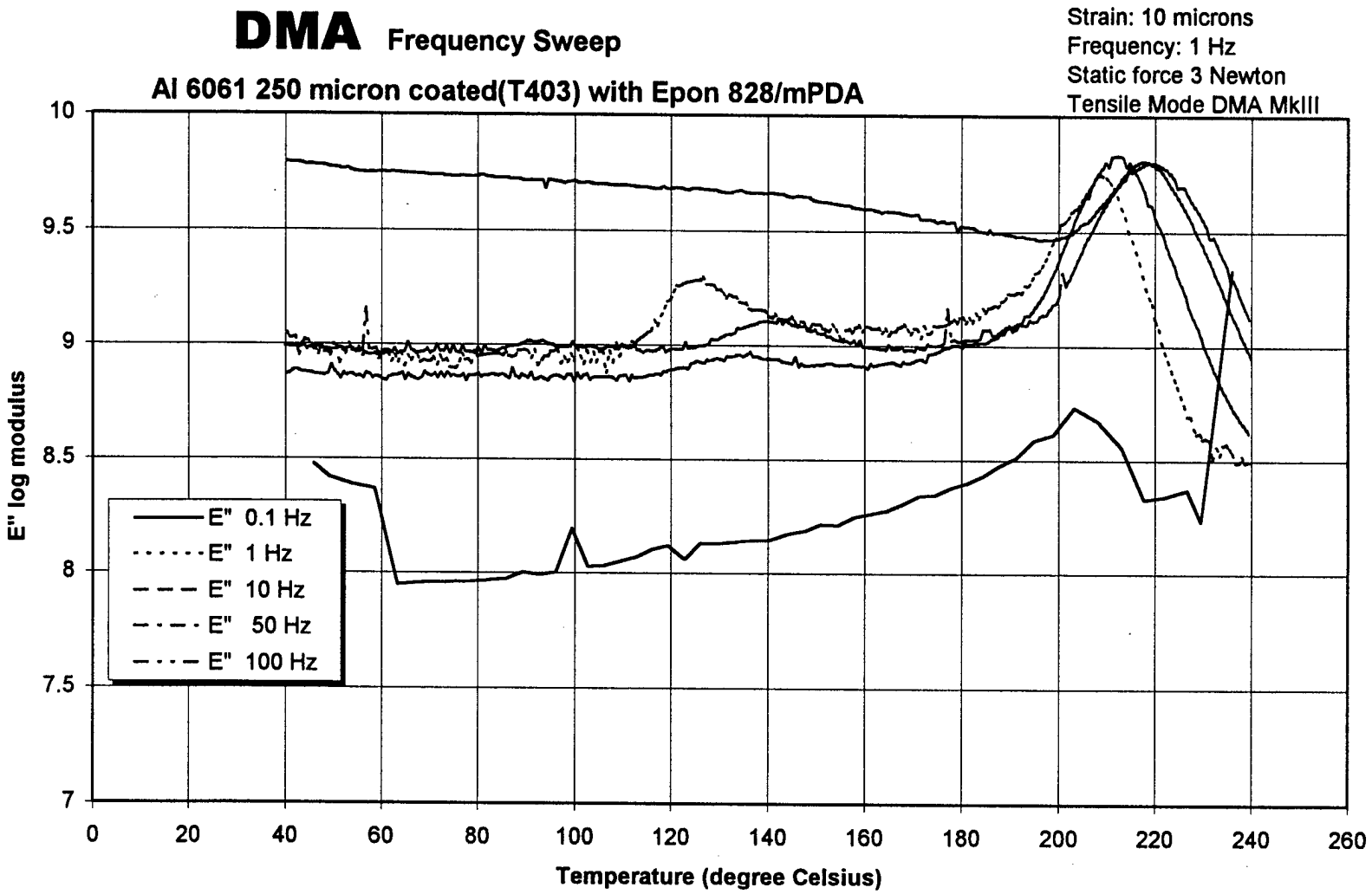

Figure 4.4.27. Effect of frequency on loss modulus, E"

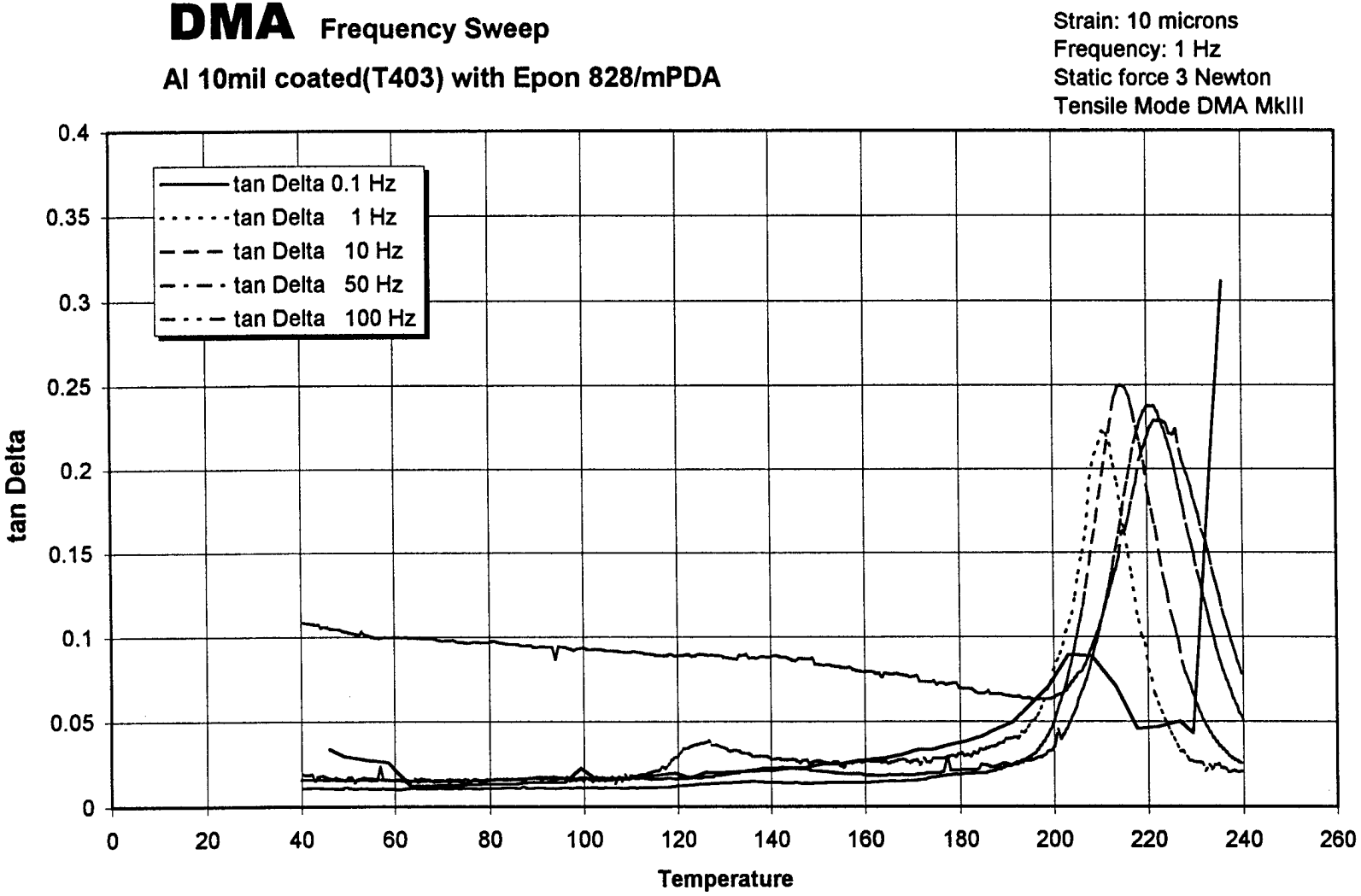

Figure 4.4.28. Effect of frequency on tan Delta

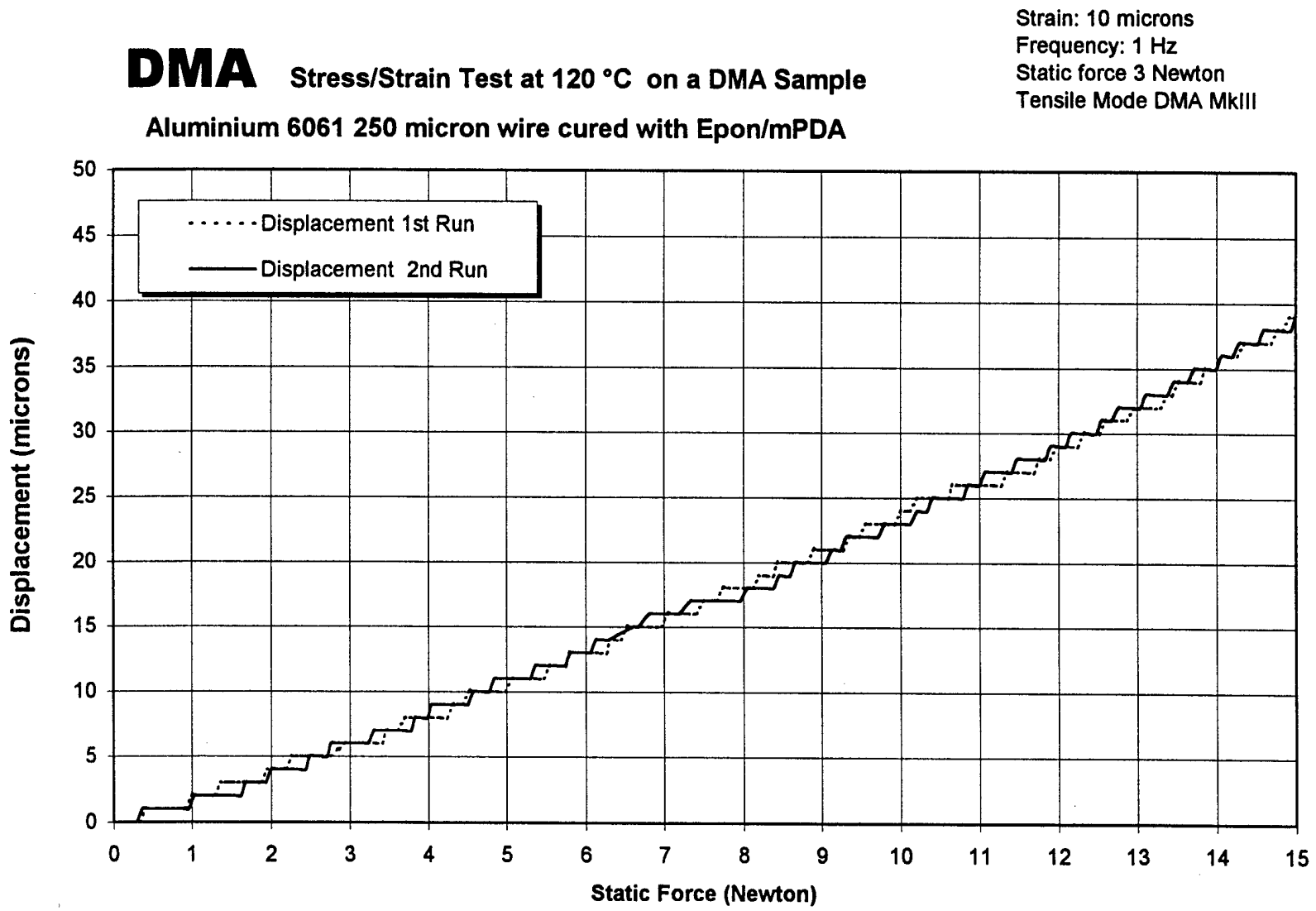

Figure 4.4.29. Stress/Strain Test at 120°C